
Influence of Pressure, Temperature and Composition on Magnetic Recording in Meteorites

Michael W. R. Volk



München 2016

Influence of Pressure, Temperature and Composition on Magnetic Recording in Meteorites

Michael W. R. Volk

Dissertation
zur Erlangung des Doktorgrades
an der Fakultät für Geowissenschaften
der Ludwig-Maximilians-Universität
München

vorgelegt von
Michael W. R. Volk
aus München

München, den 14.06.2016

Erstgutachter: Prof. Dr. Stuart A. Gilder

Zweitgutachter: Prof. Dr. Michael Winklhofer

Tag der mündlichen Prüfung: 29.08.2016

Contents

Introduction and Summary	1
1. Effect of static pressure on absolute paleointensity recording with implications for meteorites	11
1.1. Introduction	12
1.2. Materials, methods and results	17
1.2.1. Samples	17
1.2.2. Methods	18
1.2.3. Results	21
1.2.4. Paleointensity experiments after pressure cycling (hydrostatic stress)	24
1.2.5. Stress effect on remanent magnetizations acquired in strong magnetic fields	32
1.3. Discussion and Conclusions	33
2. Low temperature magnetic properties of monoclinic pyrrhotite with particular relevance to the Besnus transition	37
2.1. Introduction	38
2.2. Materials, Methods and Results	40
2.2.1. Samples	40
2.2.2. Rock Magnetic Measurements	42
2.2.3. Hysteresis parameters as a function of direction and temperature	47
2.2.4. Temperatures above T_{Bes} (> 34 K)	47
2.2.5. Temperatures within T_{Bes} (34-28 K)	49
2.2.6. Temperature below T_{Bes} (< 28 K)	52
2.2.7. Symmetry considerations	53
2.3. Discussion and Conclusions	57
3. Magnetic Properties of $\text{Fe}_{(100-x)}\text{Ni}_x$ with x from 2 - 20	61
3.1. Introduction	61
3.2. Mechanical alloying	67

3.3. Synthesis	69
3.3.1. Milling Protocol	71
3.4. Samples	72
3.4.1. Sample Preparation	73
3.5. X-ray diffraction	73
3.6. Magnetic Measurements	74
3.6.1. Changes of magnetic properties during alloying	75
3.6.2. Rock Magnetic Measurements	76
3.7. Dependence on Ni concentration	90
3.7.1. Thermomagnetic Measurements	90
3.7.2. Rock Magnetic Measurements	93
3.8. Discussion	95
3.9. Conclusions	99
4. Design of a Paleomagnetic Oven	101
4.1. Setup	102
4.1.1. Magnetic Shielding	103
4.1.2. The Boat	103
4.1.3. Heating Chamber	104
4.1.4. Cooling Chamber	110
4.2. Calibration and Testing	112
4.2.1. Lowrie test	117
4.3. Conclusions	118
5. Conclusions	121
Appendix A. Appendix	127
A.1. Effect of static pressure on absolute paleointensity recording . . .	127
A.2. Low temperature magnetic properties of monoclinic pyrrhotite . .	129
Curriculum Vitae	149

List of Figures

0.1. Meteorite classification	3
0.2. Chondrite NRM/Intensity compilation	4
0.3. Paleointensities of Meteorites	5
1.1. Effect of Pressure demagnetization and piezo remanence	14
1.2. Rock magnetism: Thermocurve and hysteresis loop for a representative sample and Day plot for all samples	19
1.3. Typical Arai diagram for different pressures	23
1.4. Hydrostatic samples: mean Arai diagrams, thermal demagnetization, and pTRM acquisition	25
1.5. Non-hydrostatic samples: mean Arai diagram, thermal demagnetization and pTRM acquisition	27
1.6. Model and data of relative differences between pressure cycled and zero pressure data	29
1.7. Pressure demagnetization of NRM and SIRM	30
1.8. Change in paleointensity with pressure	34
2.1. Hysteresis loops and Day plot for pyrrhotite bearing rock samples	44
2.2. Continuous low temperature demagnetization of pyrrhotite bearing samples	45
2.3. Stepwise low temperature demagnetization of pyrrhotite bearing samples	46
2.4. Hysteresis loops of a pyrrhotite single crystal at different temperatures	48
2.5. Polar representation of rock magnetic properties at different temperatures	50
2.6. Mean hysteresis parameter as a function of temperature	51
2.7. Normalized magnetizing energy for all angles and temperatures . .	54
2.8. Polar representation of the second inflection phenomenon through first derivatives at selected temperatures	55
2.9. Relative differences of magnetization measured at different angles compared to the room temperature easy axis	57
2.10. Unnormalized magnetizing energy for all angles and temperatures	60

3.1. Crystal structures of α -Fe,Ni and γ -Fe,Ni	62
3.2. Simplified Fe–Ni phase diagram	63
3.4. Schematic of ball milling procedure	68
3.5. Milling setup	70
3.6. Comparison of X-ray diffraction data for Fe ₈₀ Ni ₂₀ powder unmilled and milled	73
3.7. Particle size determined by the Rietveld method for Fe ₈₀ Ni ₂₀ . . .	75
3.8. Curie temperatures of Fe ₈₀ Ni ₂₀ at different milling (400 rpm) times	76
3.9. Room temperature hysteresis and backfield	78
3.10. Changes in magnetic properties of Fe ₈₀ Ni ₂₀ with milling time . . .	79
3.11. Backfield and IRM acquisition contour plots	80
3.12. Henkel and Cisowski plot at different milling times	82
3.13. Remanence and coercivity ratio versus the crossover points	84
3.14. FORC diagram for Fe ₈₀ Ni ₂₀ milled for 1440 min	87
3.15. Examples of Langevin fitting for Fe ₈₀ Ni ₂₀ at selected milling times	88
3.16. Results of Langevin fitting of milling data	89
3.17. Thermomagnetic curves for Fe _{100-x} Ni _x , x=(2,4,6,8,12,20) in air and with reducing agent	91
3.18. Curie temperatures for Fe _(100-x) Ni _x compositions	92
3.19. Hysteresis, backfield and IRM acquisition measurements for differ- ent Fe _{100-x} Ni _x	93
3.20. Rock magnetic results for different Fe _{100-x} Ni _x compositions	94
3.21. Remanence and coercivity ratios for different Fe _{100-x} Ni _x compositions	98
4.1. Magnetic Shield	104
4.2. Sample boat	105
4.3. Heating wire configurations	106
4.4. Heating chamber dimensions	107
4.5. Heating chamber	109
4.6. Heating chamber design	110
4.7. The furnace operating software <i>magovencontrol</i>	111
4.8. Cut through Oven chamber	112
4.9. Frame of Paleomagnetic Oven	113
4.10. Cooling section	114
4.11. Heating and cooling times	115
4.12. Data of furnace calibration	116
4.13. Testing: Lowrie test	117
4.14. Finished furnace inside the Mu-metal shield installed in the lab. .	119
5.1. Arai diagram: Ambiguity of paleointensity determined from PSD and MD grains	123

5.2. Arai diagrams before and after pressure cycling with correcion . .	125
A.1. Alternating field (AF) demagnetization of a 1.2 T SIRM after pres- sure cycling	127
A.2. Normalized alternating field (AF) demagnetization of a 1.2 T SIRM after pressure cycling	128
A.3. Polar representation of non normalized rock magnetic results for all temperatures	129
A.4. Polar representation of normalized rock magnetic results for all temperatures	130
A.5. Polar representation of the second inflection phenomenon through first derivatives for all temperatures	131

List of Tables

1.1. Paleointensity results (0-1.8 GPa)	22
2.1. Room temperature hysteresis results for pyrrhotite bearing samples and crystals	43
2.2. Mean results from rotational hysteresis of a pyrrhotite single crystal at different temperatures	53
3.1. Milling protocols used in the study	72
3.2. Rock magnetic results for different milling times of $\text{Fe}_{80}\text{Ni}_{20}$. . .	77
3.3. Coercivity and remanence ratios for all milling time for the $\text{Fe}_{80}\text{Ni}_{20}$	85
4.1. Commercially available thermal demagnetization oven	102
4.2. Heating wire configuration	108
4.3. Overview of heating and cooling times	116

Every aspect of Nature reveals a deep mystery and touches our sense of wonder and awe. Those afraid of the universe as it really is, those who pretend to nonexistent knowledge and envision a Cosmos centered on human beings will prefer the fleeting comforts of superstition. They avoid rather than confront the world. But those with the courage to explore the weave and structure of the Cosmos, even where it differs profoundly from their wishes and prejudices, will penetrate its deepest mysteries.

CARL SAGAN, *Cosmos*

Summary

Meteorites potentially record the magnetic fields present during the nascent formation of the early solar system. However, the interpretation of the magnetic records contained within them is complicated by a myriad of variables including poorly understood magnetic minerals and events occurring after the lock-in of the original magnetization such as shock, decompression and low-temperature cycling from space to the Earth's surface. This dissertation attempts to place constraints on how some of these factors influence paleomagnetic recording in meteorites. Through the development of a pressure cell, we show that even low pressures (<2 GPa) will lower the remanent magnetization intensity in rocks. The magnetic field strength determined from shocked or decompressed material can be appreciably underestimated and should only be taken as a lower limit. Monoclinic pyrrhotite is commonly found in certain achondritic meteorites, especially those from Mars. Monoclinic pyrrhotite undergoes a magnetic phase transition at ca. 30 K, called the Besnus transition, whose mechanism is poorly understood and highly debated. We provide evidence that this magnetic phase transition is due to a crystallographic reorientation in symmetry. Furthermore, our experiments show that low temperature cycling from their thermal equilibrium temperature in space to ambient surface temperatures on Earth will not significantly alter the paleointensity value recorded in pyrrhotite-bearing meteorites. The most common magnetic mineral in meteorites are body centered cubic iron-nickel alloys; however, the magnetic properties of these alloys as a function of grain size is virtually unknown. As grain size bears drastically on the ability to carry and retain magnetic remanence, filling this gap in our knowledge is crucial to properly interpret the paleomagnetic recording of FeNi alloys that are so ubiquitous in nature. For this reason, we initiated a research program to synthesize FeNi alloys with well constrained compositions and grain size distributions through mechanical alloying. Mechanically alloyed powders show similar magnetic properties to published results on metal bearing meteorites, but the size threshold for stable single domain particles— the domain state essential for paleomagnetism— was never identified. Finally, the design, building and implementation of a unique paleomagnetic thermal demagnetizing oven is presented.

Acknowledgments

Firstly, I would like to express my sincere gratitude to my advisor Stuart Gilder for sparking my interest in magnetism, guiding me through a bachelors and masters thesis and ultimately leading me through this thesis. I am very lucky that I was allowed to explore these topics on my own terms. I could always rely on his patience, motivation, and knowledge and ask for advice, wherever I needed it.

My sincere thanks also goes to my colleague and friend Michael Wack, who kept a sense of humor when I had lost mine for countless discussions that helped shape this research.

I am indebted to the "Deutsche Forschungsgemeinschaft" for financing the research.

I would also like to thank Nikolai Petersen, Elmar Schmidbauer, Michael Winkhofer, Karl Fabian and Ramon Egli for their ever ready advice, their insightful comments and encouragement. The kind people at the "Institute for Rock Magnetism", Joshua Feinberg, Michael Jackson, Dario Bilardello, Pete Solheid and Bruce Moskowitz for their support during my stay as a visiting fellow and for giving me the opportunity to work with them in the coming years.

Special thanks to Bernd Meier, Karl-Thomas Fehr and Amanda Günther for their help with X-ray diffraction. I would like to thank all other colleagues here at the department, the other doctoral students and student helpers, who made this journey the more pleasurable.

Finally I want to express my gratitude to my friends and family for their patience and support. A simple thank you, cannot express how much their support means to me.

If I have seen further, it is by standing on the shoulders of giants.

Isaac Newton

Introduction and Outline

Meteorites are among the oldest known materials in our solar system. They originate from primordial matter and early solar system planetary bodies and thus contain unique information on the early solar system, its composition and its formation. During the late 50s [Stacey & Lovering, 1959] it was recognized that the magnetic information stored in them could help in reconstructing the history of early solar system.

Meteorites are classified into 4 types, chondrites, achondrites, irons and stony irons [Anders, 1971] (fig. 0.1). These classes can generally be described as different stages of planetary formation with chondrites being the oldest. It is believed that chondrites are formed by melting of primordial material in the accretionary disk of the solar nebular [Acton et al., 2007]. Even though evidence for dynamo generated fields have been found in the carbonaceous chondrite Allende, it is generally believed that the chondrite parent body is undifferentiated [Carpenter et al., 2011]. These primitive stony meteorites contain chondrules, millimeter sized spherical silicate droplets, that often contain inclusions of iron-nickel minerals. Recent studies have found that these inclusions could well carry a stable magnetization and thus retain information of pre-accretionary magnetic fields [Fu et al., 2014, Lappe et al., 2011, Uehara & Nakamura, 2006, Van de Moortèle et al., 2007].

The other meteorite classes are of planetary (Martian) or asteroidal origin and originate from different depths on their parent body. Large-scale compositional structures of planets are primarily established during early differentiation. Thus it is generally believed that iron meteorites represent material from planetary

or asteroidal cores and stony irons originate from the mantle of a planetesimal (fig. 0.1)[Tarduno et al., 2012, Weiss et al., 2010]. Advances in analytical geochemistry, the increasing diversity of extraterrestrial samples, and new paleomagnetic data help our understanding of the nature and timing of these early melting processes. Differentiation of a planetary body can lead to the convection of material and formation of a core dynamo.

One of the main goals of extraterrestrial magnetism is to quantify the intensities of these planetary bodies and has shown that even small planetesimals may possess core dynamos [Nichols et al., 2016]. In particular, recent studies of a group of basaltic achondrites, called angrites, coupled with new theoretical insights into the possibility of dynamo generation on small bodies, indicate that some meteorites might retain primary records of internally generated fields [Weiss et al., 2008a, 2009, 2010]. The emerging results indicate that some planetesimals formed metallic cores and early dynamos within just a few million years of solar system formation. Similarly, paleointensity values from other meteorite classes yield insight into the dynamo process of the terrestrial planets—notably Mars [Gattacceca & Rochette, 2004, Rochette et al., 2001, Weiss et al., 2008b, 2002].

Several methods have been developed to determine the intensity of the ancient magnetic field. Thellier & Thellier [1959] established a physically rigorous technique, based on Néel theory, to determine paleo-field intensities that is widely (with variants) used today. The Thellier technique compares the thermal demagnetization spectra of a rock’s natural remanent magnetization (NRM) with the acquisition of an artificial thermoremanence (TRM) by cooling the sample in a known laboratory field. If the two are proportional, then the sum of NRM lost + TRM gained should remain constant as a function of temperature, and the slope of NRM lost to TRM gained normalized by the laboratory field yields the paleointensity value. This technique is only rigorously valid for rocks bearing solely single domain magnetic particles and will only yield linear slopes if no change in the magnetomineralogy occurs since lock-in of the thermal remanence. The presence of multidomain grains will produce non-linear slopes, rendering ambigu-

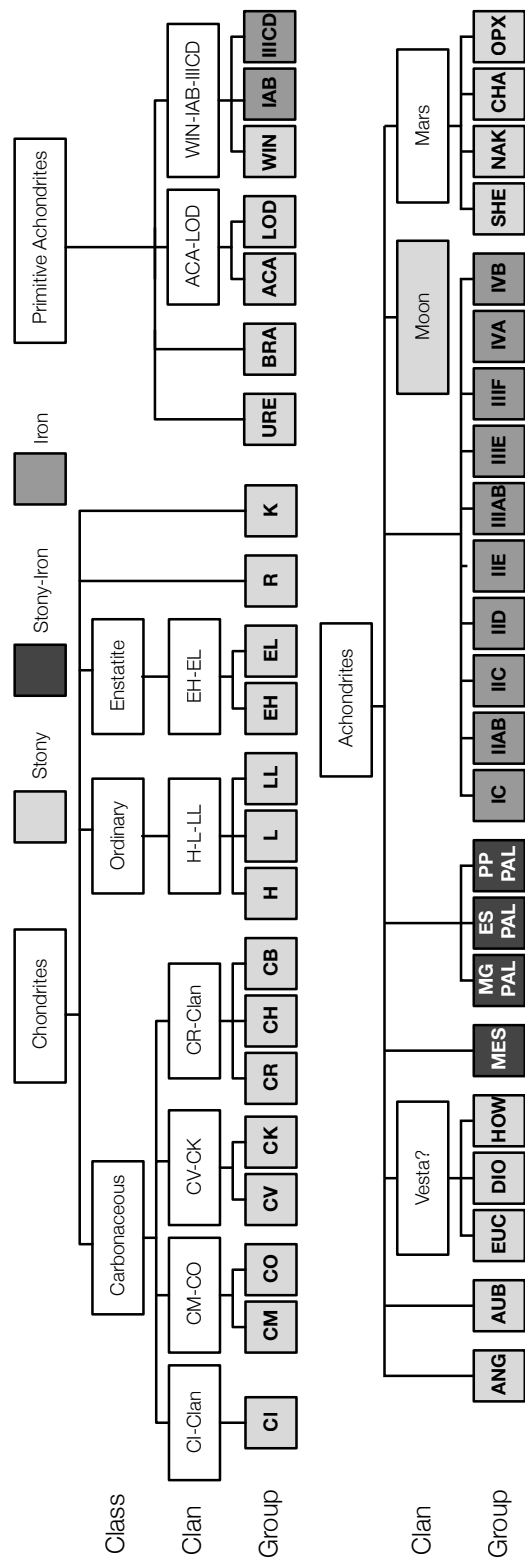


Figure 0.1.: Meteorite Classification after to Weisberg et al. [2006].

ous data interpretation. Despite these potential pitfalls, the Thellier method has been applied to meteorites, and the data were interpreted as evidence for the existence of Earth-like paleo-fields in the early solar system (fig. 0.3) [e.g. Banerjee & Hargraves, 1972, Butler, 1972, Morden, 1992, Nagata, 1979b, Stacey, 1976].

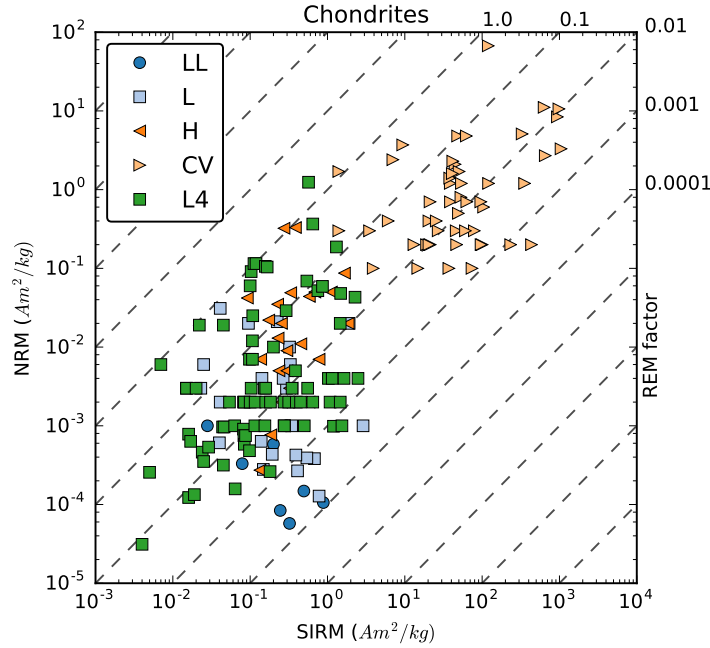


Figure 0.2.: Compilation of data for NRM against the saturation isothermal remanent magnetization (SIRM) for different meteorite types. H (high iron, red triangles), L (low iron, green squares), LL (very low iron, blue circles) [Sugiura & Strangway, 1988], L (low iron, open squares) [Wasilewski et al., 2002], and CV (blue triangles) [Emmert et al., 2011] chondrite meteorites. The diagonal lines show the NRM/SIRM ratio (REM).

As the classic Thellier method is not well suited to study meteorites due to thermo-chemical alteration, several workers use relative paleointensity experiments to determine intensity estimates [e.g. Acton et al., 2007, Emmerton et al., 2011, Gattacceca et al., 2007, Wasilewski et al., 2002, Weiss et al., 2008a]. Several different relative methods exist. The REM method uses the ratio of the natural remanent magnetization to saturating isothermal remanent magnetization (SIRM) acquired in a strong field at room temperature (fig. 0.2) to estimate the paleointensity [Cisowski et al., 1975, Lappe et al., 2013, Yu, 2010] ($\text{NRM}/\text{SIRM}=\text{REM}$),

while the REM' method is based on the derivative of alternating field demagnetizations of the NRM and SIRM [Gattacceca & Rochette, 2004]. These methods have the disadvantage that they are mineral specific and require calibration measurements to calculate the paleointensity [Fuller & Cisowski, 1987, Kletetschka et al., 2004a, Yu, 2006, 2010]. Calibration measurements have been done on many minerals commonly found on Earth [Gattacceca & Rochette, 2004] but those for extraterrestrial material are still sparse.

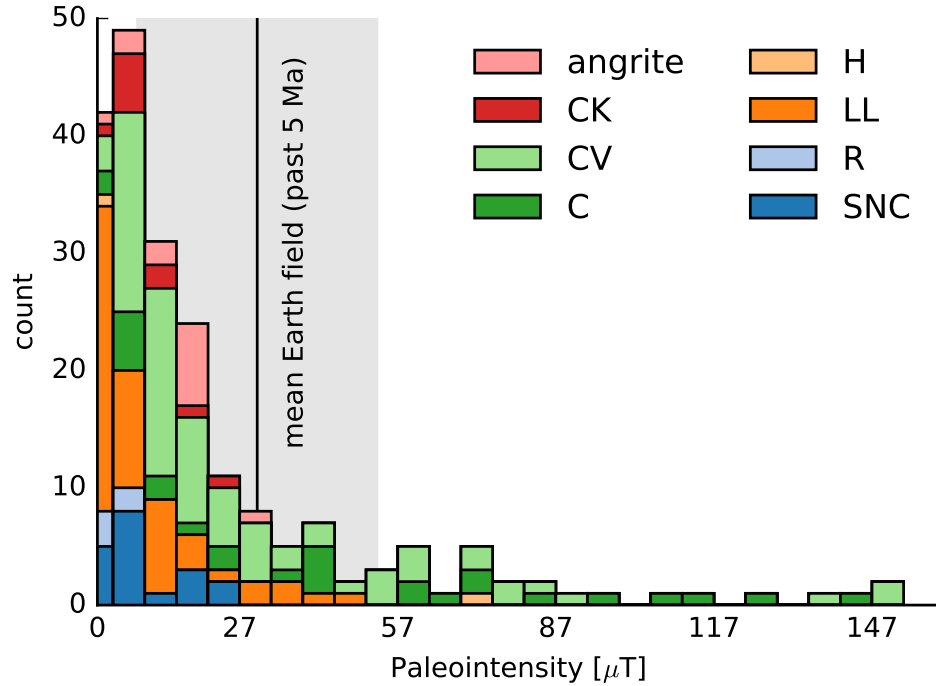


Figure 0.3.: Histograms of estimated paleointensities determined by REM methods from previous studies [Acton et al., 2007, Brecher et al., 1977, Emmerton et al., 2011, Gattacceca & Rochette, 2004, Wasilewski et al., 2002, Wasilewski, 1981b, Weiss et al., 2008a] for several meteorite classes. C, CV, CK, H, LL, R are chondritic meteorites. Angrites are among the oldest meteorites from differentiated planetesimals. SNC (shergottite, nakhlite, and chassigny) are three types of meteorites believed to originate from Mars. Line shows the mean Earth field in the past 5 million years with two standard deviations (shaded region) (data obtained from Pint database [Biggin et al., 2009]).

Meteorite magnetism faces several challenges, which cause skepticism within the

community towards field strengths determined from extraterrestrial materials and their interpretations. Paleointensities tend to have large margins of error and values can span several orders of magnitude [Gattacceca & Rochette, 2004]. This often leads to widely different paleointensity estimates within a group of meteorites (fig. 0.3) and even within one specimen. The intention of this work is to tackle some of the problems faced by paleointensity determinations on meteorites, to check their validity and to help build a solid foundation on which future studies can be built upon.

Geological settings of terrestrial rocks are generally well known, but for meteoritic material, this information is rarely available. With the exception of the howardite-eucrite-diogenite (HED) clan and lunar and Martian meteorites, neither the parent body nor the precise depth of origin or thermal and shock history of a meteorite is known [Weiss et al., 2010]. Meteorites often experienced a complicated strain history, from shock, decompression from depth in the original parent body, etc. Shock and static pressures are well known to modify the saturation remanent magnetization direction, coercivity, susceptibility, and anisotropy of susceptibility and remanence [Funaki & Syono, 2008, Gattacceca et al., 2007, Gilder & Le Goff, 2008, Gilder et al., 2004, Kapicka, 1983, Louzada et al., 2007, 2010, Nishioka et al., 2007, Pohl & Eckstaller, 1981]. Prior to the last few years, nearly all paleointensity experiments largely ignored the possibility that shock might affect paleointensity estimates. Indeed evidence for shock is commonly found in meteorites and is categorized into 5 classes ranging from S0 (no shock) to S5 (shock > 80 GPa) [Sharp & DeCarli, 2006, Stöffler et al., 1991]. However, petrographic shock barometers can only distinguish shock events with pressures above 4-5 GPa, which leaves events below 5 GPa (S0 to S1) void of evidence [Weiss et al., 2010]. Even low pressures (< 0.5 GPa) act to decrease the NRM moment or even completely erase the remanent magnetization [Bezaeva et al., 2007, Gattacceca et al., 2006, Gilder et al., 2006], in a manner analogous to alternating field demagnetization [Dunlop et al., 1969]. On the other hand, pressure applied in the presence of an ambient field leads to an enhancement of the remanence-carrying capacity of both single and multidomain grains, called

piezoremanence [Gattacceca et al., 2008, Gilder & Le Goff, 2008, Gilder et al., 2004, Pohl et al., 1975, Pohl & Eckstaller, 1981]. Both effects can change the slope of Thellier experiments and influence the paleointensity.

The first chapter of this thesis reports experiments on the effects of static pressure on absolute paleointensities. Thellier-type experiments were carried out on 40 samples whose magnetic remanence is carried by pseudo-single domain, low Ti titanomagnetite—typically found in some achondritic meteorites [Weiss et al., 2010]. The initial (zero pressure) experiment correctly reproduced the laboratory field imparted on the samples. The samples were given a new thermo-remanent magnetization, encased in a Teflon cup, and pressurized in a stainless steel pressure vessel, which was specifically designed and built to withstand pressures of 1.8 GPa. Pressure cycling to a maximum pressure of 1.8 GPa using salt as non-hydrostatic and silicone oil as hydrostatic pressure medium provoked a pressure demagnetization effect that reduced the room-temperature thermo-remanent magnetization. The degree of magnetization loss depends on the level of hydrostaticity: hydrostatic pressure decreases the NRM moment by 10%/GPa while non-hydrostatic pressure has a four times greater effect (40%/GPa). The recorded paleointensity was decreased 10 %/GPa under hydrostatic stress and 20 %/GPa under non-hydrostatic stress, showing for the first time that paleointensity results from meteorites may be appreciably underestimated. For the work described in this chapter I designed the experiments and the high pressure cell required to execute them. I conducted all the experiments and analysis. The results of this study are currently in revision.

Volk, M. W. & Gilder, S. A. (2016). Effect of static pressure on absolute paleointensity recording with implications for meteorites. *Journal of Geophysical Research: Solid Earth*, in revision

An equally serious difficulty, related to the interpretation of the paleomagnetic record of meteorites is the presence of unusual ferro- and ferrimagnetic minerals and their poorly understood remanence carrying capabilities [Rochette et al., 2009]. The following two chapters are concerned with studying the magnetic

properties of some of those minerals.

Monoclinic pyrrhotite, is a mineral often found in Martian as well as certain chondritic meteorites [Cournede et al., 2015, Rochette et al., 2001]. It crystallizes in a monoclinic (pseudo-hexagonal) crystal structure. It owes its ferrimagnetism to the ordered structure of Fe vacancies and undergoes a poorly understood magnetic / crystallographic phase transition at 30-35 K (Besnus transition). It is known that cooling pyrrhotite bearing samples causes a low temperature demagnetization of the remanent moment especially at the transition. Paleointensity experiments, however rely on an undisturbed natural remanent magnetization. Meteorites in space are cooled significantly (120-135 K) below their Curie temperatures [Weiss et al., 2010] and then warmed back to 300 K when they fall to Earth. A question that has thus far not been answered is how low temperature demagnetization of pyrrhotite influences the remanent magnetization and hence, on paleointensity results.

Chapter two concerns the low temperature magnetic properties of monoclinic pyrrhotite. It describes low temperature experiments on pyrrhotite bearing rocks with different domain states (pseudo-single to multidomain). The samples were given a saturating isothermal remanent magnetization (SIRM) at room temperature in a 1 T field. Using a vibrating sample magnetometer, the magnetic moment during low temperature cycling to successively lower temperatures was measured. Demagnetization of the SIRM was determined as a function of temperature. The experiments show that demagnetization after cooling to 150 K is largely dependent on grain-size with little demagnetization ($< 10\%$) for small grain sizes and twice as much for larger ones. Furthermore, the nature of the magnetic transition (Besnus transition) was investigated on an oriented single crystal of monoclinic pyrrhotite. Hysteresis loops and backfield curves were measured at 21 temperatures spanning the transition in 5° steps (10° for backfield) in the crystallographic basal plane of the crystal. The experiments showed that during the transition, hysteresis parameters change drastically and the large (2.6 mm) crystal becomes more single domain-like below the transition. At 50K the crystal developed a sec-

ond inflection in the hysteresis loops measured in between the crystallographic a-axes, which revealed a sixfold symmetry. At temperatures below the transition this pattern disappears, to be replaced by a fourfold symmetry. Since these changes are linked to the crystal structure, our results indicate that the Besnus transition is of crystallographic origin. For this part I have designed and conducted the experiments. Part of the work was done during a *visiting fellowship* at the Institute for Rock Magnetism (IRM), University of Minnesota, USA. The results of this study are in preparation for publication in the *Geophysical Journal International*.

Even though Fe,Ni alloys are among the most common minerals in many classes of meteorites (e.g., kamacite and taenite) their magnetic properties and their dependence on particle size (single domain - multidomain) are not well understood. Such knowledge is indispensable to properly interpret relative paleointensity data and to unravel the magnetic signals in meteorites. In the third chapter, magnetic measurements on mechanically alloyed FeNi particles of different compositions are presented. Hysteresis and backfield curves show a dependence on milling time and energy so that the alloying process can be directly observed in the magnetic parameters. Unfortunately, even though grain-sizes down to ≈ 10 nm were achieved, the single domain to multidomain threshold could not be determined due to strong magnetic interactions. The dependence of the hysteresis parameters on nickel concentration, however suggests a change in SD/MD threshold with increasing Ni. I designed the experiments, synthesized the samples together with a student helper and measured most of the data, in part during the *visiting fellowship* at the Institute for Rock Magnetism. We are currently preparing a manuscript describing the changes in magnetic properties during milling and their dependence on milling intensity for submission to the *Journal of Magnetism and Magnetic Materials*. It will be submitted in the coming months.

The final chapter describes my work to develop and test a large thermal demagnetization furnace commonly needed in paleomagnetic studies. The oven complements the institute's automatic measurement system with a sample capacity

of 96 samples and maximum temperature of 700°C. It consists of two chambers (heating and cooling), giving the possibility to heat and cool two different sample holders at the same time, thereby reducing heating+cooling times by nearly half. The heating chamber is divided into three independently controlled sections to minimize thermal gradients. *magovencontrol* a python software controls the furnace and alerts the user via email, as soon as a heating run is finished. The software also allows for dynamic temperature offset control and real time display of temperatures at both ends and the center of the sample region. To our knowledge this is the first software controlled and the largest paleomagnetic furnace. I designed the furnace and created technical drawings for every part using Solid-Works (CAD software). I helped in the building process wherever I could. The final testing was done by me with the help of other PhD students. The software for the furnace was written by Michael Wack.

1. Effect of static pressure on absolute paleointensity recording with implications for meteorites

The work in the following chapter has been submitted to Journal of Geophysical Research and is currently in review.

Volk, M. W. & Gilder, S. A. (2016). Effect of static pressure on absolute paleointensity recording with implications for meteorites. *Journal of Geophysical Research: Solid Earth*, in revision

Abstract

We investigated the influence of hydrostatic and non-hydrostatic stress on the recording process of magnetic field intensity with particular relevance for meteorites that experienced pressures lower than 5 GPa corresponding to the lowest shock stage classification (S1) in meteorites. Thermal remanent magnetizations were imparted on natural obsidian samples containing pseudo-single domain titanomagnetite, analogous to some achondritic meteorites. Thellier-type paleointensity experiments were carried out at ambient conditions after pressure cycling to 0.6, 1.2 and 1.8 GPa. Each experiment used ten samples to assess reproducibility, which is better than $\pm 5\%$. The recorded paleointensity decreased 10 %/GPa under hydrostatic stress and 20 %/GPa under non-hydrostatic stress, leading to

the fundamental conclusion that paleointensity results from meteorites may be appreciably underestimated. Pressure cycling shifts the blocking and unblocking spectra, thereby producing more linear slopes on an Arai diagram with increasing strain. We explain why, for samples with a single magnetization component that does not alter, a two-step paleointensity protocol sufficiently resolves the true paleointensity. Moreover, we propose that pressure cycling of multidomain and pseudo-single domain bearing samples will remove the inherent curvature of the Arai slope, thereby allowing one to obtain a more accurate estimate of the true paleointensity. Conversely, linear trends on Arai plots in meteorites might have their origin in a pressure effect that does not necessarily reflect the ubiquitous presence of single domain particles.

1.1. Introduction

Meteorites serve as windows to the early solar system. Their remanent magnetizations store information concerning the magnetic fields present during the initial stages of proto-planetary formation and the extinct dynamos once present in planets or moons. Different meteorite types lend insight into the diverse processes on how the solar system formed.

Chondritic meteorites stem from undifferentiated bodies created when primordial matter assembled 4.5 billion years ago. They potentially retain evidence of the interplanetary magnetic fields in the solar nebula [Banerjee & Hargraves, 1972]. Wardle [2007] calculated that magnetic field intensities on the order of 1-100 μT are needed to transport mass and redistribute angular momentum in the protoplanetary cloud, while sun formation during the T-Tauri stage generated 100 μT fields at a distance of 0.1 AU [Weiss & Elkins-Tanton, 2013], with some workers proposing fields as strong as 400 μT [Acton et al., 2007]. Paleointensity measurements on the extensively studied carbonaceous chondrite Allende yielded field estimates ranging from 10 to 110 μT [Banerjee & Hargraves, 1972, Butler, 1972, Nagata, 1979a, Wasilewski, 1981b]. Work on other chondritic meteorites

that specifically focused on chondrules found slightly lower yet comparable intensities ranging from 1 to 56 μT [Acton et al., 2007, Fu et al., 2014, Gattacceca & Rochette, 2004].

Incipient planets formed when chondritic material coalesced and underwent full or partial melting and subsequent differentiation to form Fe-rich cores and Mg-Fe-rich silicate mantles. Fe-Ni alloy inclusions in olivine crystals from stony-iron meteorites (pallasites) thought to originate from planetesimals ≈ 200 km in radius, yielded Thellier-based paleointensities of 70-130 μT [Tarduno et al., 2012]. Basaltic achondrites, especially those in the angrite group with a narrow age range of 4564 to 4558 Ma, are thought to be the remains of the first differentiated planetoids [Mittlefehldt et al., 2002]. This meteorite class also lends insight into planetary formation and helps constrain boundary conditions for dynamo generation processes. The angrite group is especially well suited for paleointensity determinations because their main magnetic carrier, titanium-poor magnetite, is one of the best understood magnetic remanence carriers. Using a so-called relative paleointensity technique, Weiss et al. [2008a] found field intensities of 10-20 μT recorded within the angrite parent body, which falls within the range (6 to 37 μT) of paleointensity values obtained from other achondritic meteorite classes [Gattacceca & Rochette, 2004, Hood & Cisowski, 1983] that were determined using both absolute and relative paleointensity techniques. These findings are compatible with theoretical calculations suggesting even small bodies ≈ 100 km in radius can generate fields ≥ 20 μT at their surface [Weiss et al., 2010].

The Thellier paleointensity method and its variants are commonly used to measure the magnetic field strength in material that acquired its remanence when cooling through the Curie temperature; i.e., a thermal remanent magnetization (TRM) [Thellier & Thellier, 1959]. Based on Néel [1949] theory, the Thellier method attempts to mimic the process in which the original (natural) remanent magnetization (NRM) was acquired. This consists of stepwise thermal demagnetization in a zero field to successively remove the NRM followed by stepwise remagnetization in a known laboratory field at the same temperature steps. The NRM

remaining during demagnetization is plotted against the acquired magnetization for each temperature interval in a so-called Arai diagram (fig. 1.1) [Nagata et al., 1963]. Provided that the in-field blocking of the remanence linearly correlates with the zero-field unblocking, the data will define a negative slope proportional to the paleofield strength and the known laboratory field (black line in fig. 1.1). The absolute value of the slope (NRM/TRM) multiplied by the laboratory field (B_{lab}) gives the paleointensity (B_{paleo})

$$B_{\text{paleo}} = \left| \frac{\text{NRM}}{\text{TRM}} \right| \times B_{\text{lab}}.$$

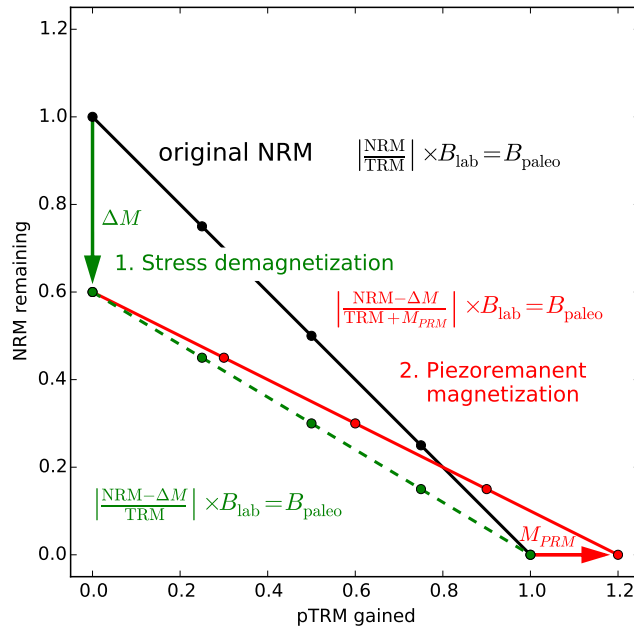


Figure 1.1.: The effect of pressure demagnetization and piezoremanent magnetization on absolute paleointensity experiments. Changes are normalized relative to the ideal case (black line and black points). Stress demagnetization (green dashed line and green points) leads to a decrease in the natural remanent magnetization (NRM), which lowers the slope (paleointensity) by 40% from the original value in this example. Piezoremanence (red line and red points) acts to increase the remanence acquisition efficiency of the grains, which leads to an increase in TRM gained (20% in this example) and a further decrease (50% in this example) in the slope (paleointensity = B_{paleo}).

Several factors lead to non-linear remanence acquisition during Thellier exper-

iments, with the biggest culprit being the creation or destruction of magnetic mineral phases through alteration or exsolution during heating. Remanence acquisition is also grain size dependent [Dunlop & Argyle, 1997], with multidomain grain sizes leading to non-linearity. Cooling rate and magnetic anisotropy can also bias paleointensity data [Leonhardt et al., 2006].

A largely unexplored problem of special concern to meteorites pertains to the effect of pressure (strain), including decompression (tension) on paleointensity determinations. For achondrites, one rarely knows where (how deep) or the size of the parent body in which the meteorite originated. The consequence is that the meteorite potentially acquired its magnetic remanence at depth and decompressed when the planetesimal broke apart. Other scenarios where pressure plays a role is when a rock became ejected from its place of genesis into space from collision (shock), collisions between bodies in space, or when the meteorite struck its host planet or moon. Six shock stages (S1-S6) are recognizable by microscopy based on mechanical deformation experiments on olivine and plagioclase [Stöffler et al., 1991]. S1, the lowest stage, corresponds to peak pressures lower than 4-5 GPa. Visible effects such as planar deformation features in olivine, mechanical twinning in pyroxene, etc., commence at stage S2 where shock pressures correspond to 5-10 GPa; pressures exceed 50 GPa for S6.

The problem addressed here concerns the effect of pressure on paleointensity recording in meteorites that experienced shock or static stress below 5 GPa (S1 stage). Indeed, it has been well established that both compression and decompression below 5 GPa influence both the remanent magnetization as well as the intrinsic magnetic properties of magnetic minerals [Cisowski & Fuller, 1978, Gattacceca et al., 2007, Gilder & Le Goff, 2008, Gilder et al., 2006, 2004, Kletetschka et al., 2004b, Louzada et al., 2007, Pohl et al., 1975]. Yet how such effects influence paleointensity values has been largely ignored.

Relative paleointensity methods might be favored over the absolute Thellier paleointensity method because they are less time consuming and do not require heating, despite the disadvantage that the paleointensity estimates can have

uncertainties exceeding an order of magnitude. Regardless of the high uncertainty, order-of-magnitude estimates may be more useful than null data from a Thellier protocol and/or destruction/alteration of the sample from the repeated heating steps. For this reason, we also performed pressure cycling experiments on samples whose moments were acquired with a direct current field (isothermal) remanence, which forms the basis of some relative paleointensity techniques. The results are compared against the pressure cycling experiments on the same rocks possessing thermal remanences.

Even in the presence of an Earth-like field (50 μT), both compression and decompression act to demagnetize the NRM of rocks (pressure demagnetization) in a manner analogous to alternating field demagnetization [Dunlop et al., 1969]. Pressure demagnetization experiments on a wide range of materials universally show a reduction of the NRM even at pressures < 1 GPa with a greater effect for uniaxial than hydrostatic pressures [Bezaeva et al., 2010, Gilder et al., 2006]. A reduction of the original NRM from pressure demagnetization would lower the slope obtained in a Thellier experiment, leading to an underestimate of the true paleointensity (green arrow and points in fig. 1.1). In the simplest case, when considering the change in moment (ΔM) due to pressure demagnetization [$\Delta M = \text{NRM}(P_0) - \text{NRM}(P_n)$], the formula for paleointensity becomes $B_{\text{paleo}} = |[(\text{NRM}(P_0) - \Delta M)/\text{TRM}(P_0)]| \times B_{\text{lab}}$.

Strain can also increase the remanence carrying capacity of a magnetic mineral beyond that of its non-strained counterpart, called piezoremanent magnetization [Gilder & Le Goff, 2008]. This would affect the in-field steps in a Thellier experiment where the magnetic carriers would acquire greater thermoremanent magnetizations (TRM) than that in a like field in the original, non-strained host. The net effect would be a further reduction of the slope in a Thellier experiment, again leading to an underestimate of the true paleointensity (red arrow and points in fig. 1.1). Taking both piezoremanent magnetization [$M_{\text{PRM}} = \text{TRM}(P_n) - \text{TRM}(P_0)$] and pressure demagnetization into account, the paleointensity can be calculated using

$$B_{\text{pal}} = \left| \left[\frac{\text{NRM}(P_0) - \Delta M}{\text{TRM}(P_0) + M_{\text{PRM}}} \right] \right| \times B_{\text{lab}},$$

which shows that both effects lead to an underestimation of the paleointensity. For example, both a 10% demagnetization of the original NRM moment and a 10% increase in moment due to piezoremanence causes the intensity to be lowered by 18%. Because the likelihood that meteorites escaped pressure cycling during their long histories in the solar system seems remote, we carried out experiments to test the effect of pressure cycling up to 2 GPa on paleointensity recording.

1.2. Materials, methods and results

1.2.1. Samples

Although well grounded in physics and acknowledged as giving the most precise paleointensity estimates, the Thellier method often yields null results due to chemical alteration and exsolution of the magnetic carriers during repeat thermal cycling up to Curie point temperatures. We therefore selected an obsidian from the Rocche Rosse (Italy) flow known for its high thermal stability [Leonhardt et al., 2006], and because it possesses low Ti magnetite similar to some angrite type achondritic meteorites [Mittlefehldt et al., 1998].

Curie temperatures were measured with a Petersen Instruments, variable field translation balance in a 50 mT field in air (fig. 1.2). Thermal cycling to increasingly higher temperatures shows a high degree of reversibility with no significant alteration. Four samples define an average Curie temperature of $538 \pm 4^\circ\text{C}$ indicative of titanomagnetite with 1.75 wt.% Ti. Magnetic hysteresis loops and backfield curves were measured on 20 samples. The magnetic hysteresis parameters lie within the pseudo-single domain field on a Day diagram (fig. 1.2) with average remanence ratios of 0.15 ± 0.02 and average coercivity ratios of 3.1 ± 0.3 shifted towards higher coercivity ratios away from the mixing lines [Day et al.,

1977, Dunlop, 2002a]. There are several possible reasons, which can cause this behavior. One explanation is a bimodal distribution of SD and large MD grains [Dunlop, 2002b]. The presence of a multidomain fraction causes samples to gain a magnetization above their unblocking temperature (high temperature tails) [Fabian, 2001]. The magnetization tail can be measured by repeated demagnetization of pTRM acquisition steps [Riisager & Riisager, 2001]. The average high temperature tail present in the samples is $\delta\text{TR} = 1.4\%$ indicating little multidomain presence. Low temperature cycling can cause irreversible loss of magnetization due to the denucleation of domain walls [Muxworthy et al., 2003]. Inappreciable changes in magnetization ($< 3\%$) occurred before and after low temperature cycling the samples in liquid N₂. Further the average coercivity $B_c = 72.8 \pm 5$ mT value is too high to support the presence of a significant MD contribution. A more likely explanation for the high coercivity ratios is the presence of super paramagnetic, single domain and pseudo-single domain particles. The sum of the rock magnetic data suggests these obsidian samples are quite suitable for Thellier- type experiments [Shcherbakov & Shcherbakova, 2001].

1.2.2. Methods

Absolute paleointensity experiments followed the Coe [1967] modified Thellier-Thellier method using the [Leonhardt et al., 2006] protocol with partial TRM (pTRM) checks, additivity checks and pTRM-tail checks. pTRM checks were measured in-field, parallel to the remanence direction following the corresponding demagnetization step. Paleointensity calculations and statistics reported here follow [Paterson et al., 2014]. Magnetic remanence measurements were done with a 2G Enterprises Inc., three axis cryogenic magnetometer housed in a magnetically shielded room using the Cryomag program package [Wack, 2010].

A shock wave from a meteorite impact induces both hydrostatic and deviatoric stresses inside the material [Pohl et al., 1975]; the more non-hydrostatic the pressure, the greater the influence on the remanence [Nagata, 1966, Pearce & Karson, 1981]. Thus, one goal of our experiments was to subject the samples

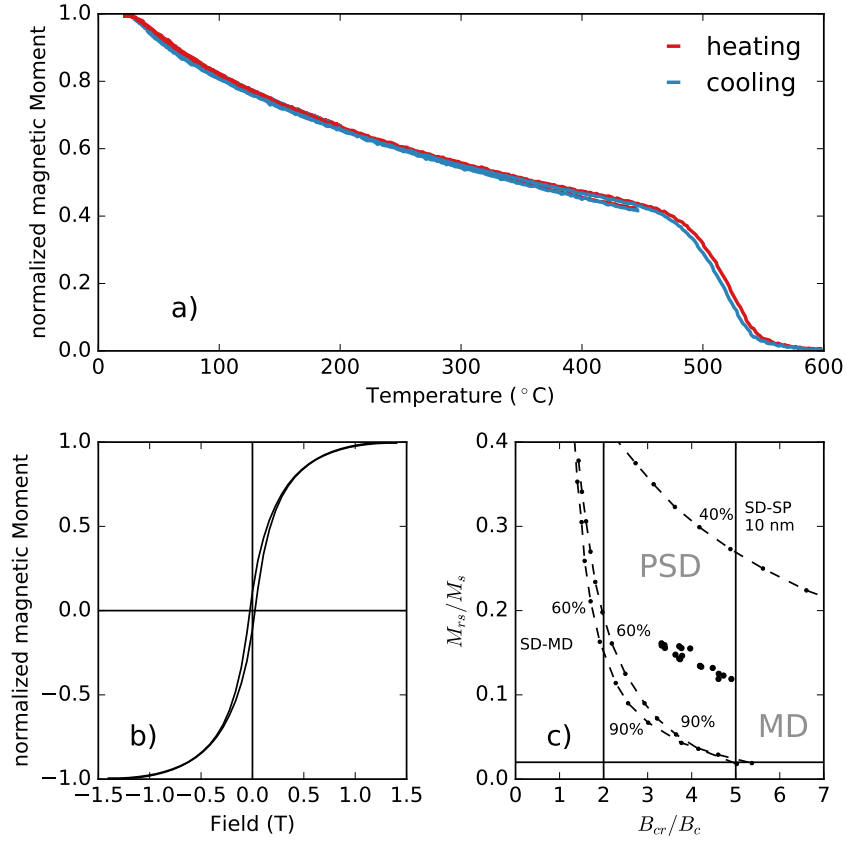


Figure 1.2.: **a)** Magnetization in a 50 mT applied field as a function of temperature. The sample was subjected to temperature cycling to 200, 450 and 600°C. Red lines show heating curves, blue lines are cooling curves. **b)** Normalized magnetic hysteresis curve. Samples in both diagrams were measured with a Petersen Instruments, variable field translation balance. **c)** Day plot for all 20 Hx+Hz samples showing the predominantly pseudo-single domain (PSD) character of the samples (MD = multidomain). Mixing lines for SD-MD and single domain and superparamagnetic (SP) from Dunlop [2002a] are shown as dashed lines.

to both hydrostatic (H) and non-hydrostatic (nH) pressures to test the role of non-hydrostatic strain on paleointensity recording. Pressure was applied by loading the samples individually into Teflon cups together with a pressure medium. Silicone oil was used in the hydrostatic (H) experiments and NaCl in the non-hydrostatic (nH) ones. The pressure cell was made of demagnetized stainless and hardened steel components with dimensions similar to the one used by [Beza-

eva et al., 2010]. Pressure was generated using a SpecAC Atlas manual 15-ton hydraulic press at room temperature. Pressure buildup and release times lasted approximately 30 seconds with peak pressure held for 10 seconds. Pressure was calculated as the applied force from the press per area of the Teflon cup which fit snugly into the pressure chamber. All pressure cycles were done in the ambient Earth's field. We tested whether the cell magnetized the sample during pressure cycling and/or whether samples acquired a remanence during pressure cycling in the Earth's field by compressing fully demagnetized samples to 2 GPa. Magnetization measured before and after cycling remained constant, meaning the remanence state of the samples was neither influenced by the cell nor the ambient magnetic field during the experiments.

The direction of the applied stress with respect to the remanence direction also influences the level of stress demagnetization or piezoremanence acquisition [Gilder & Le Goff, 2008, Kean et al., 1976]. So each H or nH experiment was carried out in duplicate, with the maximum compression axis applied perpendicular or parallel to the magnetization direction, which was in the x or z axis direction of the cylindrical sample, with the z-axis being parallel to the core axis and the x-axis perpendicular to the core axis. The four groups (Hx, Hz, nHx and nHz), each comprising ten cylindrical samples 6 mm in diameter and 5.4 mm in height, underwent the same experimental protocol.

First, all 40 samples were given thermal remanent magnetizations (TRM) by heating and cooling from 560°C to room temperature in a $35.0 \pm 0.2 \mu\text{T}$ laboratory field using a Magnetic Measurements MMTD20 oven. They were then subjected to a round of Thellier paleointensity experiments (0 GPa) and then were given a new TRM in a $35.0 \pm 0.2 \mu\text{T}$ field. After measuring their remanent magnetizations, the samples were pressurized to 0.6 GPa, and then underwent a new round of paleointensity measurements. They were again given a TRM, pressurized to the next pressure level, etc. In the end, the paleointensity for ten samples from each of the four groups were measured at 0 GPa and after pressure cycling to 0.6 GPa. Both of the hydrostatic groups (Hx and Hz) were studied

again at 1.2 and 1.8 GPa; only one pressure step (0.6 GPa) was used in the nH experiments because the samples disintegrated at higher pressures.

Relative paleointensity methods often compare the spectra of moments from step-wise alternating field demagnetization of the NRM with the demagnetization spectra after applying a direct current magnetic field at room temperature [Fuller et al., 1988, Gattacceca & Rochette, 2004]. If the two spectra are proportional, e.g., if the normalized spectra are similar, then one can assume proportionality between the two acquisition mechanisms and establish a relative paleointensity. For this reason, we compared how pressure cycling affects the magnetic recording of a sample whose remanence was acquired thermally (TRM) and with a strong magnetic field, called an isothermal remanent magnetization (IRM). All experiments described herein were carried out at Ludwig Maximilians Universität, Munich.

1.2.3. Results

Zero-pressure paleointensity experiments

All samples show narrow unblocking temperature distributions between 500°C and 550°C with less than 3% of the magnetization lost below 400°C (fig. 1.3). The 13 temperature steps in the Thellier experiments were chosen to optimize the coverage of the unblocking-blocking spectrum. Intensity determinations were based on all steps and yield an overall mean of $34.1 \pm 1.3 \mu\text{T}$ ($N=40$) (table 1.1) that matches the expected value ($35.0 \pm 0.2 \mu\text{T}$) within 1σ uncertainty limits. They have exceptionally high average quality factors (q) of 27 ± 2 , which considers the relative scatter of the best-fit line, the percentage of the NRM used for the fit and the spacing of the data [Coe et al., 1978]. Selection criteria for paleointensity studies commonly set a q threshold of 1-5 as acceptable with values of 10-20 considered very good [Paterson et al., 2015]. pTRM checks of 1.4% suggest multidomain tails are insignificant [Leonhardt et al., 2004].

Curvature of the Arai diagram arises from grains that unblock below their block-

Table 1.1.: Results from the paleointensity experiments in this study for individual samples and group averages. Abbreviations are: H, hydrostatic; nH, non-hydrostatic; x, the maximum compression axis was applied parallel to the magnetization direction; B_{paleo} , the calculated paleointensity; q, the quality factor, and ΔM , the amount of TRM moment lost after pressure cycling divided by NRM_{Po} (in percent).

	B_{paleo} [μT] 0.0 GPa	q	B_{paleo} [μT] 0.6 GPa	ΔM [%]	B_{paleo} [μT] 1.2 GPa	ΔM [%]	B_{paleo} [μT] 1.8 GPa	ΔM [%]
Hx00	35.4 \pm 1.4	23.7	33.9 \pm 1.0	-3.65	30.5 \pm 0.7	39.6	-12.21	
Hx01	35.9 \pm 1.4	23.1	34.3 \pm 0.9	-6.06	32.9 \pm 0.6	52.8	-10.89	
Hx02	32.9 \pm 1.1	25.4	32.1 \pm 0.8	-7.02	30.4 \pm 0.8	34.7	-12.50	
Hx03	33.7 \pm 1.1	26.6	32.4 \pm 0.9	-6.98	29.9 \pm 0.7	35.7	-11.70	
Hx04	34.2 \pm 1.1	29.2	34.1 \pm 0.9	-6.93	28.9 \pm 0.7	37.9	-14.48	
Hx05	33.5 \pm 1.2	27.4	33.3 \pm 0.8	-7.03	30.3 \pm 0.7	40.7	-13.14	
Hx06	36.9 \pm 1.1	30.9	33.1 \pm 0.8	-6.80	29.8 \pm 0.6	42.0	-12.84	
Hx07	34.8 \pm 1.1	27.5	34.3 \pm 1.0	-5.73	31.8 \pm 0.6	48.8	-11.54	
Hx08	35.1 \pm 1.2	25.9	34.4 \pm 0.9	-5.55	30.4 \pm 0.6	48.3	-12.25	
Hx09	34.5 \pm 1.1	27.4	34.2 \pm 1.0	-5.52	31.5 \pm 0.6	45.5	-11.62	
Hx00	33.8 \pm 1.1	28.4	32.2 \pm 0.8	-7.47	30.0 \pm 0.5	52.4	-14.39	
Hx01	34.8 \pm 1.1	28.3	32.7 \pm 0.9	-7.12	30.0 \pm 0.5	56.3	-14.85	
Hx02	34.5 \pm 1.2	27.4	33.3 \pm 0.9	-5.71	29.8 \pm 0.5	51.4	-16.77	
Hx03	34.9 \pm 1.3	25.8	33.7 \pm 1.0	-5.49	30.6 \pm 0.6	46.7	-13.99	
Hx04	34.5 \pm 1.2	27.8	33.5 \pm 0.9	-6.64	30.1 \pm 0.5	49.5	-15.16	
Hx05	35.4 \pm 1.2	27.5	33.7 \pm 0.9	-8.83	30.6 \pm 0.6	48.0	-12.22	
Hx06	34.4 \pm 1.1	28.2	33.6 \pm 0.9	-5.41	30.8 \pm 0.5	53.0	-14.51	
Hx07	34.9 \pm 1.1	27.9	34.6 \pm 0.9	-4.85	30.6 \pm 0.5	54.8	-14.15	
Hx08	35.4 \pm 1.2	27.8	33.4 \pm 0.9	-7.15	30.0 \pm 0.4	59.1	-17.59	
Hx09	35.4 \pm 1.3	24.6	33.6 \pm 1.0	-5.50	30.6 \pm 0.5	50.0	-13.89	
Hx00	34.9 \pm 1.1	28.3	29.5 \pm 0.9	-29.06				50.6
nHx01	37.1 \pm 1.3	26.8	32.6 \pm 1.3	-4.71				
nHx02	34.5 \pm 1.2	27.0	25.3 \pm 1.1	-34.75				
nHx03	33.8 \pm 0.9	33.4	32.0 \pm 1.2	-15.98				
nHx04	32.6 \pm 1.2	24.6	29.4 \pm 0.7	-16.44				
nHx05	35.1 \pm 1.0	31.4	27.5 \pm 0.7	-21.27				
nHx06	35.2 \pm 1.1	27.9	36.5 \pm 1.1	-19.22				
nHx07	35.2 \pm 1.3	25.0	30.8 \pm 1.2	-21.22				
nHx08	32.4 \pm 1.0	29.3	29.8 \pm 1.0	-27.97				
nHx09	34.9 \pm 1.4	23.3	26.8 \pm 1.2	-18.02				
nHx00	33.3 \pm 1.1	27.3	30.8 \pm 0.6	-27.93				
nHx01	33.9 \pm 1.2	25.7	30.0 \pm 0.6	-23.92				
nHx02	35.0 \pm 1.3	24.9	30.1 \pm 0.7	-31.02				
nHx03	32.3 \pm 1.1	27.8	30.0 \pm 0.6	-42.96				
nHx04	32.1 \pm 1.0	28.2	30.8 \pm 0.6	-30.12				
nHx05	32.7 \pm 1.1	27.9	30.0 \pm 0.6	-22.95				
nHx06	32.9 \pm 1.1	27.1	28.8 \pm 0.6	-30.26				
nHx07	35.2 \pm 1.3	24.8	28.8 \pm 0.8	-28.05				
nHx08	35.1 \pm 1.4	24.2	29.1 \pm 0.7	-27.01				
nHx09	33.3 \pm 1.2	24.9	29.2 \pm 0.8	-27.41				
H	34.7 \pm 0.9	27.0 \pm 1.8	33.5 \pm 0.7	-6.0 \pm 1.1	30.5 \pm 0.8	47.4 \pm 6.8	-13.5 \pm 1.7	29.0 \pm 0.8
Hx	34.7 \pm 1.1	26.7 \pm 2.2	33.6 \pm 0.8	-6.1 \pm 1.0	30.6 \pm 1.1	42.6 \pm 5.7	-12.3 \pm 1.0	46.5 \pm 8.9
Hx	34.8 \pm 0.5	27.4 \pm 1.2	33.4 \pm 0.6	-5.9 \pm 1.1	30.3 \pm 0.3	52.1 \pm 3.6	-14.8 \pm 1.4	29.2 \pm 1.1
nH	34.1 \pm 1.3	27.0 \pm 2.4	29.9 \pm 2.2	-20.9 \pm 7.9				51.6 \pm 8.0
nHx	34.6 \pm 1.3	27.7 \pm 2.9	30.0 \pm 3.0	-20.9 \pm 7.9				
nHz	33.6 \pm 1.1	26.3 \pm 1.4	29.8 \pm 0.7	-29.2 \pm 5.5				

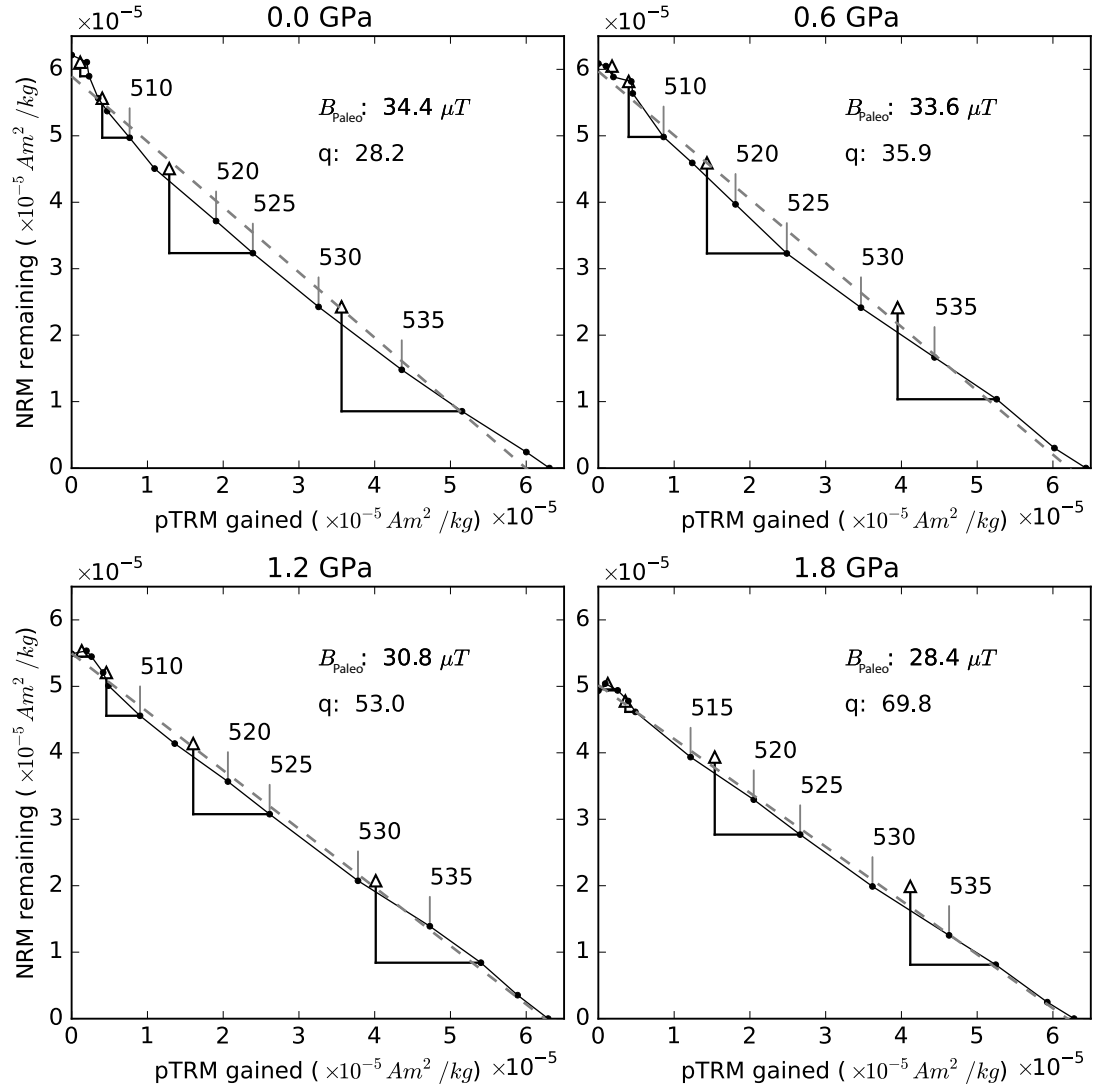


Figure 1.3.: Arai diagrams for a sample at ambient pressure (0 GPa) and then after pressure cycling to 0.6, 1.2 and 1.8 GPa. The sample was given a thermal remanent magnetization in a $35.0 \pm 0.2 \mu T$ field before pressure cycling and implementation of the Thellier-type paleointensity experiment. Temperature in $^{\circ}C$ listed for select steps.

ing temperature [Fabian, 2001], which commonly afflicts multidomain as well as pseudo-single domain sized particles. The pseudo-single domain character of the samples (fig. 1.2) causes some curvature in the Arai plot, which leads to an ambiguity on how to fit the line segment. If only the $510^{\circ}C$ to $560^{\circ}C$ unblocking

portion on the Arai diagram is used for the calculation, the quality factor increases from 27 ± 2 to 36 ± 12 , yet the average paleointensity of $30.6 \pm 1.1 \mu\text{T}$ underestimates the true value by 13%, thus we used the entire demagnetization spectrum to determine the paleointensity values.

1.2.4. Paleointensity experiments after pressure cycling (hydrostatic stress)

Following the initial (0 GPa) paleointensity experiments, a new TRM was imparted on the samples in the x ($N = 10$) or z ($N = 10$) direction. The samples were pressure cycled to 0.6 GPa, then the paleointensity experiments were performed. This process was repeated using peak pressures of 1.2 and 1.8 GPa. With some caveats described below, we found no significant difference between H_x and H_z so all 20 results were averaged together (table 1.1). There are two ways to analyze the data (fig. 1.4). The conventional approach would be to normalize the magnetic moments to the NRM. Here, the NRM would be the initial moment obtained, whether it was the 0 GPa value $[\text{NRM}(P_0)]$ or the NRM value after pressure cycling to P_n $[\text{NRM}(P_n)]$ (fig. 1.4a and 1.4b). Plotted in this way, the data exhibit piezoremanence, with an increase in acquired remanence in the high temperature part of the blocking spectrum as pressure increases. The total acquired magnetization grows by 5, 15 and 21% of the original NRM moment at 0.6, 1.2 and 1.8 GPa, respectively. This coincides with a systematic decrease in paleointensity values from $34.8 \pm 0.9 \mu\text{T}$ to $33.5 \pm 0.7 \mu\text{T}$ (-3.7 %) at 0.6 GPa, to $30.5 \pm 0.8 \mu\text{T}$ (-12.3 %) at 1.2 GPa and $29.1 \pm 0.8 \mu\text{T}$ (-16.4%) at 1.8 GPa due to an apparent piezoremanence effect.

A second approach is to normalize the paleointensity runs by the initial, pre-pressurized magnetization $[\text{NRM}(P_0)]$ (fig. 1.4a and b), thus illustrating the changes relative to the starting condition. In other words, if one had a priori information about the initial, pre-strained TRM, which of course one does not know, this approach best reflects the effect of strain. Viewed in this way,

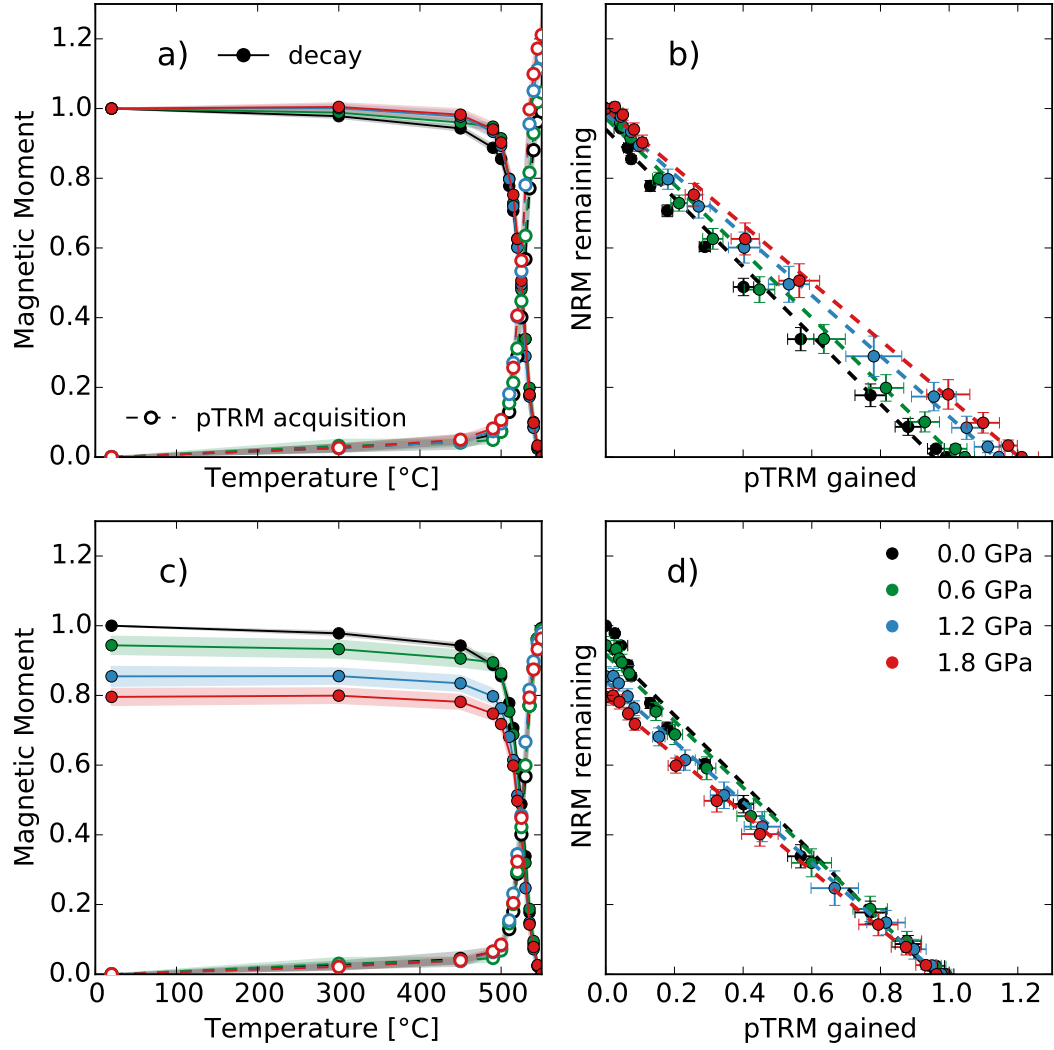


Figure 1.4.: Average thermal demagnetization and acquisition for all 20 hydrostatic experiments **a,b)** normalized to the $NRM(P_n)$ magnetization and **c,d)** normalized to the initial, pre-pressurized $NRM(P_0)$. **b)** and **d)** are the Arai plots corresponding to **a)** and **c)**, respectively; uncertainties are single standard deviations.

one observes a pressure demagnetization effect that mostly influences the lower temperature part of the unblocking spectrum, consistent with experiments by Tikoo et al. [2015]. $NRM(P_n)$ values decrease with increasing pressure, which systematically lowers the paleointensities the same amount as in the first case

because the slopes are lowered in a reciprocal manner.

A third way of analyzing the data would be to normalize the NRM by the magnetization value acquired at the end of the last, in-field paleointensity step, and not to the non-pressure cycled $\text{NRM}(P_0)$. This approach likely yields the most precise understanding of the effect of pressure demagnetization on paleointensity, as it describes the changes relative to the prior pressure step and not to the initial step, e.g., it tracks the incremental changes since the pressures are applied incrementally. Because the samples already experienced one or more pressure cycles, the cumulative demagnetization effect from multiple pressure cycling to some peak pressure would be greater than a single pressure step to the same peak pressure, as analogous to alternating field demagnetization. However, there is only a very slight difference with respect to the second method, so we show only the data normalized by unstressed (initial) $\text{NRM}(P_0)$ value (fig. 1.4c and d).

Paleointensity experiments after pressure cycling (non-hydrostatic stress)

Non-hydrostatic pressures impart deviatoric stresses, which facilitate greater changes in initial to post pressure magnetization beyond that of hydrostatic pressure. Figure 1.5 shows the thermal demagnetization and pTRM acquisition curves and the corresponding Arai-Nagata diagram for the nH experiments. The demagnetization effect can be readily seen in the thermal decay of the NRM normalized to $\text{NRM}(P_0)$ (fig. 1.5a). Small pieces broke off at the rims of most samples during pressure cycling, so we weighed them again to account for the loss in mass when normalizing the magnetizations.

After pressure cycling to 0.6 GPa, the nHx and nHz samples lost $20.9 \pm 7.9\%$ and $29.2 \pm 5.2\%$ of the pre-pressurized NRM moment, respectively (table 1.1). However, the magnetizations in the nHz group recover $4.3 \pm 0.8\%$ upon heating to 300°C , and above 450°C the thermal decay of nHx and nHz follow very similar paths (fig. 1.5a). These results demonstrate that stress demagnetization is more effective when the magnetic moment parallels the maximum compression

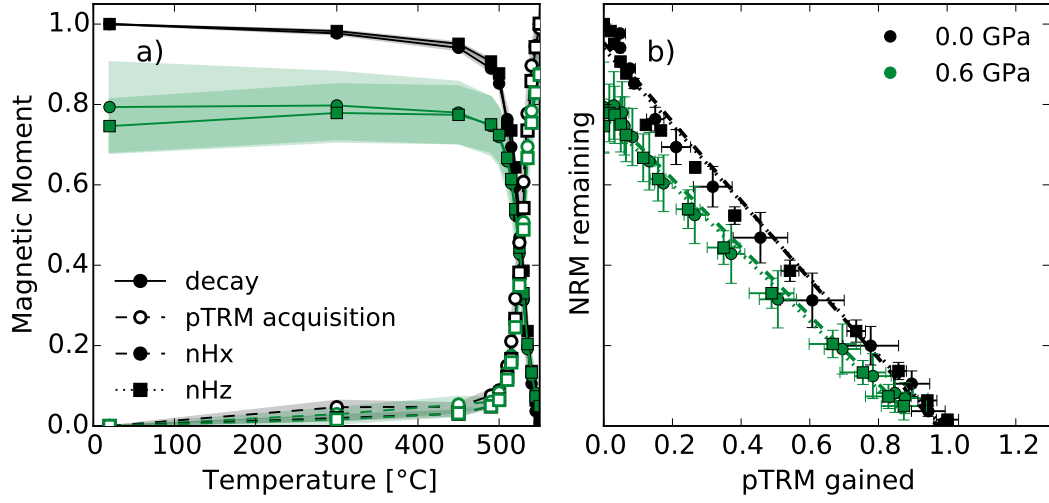


Figure 1.5.: a) Thermal demagnetization and pTRM acquisition when normalized to the initial pre-pressure NRM(P_0) and b) the corresponding Arai-Nagata diagrams for non-hydrostatically (nH) pressure cycled samples either when the maximum stress axis was applied parallel (z) or perpendicular (x) to the magnetization direction. Shaded area and error bars represent one standard deviation. Pressure demagnetization is clearly visible in **a)** which results in a shallowing of the slope and hence, the paleointensity value **b)**.

axis rather than perpendicular to it, whereas pTRM acquisition occurs independently of the compression axis direction relative to the magnetization direction. Paleointensity decreases with pressure (fig. 1.5b), going from $34.6 \pm 1.0 \mu\text{T}$ at 0 GPa to $30.0 \pm 3.0 \mu\text{T}$ at 0.6 GPa ($-13.2 \pm 1.3\%$) for nHx and from $33.6 \pm 1.0 \mu\text{T}$ at 0 GPa to $29.8 \pm 1.0 \mu\text{T}$ at 0.6 GPa ($-11.3 \pm 0.2\%$) for nHz. However, the reduction in paleointensity at 0.6 GPa (-12.5%) is only about half the decrease in NRM moment from stress demagnetization (-25%). Although stress demagnetization exhibits a strong directional dependence, the effect on paleointensity is small due to the recovery of the magnetic moment upon heating in the nHz samples – an effect likely related to thermal annealing. In most cases, q improves with increasing pressure as the curvature becomes less pronounced (fig. 1.5, table 1.1).

Numerical modeling of the pressure cycled paleointensity data

The effect of pressure cycling on thermoremanence can be better understood by plotting the change in magnetization $[M(P_n, T_i) - M(P_0, T_i)]$ relative to the room temperature values of $\text{NRM}(P_n)$ or $\text{NRM}(P_0)$ for the hydrostatic results (averages and standard deviation envelopes of $N = 20$ shown in fig. 1.6). The data in fig. 1.6a and 1.6b represent the differences between the black (P_0) and the colored (P_n) curves in fig. 1.4a and 1.4c, respectively. Figure 1.6a shows the moment normalized to the $\text{NRM}(P_n)$ value, which yields the apparent change in unblocking distribution with pressure due to pressure demagnetization (solid lines) and piezoremanence (dashed lines). Figure 1.6c represents the average unblocking spectra from the 0 and 1.8 GPa runs. It is the relative differences between these two curves that yield the thin red curve in fig. 1.6a. The pressure demagnetization curves increase linearly up to 450°C with a maximum change in unblocking behavior around 500°C and then a decrease above 500°C where after the thermal decay gradually converges with the zero pressure curve near 100% unblocking. Differences become exacerbated with pressure.

Normalization by $\text{NRM}(P_0)$ shows a different facet of the data (fig. 1.6b). Negative (positive) relative differences mean that the magnetic moment after pressure-cycling is lower (higher) than the initial case, again displaying a clear pressure dependency. As fig. 1.6b shows, the differences between the $P_n(1.8 \text{ GPa})$ and $P_0(0 \text{ GPa})$ curves best reflect the change in blocking behavior (pTRM acquisition) due to strain. Because the grains begin in a demagnetized state, changes in the blocking behavior are associated with irreversible changes, such as going from more multidomain to more single domain-like behavior. pTRM acquisition is pressure independent below 500°C whereas significant changes occur above 500°C for all three pressure steps. The lowest pressure (0.6 GPa) provokes the smallest difference, while the two higher pressure steps (1.2 and 1.8 GPa) are fairly similar except for a sharp increase in the 1.2 GPa curve at 530°C which we attribute to an error when setting the temperature on the controller since all samples show the same effect (e.g., the spike arises from all samples and not

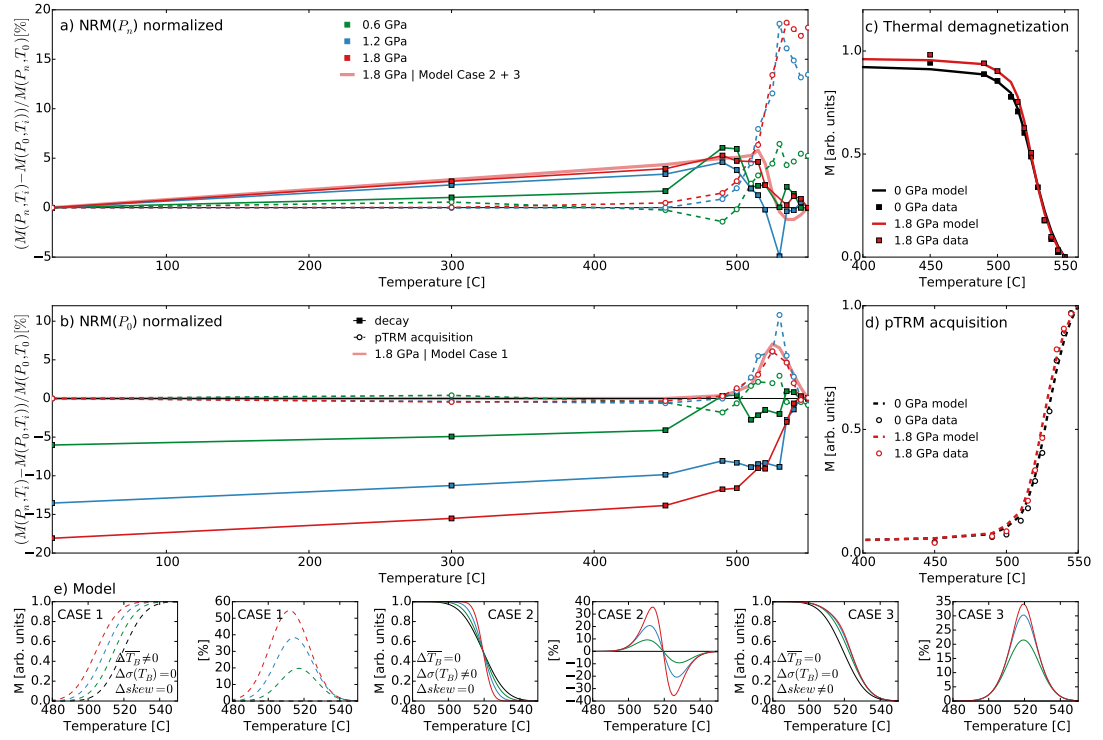
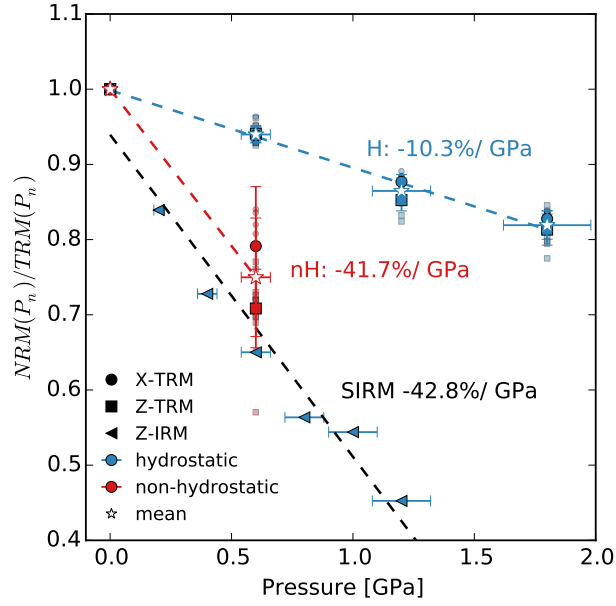


Figure 1.6.: Relative differences between pressure cycled and zero pressure data, calculated from the averages of all hydrostatic samples ($N=20$). Data are normalized to $\text{NRM}(P_n)$ in **a)** and to $\text{NRM}(P_0)$ in **b)**. Dashed lines and open symbols represent the differences of the pTRM acquisition data (blocking) while solid lines represent zero field heating steps (unblocking). **c)** and **d)** show the data used for modeling with points representing the measured data and the lines representing the model, black lines and points show data/model for zero pressure, red is data/model for 1.8 GPa. Plots **e)** represent pTRM acquisition and thermal demagnetization curves calculated from skewed Gaussian distributions of blocking/unblocking temperatures with mean temperature $[T_B]$, distribution width $[\sigma(T_B)]$ and skewness $[\text{skew}]$ and the calculated relative difference of the three cases.

a single outlier). On the other hand, the high degree of similarity between the curves suggests the differences have physical meaning and temperature control is generally precise.

Figure 1.6e represents a simple model explaining the origin of the relative differences by assuming both the blocking and unblocking temperatures follow skewed normal distributions. The curvature in the Arai diagrams indicates that the

Figure 1.7: Magnetic moment normalized to the $TRM(P_n)$ value after pressure demagnetization for both hydrostatic (H) and non-hydrostatic (nH) stresses where the maximum compression axis was applied parallel (z) or perpendicular (x) to the magnetization direction. Stars represent the average values ($N=20$). Uncertainties on pressure are $\pm 10\%$



blocking and unblocking mechanisms follow separate laws, so they should be treated individually [Fabian, 2001]. Figure 1.6e shows how shifts in the blocking or unblocking spectra influence the thermal decay or pTRM acquisition data. Three cases are presented: Case 1 to shift the mean blocking temperature $[T_B]$, Case 2 to broaden or narrow the width of the unblocking temperature distribution $[\sigma(T_B)]$, and Case 3 to alter the skewness [skew] of the unblocking temperature distribution. Each case produces relative differences in the temperature spectra (fig. 1.6e). For Case 1, lowering (raising) the mean blocking temperature results in a positive (negative) relative difference in magnetization with larger amplitudes for larger shifts in temperature. For Case 2, narrowing the unblocking distribution about a constant mean causes a positive-negative peak doublet centered on the mean unblocking temperature of the distribution; the narrower the distribution, the higher the amplitude. For Case 3, skewing the spectra towards higher unblocking temperatures (negative skewness) results in a positive peak centered on the mean unblocking temperature. Skewing toward lower unblocking temperatures (positive skewness) yields the same result except the peaks are negative.

We used a combination of the three cases to model the 1.8 GPa data relative to the 0 GPa hydrostatic data. For this we assume that the sample consists of a single a skewed normal distribution for both the T_B and T_{UB} spectra. Although the samples show narrow blocking and unblocking spectra, it is likely that several different grain populations can describe it. We added a linear component to explain the loss (gain) of magnetic moment in the lower un-blocking (blocking) temperatures. In the first iteration, we fit the cumulative distribution of a skewed normal distribution together with a linear component to the mean of the raw 0 GPa data for thermal demagnetization and pTRM acquisition. This procedure was repeated for the raw data at 1.8 GPa. We then calculated the relative differences. A visual comparison of the fit with the data showed the need for further adjustments of the model. In a second iteration we adjusted the values to better match difference curves in fig. 1.6a and 1.6b. The parameter of the baseline distribution (0 GPa) for thermal decay are $T_{UB} = 520^\circ\text{C}$, $\sigma(T_{UB}) = 20^\circ\text{C}$, skew = -3 and a constant of $-2.3\%/100^\circ\text{C}$ while pTRM acquisition was fit with $T_B = 523^\circ\text{C}$, $\sigma(T_B) = 18^\circ\text{C}$, skew = -3 and constant of $+1.5\%/100^\circ\text{C}$. These led to the black lines (model) connecting the black data points in fig. 1.6c and 1.6d. The same operation was performed for the 1.8 GPa data leading to the red lines (model) connecting the red, measured data points in fig. 1.6c and 1.6d. Although fairly crude, the model provides a simple way to explain changes in the blocking and unblocking spectra, thereby giving a first-order indication of the processes involved.

The modeled differences between the 1.8 and 0 GPa data are plotted as thick red lines over the original data (thin red lines) in fig. 1.6a and 1.6b. For pTRM acquisition, the relative differences between the 1.8 and 0 GPa can be described using case 1 with a -3.0°C shift in blocking temperatures (thick red line in fig. 1.6b). This indicates that pressure cycling causes irreversible changes in the samples blocking spectrum by shifting it toward slightly lower temperatures. Lowering the mean blocking temperature so that it converges with the mean unblocking temperature eliminates curvature of the Arai diagram [Fabian, 2001], consistent with our data (fig. 1.4d and 1.5b). The relative differences of the thermal decay

can be described using a combination of cases 2 and 3, which narrows the distribution width by 1.0°C, decreases skewness by 2, and has a constant linear change of +1.1%/100°C. This suggests two processes are involved in stress demagnetization: one that affects the entire spectrum of unblocking temperatures and a second that mainly skews the population with lower unblocking temperatures while tightening the spread.

Irreversible changes in thermal remanent acquisition can be quantified by comparing the final pTRM acquisition step of one Thellier experiment with the new TRM imposed before pressurization for the next step. The TRM moment after pressure cycling to 0.6 GPa is 3% and 5% greater than that of the 0 GPa TRM moment [$\text{TRM}(P_{0.6}) / \text{TRM}(P_0) = 1.03$ and 1.05] for the hydrostatic and non-hydrostatic groups, respectively. The increase in magnetic remanence acquisition efficiency likely owes its origin to a reduction in domain state, introduction of crystal defects, and/or permanent strain of the crystal lattice as previously postulated [Gilder & Le Goff, 2008]. High reciprocity of the moment as a function of temperature dis- counts chemical alteration as a viable explanation.

1.2.5. Stress effect on remanent magnetizations acquired in strong magnetic fields

Thellier-type paleointensity experiments often produce alteration and are thus avoided in meteorite studies. Instead, relative, non-destructive paleointensity techniques are employed, which rely on giving a sample an artificial magnetization at room temperature, such as a saturation isothermal (direct current) remanent magnetization (SIRM), and then comparing the alternating field demagnetization spectra between the SIRM and the (supposed) TRM [Fuller et al., 1988, Gattacceca & Rochette, 2004]. The paleointensity is derived by assuming a proportionality constant between the two. Whereas Thellier-derived paleointensities are based on physical (Néel) theory, relative paleointensities based on SIRM are not, so comparison between the two should be made with caution. But

because Thellier-based results are more difficult to obtain, relative paleointensity techniques, although inaccurate, may be preferred over no result as an order of magnitude estimate.

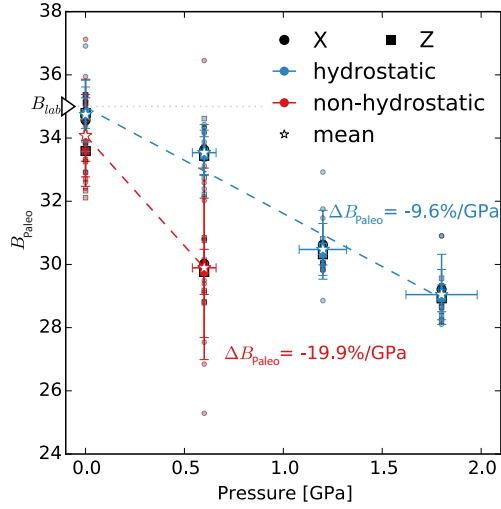
Quantifying the stress demagnetization effect on SIRM-bearing samples was done by exposing samples to a 1.2 T field, measuring their magnetizations, stress cycling the samples under hydrostatic conditions with the piston axis oriented parallel to the magnetization direction (z), and then measuring their magnetizations again¹. The amount of magnetization lost was compared against the stress demagnetized data from TRM-bearing samples for both the hydrostatic and non-hydrostatic cases (fig. 1.7). Demagnetization of the SIRM moment decreases 42.8%/GPa, comparable to demagnetization levels measured on several different rock types with similar domain states [Bezaeva et al., 2007]. This is four times greater than for TRM (- 10.3%/GPa) under like conditions, which is not surprising since a SIRM on single domain and pseudo-single domain grains is also more easily demagnetized than a like population having a TRM [Halgedahl, 1998]. Of interest is that non-hydrostatic stress demagnetization of a TRM is essentially equivalent to that of the hydrostatic stress demagnetization of a SIRM (fig. 1.7), likely because the strain gradient from non-hydrostatic stresses produces a greater effect than hydrostatic stress on one hand and IRM-based magnetizations are more strain sensitive on the other. This implies that pressure demagnetization experiments based on SIRM can be used as an end-member analogy for strain effects on TRM-bearing samples.

1.3. Discussion and Conclusions

Figure 1.8 summarizes the results of the paleointensity experiments. The degree of magnetization loss depends on the level of hydrostaticity: hydrostatic pressure decreases the NRM moment by 10%/GPa while non-hydrostatic pressure has a

¹Alternating field demagnetization of an SIRM moment after pressure cycling can be seen in the Appendix fig. A.1

Figure 1.8: Change in paleointensity as a function of pressure relative to the initial measured value for both hydrostatic and non-hydrostatic stresses where the maximum compression axis was applied parallel (z) or perpendicular (x) to the magnetization direction. Uncertainties are $\pm 10\%$ for pressure; single standard deviation for paleointensity. Stars represent the average paleointensity for each group: red for non-hydrostatic (N=20), blue for hydrostatic (N=20). Small symbols represent paleointensity result for individual samples; large symbols show the averages for x and z separately. Slopes were calculated from least squares fit of the averages.



four times greater effect ($40\%/GPa$). This degree of loss translates into correspondingly lower paleointensity estimates by $10\%/GPa$ for hydrostatic stress and $20\%/GPa$ for non-hydrostatic stress (fig. 1.8). When extrapolated to higher pressures, one would conclude that shock or static pressure above ca. 5 GPa should effectively demagnetize most samples. However, experiments employing stresses well above our peak pressure of 1.8 GPa show the magnetization generally decays with the inverse of pressure [Gattacceca et al., 2007, Gilder et al., 2006], so it remains possible that meteorites exhibiting shock stages above S1 can retain some remanence.

Why the decrease in paleointensity is proportional to stress demagnetization for the hydrostatic case, but only half that for the non-hydrostatic case, can only be partly attributed to recovery of the moment during heating. Although the degree of demagnetization for non-hydrostatic stresses is sensitive to the relative orientation between the maximum compression axis and the remanent magnetization direction, the paleointensity result, and hence the modification in the unblocking/blocking spectra, is not. The fundamental conclusion is that paleointensity results from S1 unshocked meteorites may be appreciably underestimated and should be considered as lower limits. This is particularly clear for hypere-

locity impacts, which eject material from the host body into space, since they have non-negligible and highly variable deviatoric stress components [Pohl et al., 1975].

Thermal decay curves for pressurized and non-pressurized samples are nearly indistinguishable when normalized by $\text{NRM}(P_n)$ (fig. 1.4a); however, normalizing by $\text{NRM}(P_0)$ clearly reveals the stress demagnetization effect (fig. 1.4c). The opposite is true for the piezoremanence effect (fig. 1.4b and 1.4d). Modeling the relative differences with skewed Gaussian distributions together with linear components indicates two distinct processes influence the unblocking spectra: one that affects the entire spectrum of unblocking temperatures and a second that mainly tightens the spread of the fraction with lower unblocking temperatures. Stress demagnetization has a greater influence on the portion of remanence carriers with lower unblocking temperatures, which is increasingly exacerbated with pressure and serves as an indication for the onset of irreversible changes in the remanence carriers. In contrast, the blocking temperature spectrum is much less affected. The net effect lowers the difference between blocking and unblocking thereby reducing the curvature of the Arai diagram.

Besides implications for paleointensity recording in meteorites, our study explains a commonly observed phenomena in paleointensity data on unshocked terrestrial material – namely that one obtains the correct paleointensity result merely by fitting a line on the Arai slope between the first (NRM) and last (full pTRM) points for samples that (1) have only one magnetization component, (2) exhibit no or only a low propensity for alteration, and (3) have curved blocking-unblocking spectra due to the presence of multidomain and/or pseudo-single domain grains [Chauvin et al., 2005, Dunlop, 2005]. The reason for this can be seen in fig. 1.6 where the relative differences in unblocking and unblocking temperature become unity for the fraction with the highest temperatures. As long as the NRM moment has remained constant since remanent acquisition, a paleointensity slope based on the first and final points should yield the correct answer.

Pressure cycling can also be used to correct curved paleointensity data for sam-

ples that have a single magnetization component, do not significantly alter during heating near the Curie temperature and contain a significant proportion of pseudo-single and/or multidomain grains. In such cases, one would measure the NRM, compress the sample to ca. 2 GPa, and then carry out a Thellier experiment. One then normalizes the data by $R(P_n) = \text{NRM}(P_n)/\text{NRM}(P_0)$ and then calculates the slopes on the normalized curves [$B_{\text{Pal}} = B_{\text{lab}} \times |\text{slope}| \times R(P_{n-1})$]. We performed this exercise on the hydrostatically-stressed samples, which resulted in corrected paleointensity values of 35.7 ± 0.6 , 35.3 ± 0.8 and 35.5 ± 0.9 μT for the 0.6, 1.2 and 1.8 GPa results, respectively – well matching the laboratory field of 35.0 ± 0.2 μT . Although encouraging, the method should be further tested on magnetite samples with well-defined size distributions to verify its general applicability.

It would be interesting to repeat the experiments herein on thermally-stable samples possessing different types of remanence carriers (i.e., hematite). Measuring the effect on paleointensity when imposing pressure at elevated temperature, as analogous to basement rocks in meteorite impact craters, may also bear interesting results. Moreover, rocks (terrestrial or extra-terrestrial) displaying linear trends on Arai plots might have their origin in a pressure effect that does not necessarily reflect the ubiquitous presence of single domain particles. In other words, evidence for the presence of large, multidomain grains in a sample yielding linear Arai plots could suggest the sample experienced some degree of stress cycling. An example comes from diamonds with millimeter-sized pyrrhotite inclusions, which one would assume are in the multi-domain range, yet they exhibit single domain-like magnetic properties [Clement et al., 2008]. High-pressure experiments on pyrrhotite show that the effect of strain is to make multi-domain pyrrhotite more single domain-like [Gilder et al., 2011]. These workers calculated that differences in bulk moduli between diamond and pyrrhotite leads to an overpressure of the pyrrhotite inclusions when the diamonds reach the Earth's surface from the mantle. The same could be true for Fe-Ni metal inclusions in olivine, like in the pallasite meteorites described by Tarduno et al. [2012].

2. Low temperature magnetic properties of monoclinic pyrrhotite with particular relevance to the Besnus transition

Abstract

Monoclinic pyrrhotite (Fe_7S_8) owes its ferrimagnetism to an ordered array of Fe vacancies. Its magnetic properties change markedly around 30 K, in what is known as the Besnus transition. Plausible explanations for the Besnus transition are either due to changes in crystalline anisotropy from a reduction in crystal symmetry or from the establishment of a two-phase system with magnetic interaction between the two phases. To help resolve this discrepancy, we measured hysteresis loops every 5° and back field curves every 10° in the basal plane of an oriented single crystal of monoclinic pyrrhotite at 300 K and at 21 temperature steps from 50 K through the Besnus transition until 20 K. Between 50 and 30 K, hysteresis loops possess double inflections between crystallographic a-axes and only a single inflection parallel to the a-axes. Magnetization energy calculations and relative differences of the loops show a six-fold symmetry in this temperature range. We propose that the inflections stem from magnetic axis switching,

which is both field and temperature dependent, in a manner somewhat analogous to an isotropic point where magnetocrystalline constants change their sign. The Besnus transition is best characterized by changes in magnetic remanence and coercivity over a 6° temperature span with a maximum rate of change at 30 K. A surprising yet puzzling finding is that the coercivity ratio becomes less than unity below the transition when four-fold symmetry arises. Because the changes in magnetic parameters are linked to the crystal structure, we conclude the Besnus transition owes its origin to a distortion of the crystallographic axes rather than an apparition of a two-phase system. The saturation magnetization of natural pyrrhotite cycled from room temperature to successively lower temperatures through the Besnus transition decreases 2-4 times less than equivalent grain sizes of magnetite, with less than a 10% loss in remanence between 300 K and 150 K in pseudo-single domain pyrrhotite. As pseudo-single domain monoclinic pyrrhotite carries the magnetic remanence in some meteorites, it is likely that low temperature cycling in space to the Earth's surface will have only a minor influence on paleointensity values derived from those meteorites.

2.1. Introduction

Pyrrhotite refers to a group of non-stoichiometric iron sulfides, Fe_{1-x}S with $0.08 < x < 0.125$, that are important carriers of magnetic remanence in some terrestrial and extraterrestrial rocks. The mineral group has a hexagonal (NiAs type) crystal structure consisting of alternating Fe and S layers. A slight distortion (β from 90° to $\approx 90.4^\circ$) of the crystal lattice in Fe_7S_8 lowers the symmetry from hexagonal to monoclinic, so it is commonly referred to as pseudo-hexagonal [Martin-Hernandez et al., 2008]. Vacancies in the Fe layers lead to different superstructures [Morimoto et al., 1970], with the most iron deficient pyrrhotite (4C) having alternating layers of completely filled Fe sites and layers containing ordered vacancies at an Fe site [Bertaut, 1953]. Sublattice moments couple ferromagnetically within the basal plane while adjacent Fe-layers couple antiferromagnetically.

Regular ordering of vacancies in the basal plane and unequal sublattice moments give rise to ferrimagnetism in monoclinic pyrrhotite [Bertaut, 1953, Néel, 1952, O'Reilly, 1984]. Hexagonal pyrrhotite ($\text{Fe}_{11}\text{S}_{12}$ - Fe_9S_{10}) has equal but opposite sublattice moments at room temperature. Around 220°C, hexagonal pyrrhotite undergoes the so-called lambda transition characterized by a reordering of the vacancy structure that transforms the crystal into a ferrimagnetic monoclinic form with a sharp increase in magnetization [Schwarz & Vaughan, 1972]. Monoclinic pyrrhotite exhibits no lambda transition.

Vacancy ordering produces a strong magnetocrystalline anisotropy in Fe_7S_8 [Bin & Pauthenet, 1963, Martin-Hernandez et al., 2008, Mikami et al., 1959, Sato et al., 1964]. At room temperature, the hard magnetic axis parallels the c-axis while the easy direction resides within the basal plane [Bin & Pauthenet, 1963, Kind et al., 2013]. Magnetic domain observations mainly show 180° domain walls [Halgedahl & Fuller, 1981, Soffel, 1981]. The multidomain (MD) threshold occurs at grain sizes $> 100 \mu\text{m}$ while particles smaller than $2 \mu\text{m}$ are single domain (SD) [Soffel, 1977]; most magnetic parameters show grain size dependencies [Dekkers, 1988, 1989, Menyeh & O'Reilly, 1997].

Monoclinic pyrrhotite undergoes a magnetic phase transition around 30-34 K, called the Besnus transition (T_{Bes}) [Besnus & Meyer, 1964, Dekkers et al., 1989, Fillion & Rochette, 1988]. When cooled in zero field, the transition is marked by a sudden loss of remanent magnetization as well as changes in other magnetic parameters [Dekkers et al., 1989, Kind et al., 2013, Koulialias et al., 2015]. Why the transition occurs is debated. Some workers propose a crystallographic transformation from monoclinic to triclinic [Fillion & Rochette, 1988, Rochette et al., 2011, Wolfers et al., 2011], while others argue for a reorientation of domain structure due to interacting superstructures independent of the 4C superstructure [Charilaou et al., 2015, Kind et al., 2013, Koulialias et al., 2015]. To help elucidate this problem we studied magnetic hysteresis and backfield curves on a single crystal of monoclinic (Fe_7S_8) pyrrhotite in 72 discrete angles at 22 discrete temperatures above, during and below T_{Bes} .

Another reason to study magnetic properties of monoclinic pyrrhotite at low temperatures is that it constitutes a major magnetic mineral in certain types of achondritic meteorites, including Martian meteorites, that potentially carries a record of the ancient magnetic fields on those bodies [Gattacceca & Rochette, 2004, Rochette et al., 2008, 2001, Weiss et al., 2008b, 2002]. A largely unexplored problem is how low temperature cycling in space influences the remanent magnetization of pyrrhotite, which may in turn bias the interpretation of paleointensity data. Weiss et al. [2010] estimated the equilibrium temperature of a rotating meteorite at a distance of 3.5 AU to be ≈ 150 -130 K. Thus, we question how temperature cycling will affect paleointensity estimates if a rock obtained a thermal remanent magnetization by cooling through the Curie temperature down to an equilibrium temperature of ≈ 150 K then subsequently arrived on the Earth's surface and warmed to ≈ 300 K. Dunlop [2003] carried out low temperature cycling experiments on nine size fractions of magnetite (Fe_3O_4) where it was found the amount of demagnetization strongly depends on particle size. We followed this example by studying the low temperature cycling of natural pyrrhotite bearing rocks with different magnetic domain states to assess the potential implications for meteorites.

2.2. Materials, Methods and Results

2.2.1. Samples

The Munich Mineralogical State Collection (Mineralogische Staatssammlung München) provided us with a single crystal of monoclinic pyrrhotite (sample MSM17591) to study the Besnus transition. It yielded a Curie temperature of 311 °C (Petersen Instruments, variable field translation balance, Univ. Munich) with no trace of a lambda transition. We drilled a disk from the single crystal measuring 2.6 mm in diameter and 0.75 mm in height – paying close attention that the disk was as circular as possible.

A JEOL 6500 field emission gun outfitted with an HKL electron backscatter diffraction detector (Univ. Minnesota) determined the sample's crystallography using an operating voltage of 20 kV and a working distance of 14.8 mm. Diffraction patterns were indexed using Channel 5 software with a monoclinic crystal structure described by Tokonami et al. [1972] and Powell et al. [2004]. Crystallographic solutions were accepted only if the mean angular deviation value was less than 1.4° . Measurements of elemental abundances were collected using an accelerating voltage of 15 kV at a working distance of 10.0 mm. Spot energy dispersive spectroscopy measurements were collected with a Thermo-Noran Vantage microanalysis system. The diameter of the interaction volume for elemental measurements is ca. $2.0\text{ }\mu\text{m}$ for oxide and sulfide minerals. Matrix correction coefficients (Z, A and F) were calculated using the $\Phi(\text{Rho}^*z)$ method of Pouchou & Pichoir [1984] and Bastin & Heijligers [1991]. X-ray spectra were collected using counting times of 60 s and a probe current of 20 nA.

The electron backscatter diffraction data show the c-axis of the MSM17951 pyrrhotite is oriented almost normal (77°) to the sample's surface. We arbitrarily defined one of the a-axes to be $a_1=0^\circ$. With reference to this axis, the c-axis trends 286° and the two other a-axes lie close to expected pseudo hexagonal structure directions that trend $a_2=57^\circ$ and $a_3=116^\circ$ with respect to a_1 . There is no evidence for twinning, intergrowths or mineral inclusions. Nine spot energy dispersive spectra yield an average composition of $47.4\pm0.7\text{ at\% Fe}$ and $52.6\pm0.7\text{ at\% S}$, corresponding to a bulk chemical composition of $\text{Fe}_{7.2\pm0.2}\text{S}_8$.

The samples used for the temperature cycling experiments comprise three pyrrhotite-bearing gneiss samples from the Kirchzarten deep drilling project in the Black Forest, Germany [Pucher & Fromm, 1985] and a pure polycrystalline pyrrhotite sample (MSM73410) courtesy of the Mineralogical State Collection. Mössbauer spectra, magnetic hysteresis, Curie and Besnus temperature measurements for MSM73410 were reported in Gilder et al. [2011]. Thermomagnetic curves measured with a Petersen Instruments variable field translation balance define Curie temperatures of $319\pm5^\circ\text{C}$ for the three samples from the gneisses and 322°C for

MSM73410, typical of pure monoclinic pyrrhotite [Dunlop & Özdemir, 1997]. No lambda-transition or Curie temperatures corresponding to magnetic phases other than pyrrhotite were detected.

2.2.2. Rock Magnetic Measurements

Magnetic hysteresis loops and backfield curves were measured to maximum fields of 1.5 T with a Princeton Instruments vibrating sample magnetometer to obtain remanent saturation magnetization (M_{rs}), saturation magnetization (M_s), bulk coercive force (B_c) and the coercivity of remanence (B_{cr}) (fig. 2.1; table 2.1). Figure 2.1c plots the room temperature (300 K) remanence (M_{rs}/M_s) and coercivity (B_{cr}/B_c) ratios together with specific size fractions of pyrrhotite studied by Dekkers [1988]. The three samples from the deep bore hole have relatively high remanence ratios ≈ 0.4 and low coercivity ratios (< 1.5) typical of pseudo single domain pyrrhotite with grain sizes $< 35 \mu\text{m}$. MSM73410 and MSM17591 have lower M_{rs}/M_s and higher B_{cr}/B_c characteristic of multidomain pyrrhotite with grain sizes $> 200 \mu\text{m}$ [Dekkers, 1988]. Grain sizes listed in Table 1 for the multidomain-rich pyrrhotite was estimated by extrapolating the Dekkers [1988] data.

Hysteresis parameters are markedly different above and below T_{Bes} (table 2.1; fig. 2.1), consistent with previous work [Dekkers et al., 1989, Kind et al., 2013]. At low temperatures the multidomain crystals act more single domain like. From our limited data, there seems to be a linear relationship between the remanence ratio and B_c with respect to grain size (fig. 2.1d inset).

For the low temperature demagnetization experiments, each sample was initially magnetized in a 1 T magnetic field to produce a room temperature ($T_0 = 300$ K) saturating isothermal remanent magnetization (SIRM). The specimens were cycled from T_0 to approximately one of eight temperatures ($T_i = 200, 150, 120, 90, 60, 40, 30$ and 20 K) and then warmed back to T_0 . Magnetic moments were measured in 5 K intervals in a null field. For each cycle, magnetization decreases

Table 2.1.: Room temperature and 20 K results of hysteresis and backfield measurements. T_B was calculated from the maximum inflection of $dM(T)/dT$ except for MSM17591 where it was calculated from the maximum inflection in $dB_c(T)/dT$ marked by *.

Sample (\approx size)	T_c ($^{\circ}\text{C}$)	T_B (K)	$M_s(\text{Am}^2/\text{kg})$		$M_{rs}(\text{Am}^2/\text{kg})$		M_{rs}/M_s		$B_c(\text{mT})$		$B_{cr}(\text{mT})$		B_{cr}/B_c 300K
			300 K	20 K	300 K	20 K	300 K	20 K	300 K	20 K	300 K	300 K	
P167 (15 μm)	325	29	0.35	0.44	0.15	0.21	0.42	0.48	18.7	151.9	20.4		1.09
P512 (30 μm)	314	31	0.64	0.79	0.28	0.47	0.43	0.59	20.4	164.0	22.0		1.08
P527 (35 μm)	317	30	0.27	0.29	0.12	0.19	0.42	0.65	20.6	134.8	22.4		1.09
MSM73410 (0.5 mm)	322	29	16.79	16.01	1.74	10.6	0.10	0.66	5.0	64.9	7.8		1.56
MSM17591 (1.6 mm)	311	30*	21.04	20.48	0.81	15.7	0.04	0.77	1.4	54.9	3.5		2.50

44 2. Low temperature magnetic properties of monoclinic pyrrhotite

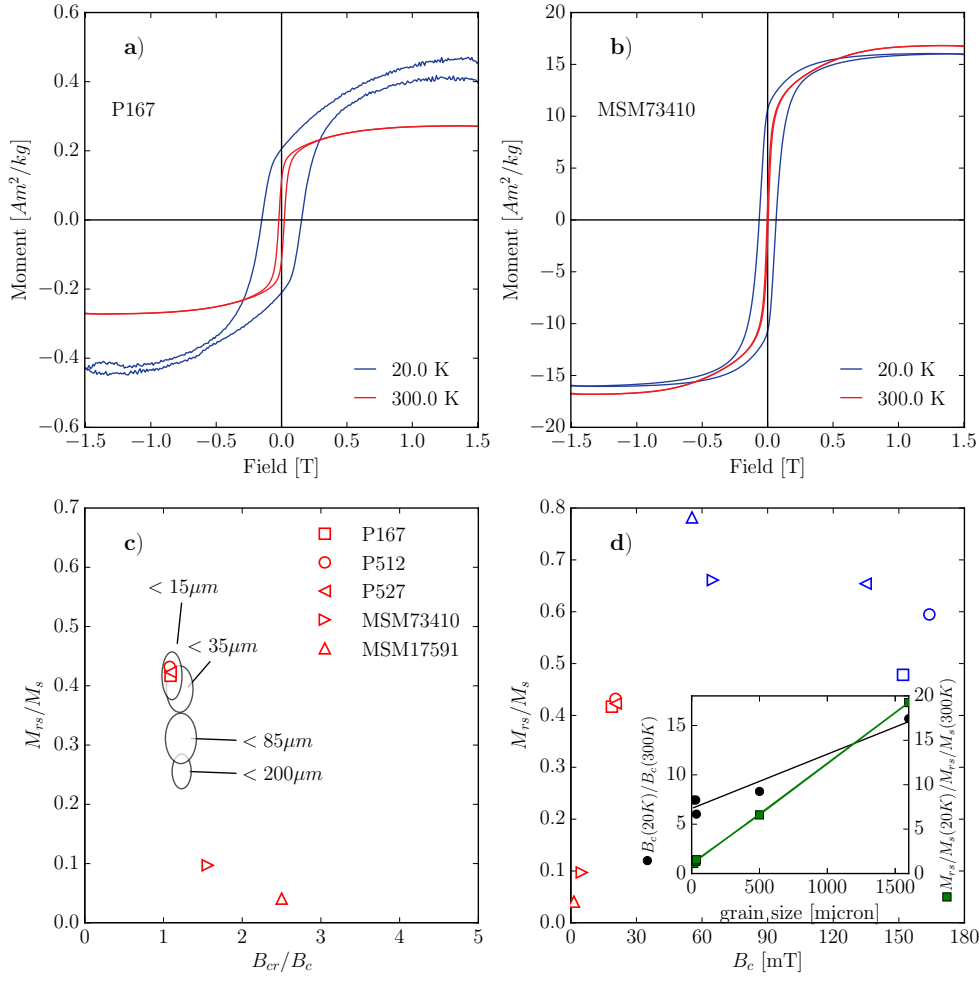


Figure 2.1.: Hysteresis loops measured at 300 K and 20 K for samples that are a) pseudo-single domain (P167) and b) multidomain (MSM73410) rich pyrrhotite after correction for paramagnetic contribution. c) Day et al. [1977] plot for pyrrhotite measured at 300 K. Ellipses represent fields measured from constrained size populations (as indicated, two standard deviations) of pyrrhotite powder from Dekkers [1988]. b) Comparison of the remanence ratio (M_{rs}/M_s) vs. bulk coercivity (B_c) measured at 300 K (red points) and 20 K (blue points). Inset shows the relative change in B_c and M_{rs}/M_s as a function of grain size.

a few percent upon initial cooling from 300 K and then slightly increases before decreasing again upon further cooling (fig. 2.2). A positive inflection coincides with changes in crystalline anisotropy constants that achieve maximum values around 200 K [Bin & Pauthenet, 1963].

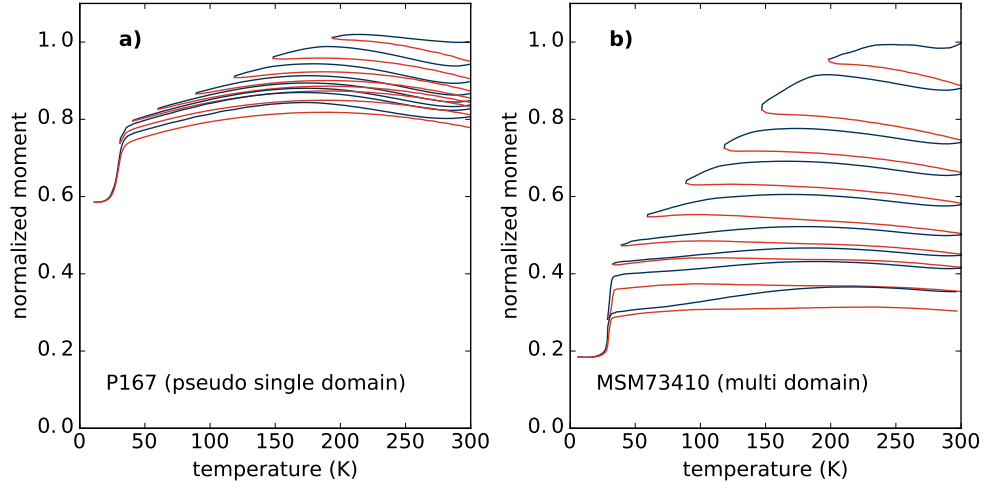
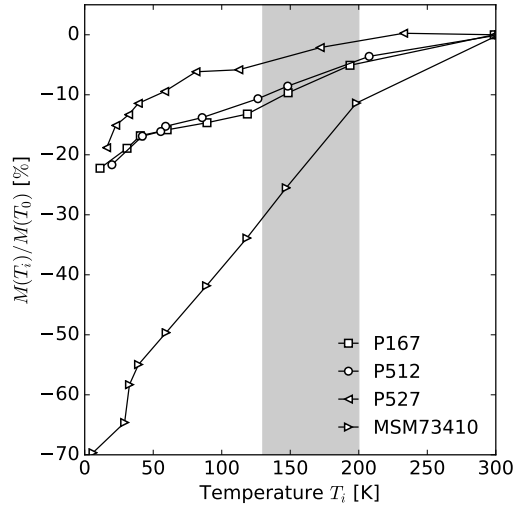


Figure 2.2.: Continuous cooling/warming measurements for a) pseudo-single domain rich pyrrhotite and b) multidomain rich pyrrhotite. Blue lines are cooling paths from $T_0 (=300 \text{ K}) \rightarrow T_i$; red lines show warming back to 300 K.

The main difference between pseudo-single domain and multidomain-dominated samples upon low temperature cycling is the relative loss in magnetization, which is significantly less in pseudo-single domain than in multidomain bearing samples (fig. 2.2). In contrast to magnetite, the curves are not reversible and do not follow the previous warming path when cycling to a lower temperature [Dunlop, 2003]. The greatest loss in remanence occurs at the Besnus transition (T_{Bes}). Defined by the maximum in dM/dB calculated from the cooling path of the final $T_0 \rightarrow T(20 \text{ K})$ cycle, T_{Bes} averages $29.8 \pm 0.6 \text{ K}$ (table 2.1), consistent with reported values (30-34 K) [e.g. Rochette et al., 1990].

Figure 2.3 plots the remaining fraction of initial magnetization after cycling from $T_0 \rightarrow T_i \rightarrow T_0$ as a function of T_i , again showing that demagnetization levels are grain size dependent. Linear regression of the magnetization loss for $T_i > T_{\text{Bes}}$ for the pseudo-single domain samples averages $-7\%/100^\circ\text{C}$ whereas that for the multidomain sample is roughly four times greater ($-27.8\%/100^\circ\text{C}$). For temperature cycling to 150 K from 300 K, pseudo-single and multidomain magnetite lose much more magnetization (45% and 55%, respectively; [Dunlop, 2003]) in comparison to pyrrhotite (10% and 25%). Moreover, thermal remanent magne-

Figure 2.3: Stepwise demagnetization of saturating isothermal remanent magnetization (SIRM). A room temperature SIRM was cycled from $T_0 \rightarrow T_i \rightarrow T_0$. The recovered magnetization at room temperature is plotted as a function of T_i . Shaded area shows likely equilibrium temperatures of a rotating meteorite at 3.5 AU distance from the sun.



tization in pseudo-single domain magnetite is harder (demagnetizes less than) to low temperature demagnetization than an SIRM [Dunlop, 2003]. If the same is true for pyrrhotite, then paleointensity estimates from meteorites whose magnetizations are carried by single to pseudo-single domain pyrrhotite should be lowered by less than 10% when temperature cycled to 150 K.

A pronounced inflection is visible in the demagnetization curves at the Besnus transition. Dekkers et al. [1989] cooled several differently sized pyrrhotite crystals to 4.2 K through the Besnus transition – and warmed them back to room temperature. They calculated the ratio R_{rec} defined as the recovered remanence at 300 K after a full 4.2 K cycle. They found the magnetization retained after cooling to be grain size dependent, with smaller particles retaining more magnetization than larger ones. Comparing the remanence recovered after cycling to 20 K, the rock samples show a similar recovery than the range of $< 35 \mu\text{m}$. The large crystal however recovers less than the largest sample studied by Dekkers et al. [1989]. For a sample that had been cycled through the transition, and then cycled a second time, the recovery could be erroneously interpreted as a sign of a sample rich in single or pseudo-single domain particles.

2.2.3. Hysteresis parameters as a function of direction and temperature

In order to better understand the mechanism controlling the Besnus transition, we measured hysteresis loops and backfield curves at one or two degree intervals from 50 to 20 K as well as at 300 K along 72 directions in the basal plane of the single crystal. Hysteresis loops were corrected for field and moment offsets following von von Dobeneck [1996]. In order to remove potential bias from misalignment or field offsets inside the magnetometer, we assumed that the measurements along antipodal directions ($\pm 180^\circ$) were equal and averaged their moments. The sample was never removed from the magnetometer during the entire course of the experiments in order to avoid potential sample misalignment.

When measured along one of the crystallographic a-axes at 300 K, the moment sharply increases below 25 mT then gradually approaches saturation in a fairly curved manner (blue curve in fig. 2.4a). Rotating the sample 30° in-between two a-axes (green curve in fig. 2.4a) results in a lower initial rise < 25 mT in moment followed by a steeper approach to saturation. That M_s is not identical in all directions at some temperatures suggests 1.5 T does not always fully saturate the sample; hence, the moment at 1.5 T will be referred to as pseudo- M_s (M_s^*). The lowest and highest values for M_s^* (20.8 and 21.2 Am²/kg) at 300 K lie within the range of reported values (18.3-21.2 Am²/kg) [Kind et al., 2013, O'Reilly et al., 2000]. Except for the steep initial rise in moment < 25 mT that persists at all temperatures, the character of the hysteresis loops change considerably within the basal plane above (fig. 2.4b), during (fig. 2.4c) or below (fig. 2.4d) T_{Bes} . Each case is discussed separately below.

2.2.4. Temperatures above T_{Bes} (> 34 K)

The curvature in the hysteresis loops along the a-axes diminishes considerably approaching T_{Bes} (blue curve in fig. 2.4b) whereas an intriguing double inflection arises between a-axes (green curve in fig. 2.4b). Loops with double inflections

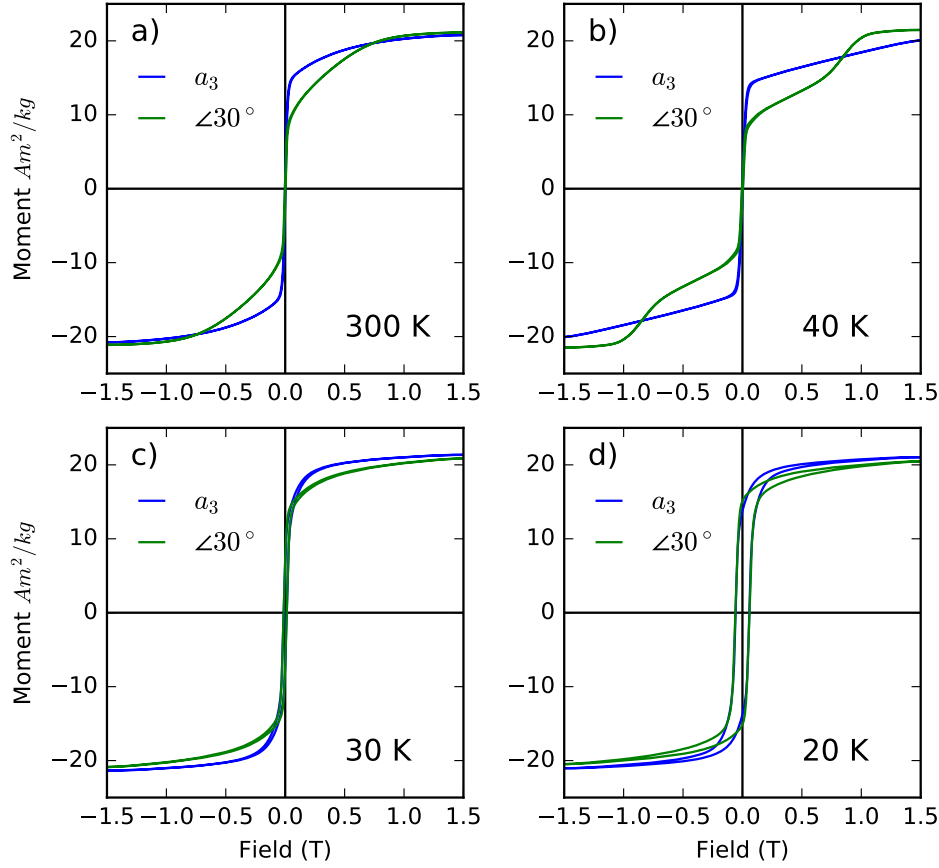


Figure 2.4.: Hysteresis loops of MSM17591 at a) 300 K, b) 40 K, c) 32 K and d) 20 K measured along the crystallographic a-axis (blue) and at an angle 30° away from the a-axis (green).

appear with six-fold symmetry between a-axes, although one direction (160° - 340°) is more pronounced than the other two. The closer the measurement direction is to an a-axis, the higher the field at which the inflection appears (B_{inf}) and the less pronounced it becomes. Defining B_{inf} by the peak in dM/dB of the downfield branch shows B_{inf} increases from 740 mT at 50 K to 780 mT at 40 K. Below 40 K, the peak rapidly disappears with a progressive decrease in B_{inf} from 700 mT at 36 K to 300 mT at 33 K before disappearing at 32 K. M_s^* is higher where the double inflection is most pronounced (fig. 2.4b). Koulialias et al. [2015] also found a double inflection in a single crystal of Fe_7S_8 ; however, they measured their sample only in one direction, most likely between a-axes, which made it

impossible to see the directional dependence of the inflection. Koulialias et al. [2015] noted a shift in B_{inf} from 500 mT at 200 K to 750 mT at 40 K, the latter being consistent with our new results.

Normalizing the hysteresis parameters to their maximum and minimum values more clearly shows their expression as a function of measurement angle (fig. 2.5). At $50 \geq T > T_{\text{Bes}}$ all maxima in hysteresis parameters fall between crystallographic axes. M_s^* peaks at 155° , 25° away from a crystallographic a-axis, similar to the findings of Wolfers et al. [2011]; the minimum in M_s^* lies at 120° , nearest to the a-axis that projects in the c-axis direction (106°). All local minima in M_s^* trend close to crystallographic a-axes, with six-fold symmetry. Between 300 and 34 K the six fold symmetry persists and the average M_s^* stays constant although the maxima and minima are more pronounced at 50 K then below according to the standard deviation of 36 M_s^* values (table 2.2). The maximum in bulk coercivity (B_c) (2.0 mT) occurs near the M_s^* maximum while the minimum in B_c (1.2 mT) is orthogonal with a uniaxial expression. B_c and B_{cr} maxima nearly coincide at 300 K. At 50 K and below, B_c and B_{cr} maxima diverge, with B_c trending nearly parallel to M_s^* while B_{cr} maximizes at the a-axis that coincides nearest to the c-axis with a second maxima in another a-axis direction. Saturation remanence (M_{rs}) defines two maxima at 300 K: a sub-maximum ($1.18 \text{ Am}^2/\text{kg}$) parallel to the c-axis and the maximum ($1.28 \text{ Am}^2/\text{kg}$) orthogonal to it. By 50 K and below, the sub-maximum in M_{rs} disappears and lies squarely between two a-axes.

2.2.5. Temperatures within T_{Bes} (34-28 K)

Hysteresis loops and hysteresis parameters, except for M_s^* and B_{rh} (the median destructive field of remanent hysteresis [von Dobeneck, 1996]), change markedly between 34 and 28 K (table 2.2; fig. 2.4c and 2.6). M_s^* slightly, yet almost imperceptibly, increases through the transition with a minimum in standard deviation at 34 K; the standard deviation for B_{rh} is lowest at 31 K. B_c and M_{rs} increase prominently across T_{Bes} , which best define the transition temperature region with both dB_c/dT and dM_{rs}/dT showing maxima at 30 K for all angles. We conclude

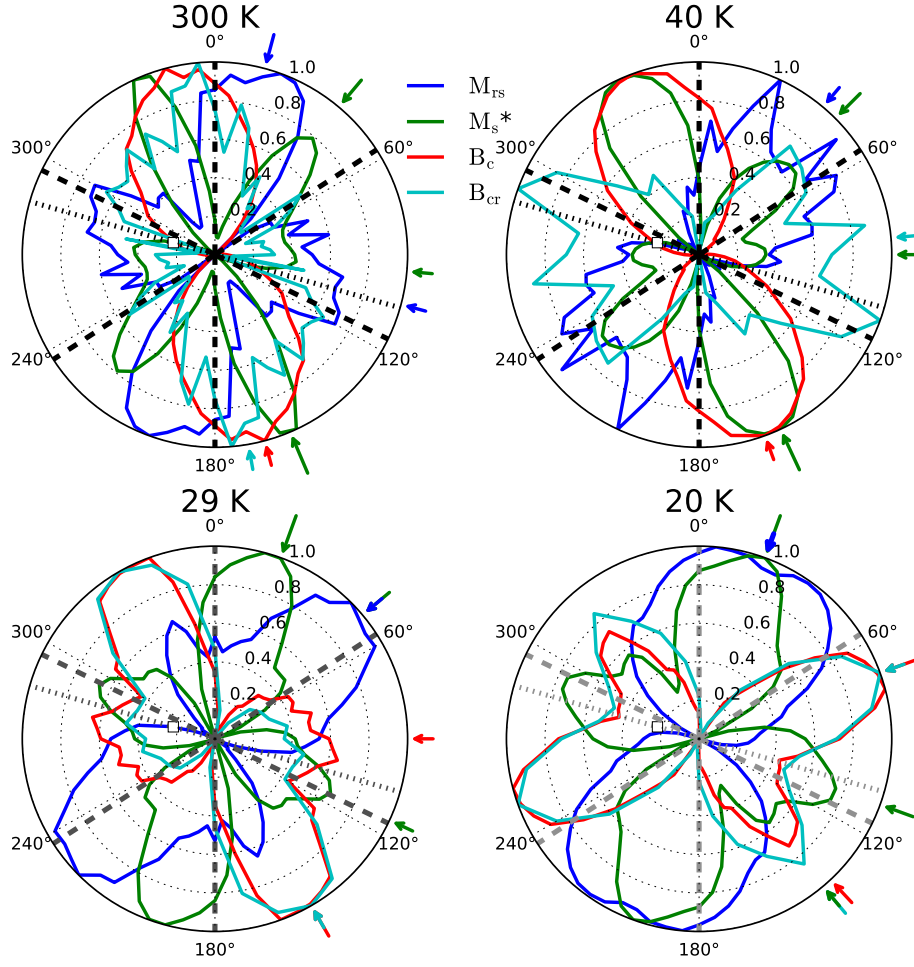


Figure 2.5.: Magnetic hysteresis and backfield parameters normalized by their minimum and maximum values at four discrete temperatures. Arrows point towards the maxima or sub-maxima of each parameter at a given temperature. Black and grey dashed lines indicate the crystallographic a-axes measured at 300 K. These lines become grey at 29 K and 20 K as the six-fold symmetry transforms into four-fold symmetry. Dashed lines and grey square trending 286° represent the c-axis and its projection on the [100] plane. Normalized and non-normalized for all temperatures can be found in the appendix (fig. A.3 and A.4)

that these two parameters best define the transition temperature yet the transition itself spans about 6 K. Within the transition, maxima in B_{cr} and B_c parallel each other between two a-axes; M_s rotates ca. 60°, closer into coincidence with M_{rs} (fig. 2.5).

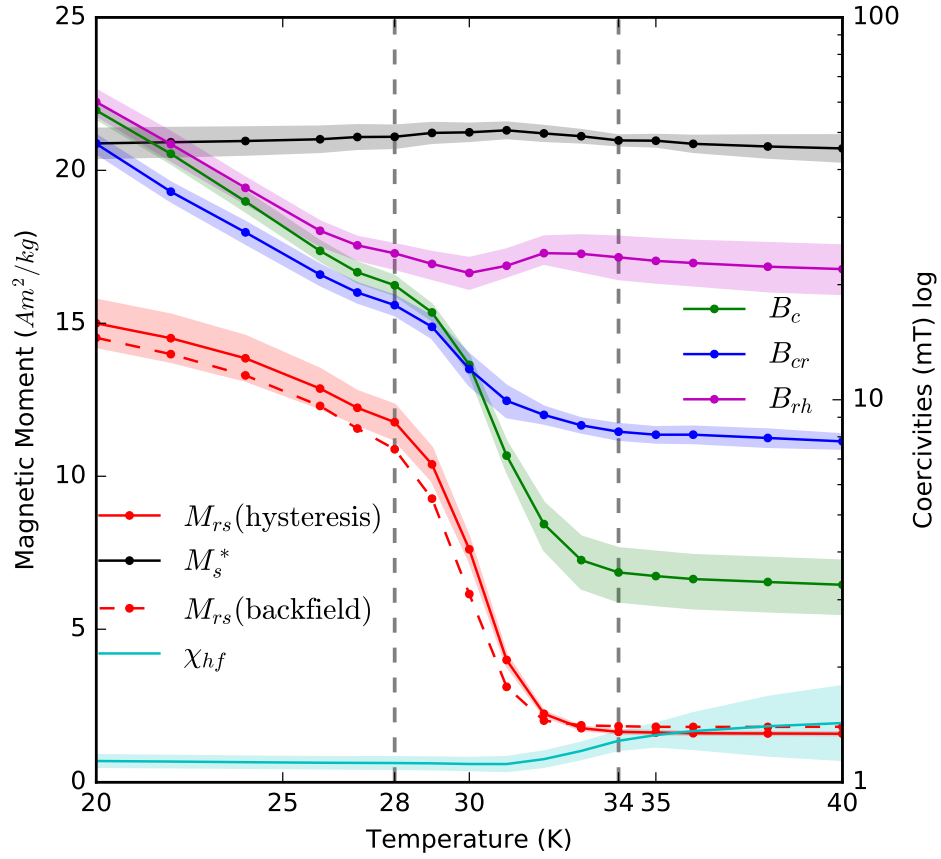


Figure 2.6.: Average hysteresis parameters for 72 hysteresis and 36 backfield measurements between 40 and 20 K. Shaded regions show one standard deviation. Vertical lines represent the Besnus transition temperature range as defined in the text. Dashed line shows SIRM ($= M_{rs}$) values calculated from the backfield measurements, uncertainty envelope omitted for clarity. Coercivities (B_c , B_{cr} , B_{rh}) are plotted on a log scale.

Surprisingly B_c increases faster than B_{cr} , and by 30 K, B_{cr} actually becomes lower than B_c thereby reducing the coercivity ratio below unity. To our knowledge, this is the first time a coercivity ratio below unity has been reported, which leads one to question whether it is due to an experimental artifact. However, this observation is highly reproducible, being based on 360 backfield measurements with corresponding hysteresis loops. Although an offset in field or magnetic moment could lower B_{cr} values, the bias would have to be very large (up to 20% B_{cr}) to underestimate a field of ≈ 11 mT at 20 K.

Another possible explanation is a faulty temperature measurement. To test this, we measured hysteresis loops and backfield curves in different sequences but still found lower B_{cr} values. Moreover, measurements between 20 and 29 K in two different angles on a vibrating sample magnetometer at the University of Munich yielded the same conclusion: coercivity ratios below unity.

Backfield curves of a non-saturated sample could lead to an underestimate of B_{cr} . Although the value for M_{rs} obtained from backfield measurements (dashed red line in fig. 2.6) is slightly lower than M_{rs} calculated from hysteresis loops below 33 K, correcting the backfield curve for this difference cannot account for the coercivity ratio lying below unity. In many cases the backfield curve would have to be corrected by such a large amount (40% at 20 K), that M_{rs} determined from backfield measurements would well exceed (ca. 25% at 20 K) M_{rs} derived from hysteresis loops. Furthermore, the high field susceptibility (χ_{hf}), calculated from a linear regression of the moments at $|B| \geq 1.3$ T decreases at 33 K which indicates that the sample is closer to saturation than at temperatures above the transition (fig. 2.6). In sum, we find no experimental grounds to explain away the observation that B_{cr}/B_c is less than 1 below T_{Bes} .

2.2.6. Temperature below T_{Bes} (< 28 K)

Hysteresis loops widen appreciably below T_{Bes} as B_c increases markedly (fig. 2.4d) and the symmetry changes from six to four fold (see below). Measurement directions in between two a-axes lose the double inflection and show a more gradual approach to saturation. Maxima in B_c and B_{cr} remain parallel, yet lie nearly orthogonal to their pre- T_{Bes} directions and exhibit distinct sub-maxima (fig. 2.5). Both develop a second peak at $\approx 80^\circ$. The maxima of M_s^* aligns perpendicular to the c-axis projection. Saturation remanence continues to increase below 28 K, but at a lower rate than during the transition (fig. 2.6), while coercivity increases linearly when plotted on log scale.

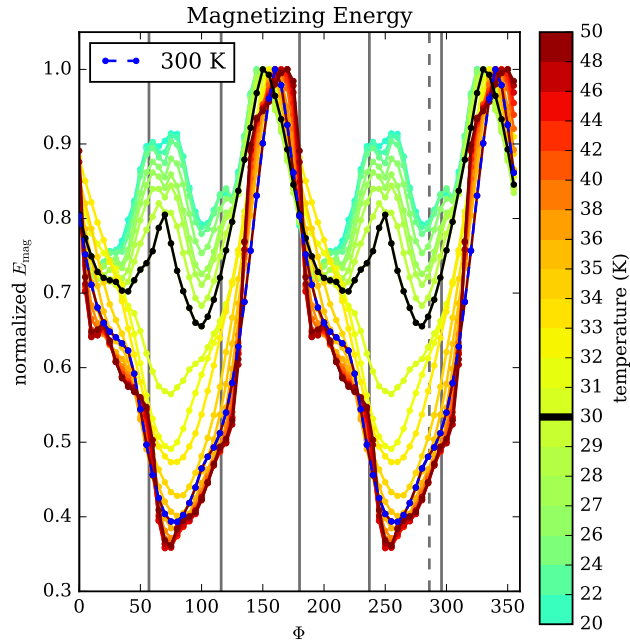
Table 2.2.: Mean results calculated from all measurement directions. $N=72$ for M_s , M_{rs} , B_c and $n=36$ for B_{cr} . Backfield curves have not been measured for temperatures > 40 K. Errors are one standard deviation.

T (K)	M_{rs}	M_s	M_{rs}/M_s	B_{cr}	B_c	B_{cr}/B_c
300	1.16 ± 0.04	20.96 ± 0.11	0.06 ± 0.002	2.92 ± 0.34	1.52 ± 0.29	1.96 ± 0.24
50	1.79 ± 0.08	20.73 ± 0.53	0.09 ± 0.004		3.24 ± 0.48	
48	1.73 ± 0.07	20.66 ± 0.53	0.08 ± 0.004		3.18 ± 0.47	
46	1.58 ± 0.05	20.72 ± 0.52	0.08 ± 0.003		3.13 ± 0.49	
44	1.58 ± 0.04	20.74 ± 0.51	0.08 ± 0.003		3.18 ± 0.51	
42	1.58 ± 0.04	20.70 ± 0.48	0.08 ± 0.003		3.23 ± 0.51	
40	1.58 ± 0.04	20.72 ± 0.43	0.08 ± 0.003	7.79 ± 0.32	3.28 ± 0.52	2.44 ± 0.45
38	1.59 ± 0.05	20.79 ± 0.36	0.08 ± 0.003	7.94 ± 0.42	3.33 ± 0.53	2.44 ± 0.43
36	1.60 ± 0.04	20.87 ± 0.26	0.08 ± 0.002	8.12 ± 0.38	3.39 ± 0.54	2.45 ± 0.42
35	1.62 ± 0.05	20.97 ± 0.19	0.08 ± 0.002	8.10 ± 0.38	3.46 ± 0.55	2.40 ± 0.40
34	1.64 ± 0.05	20.97 ± 0.16	0.08 ± 0.002	8.27 ± 0.37	3.53 ± 0.56	2.39 ± 0.38
33	1.77 ± 0.05	21.11 ± 0.20	0.08 ± 0.003	8.58 ± 0.36	3.80 ± 0.59	2.30 ± 0.33
32	2.24 ± 0.08	21.20 ± 0.24	0.11 ± 0.004	9.13 ± 0.46	4.72 ± 0.66	1.96 ± 0.19
31	4.00 ± 0.18	21.30 ± 0.25	0.19 ± 0.009	9.96 ± 0.94	7.15 ± 0.63	1.39 ± 0.05
30	7.61 ± 0.38	21.24 ± 0.28	0.36 ± 0.019	12.04 ± 1.13	12.38 ± 0.64	0.97 ± 0.05
29	10.39 ± 0.54	21.22 ± 0.32	0.49 ± 0.028	15.54 ± 1.01	16.94 ± 0.80	0.92 ± 0.02
28	11.77 ± 0.57	21.09 ± 0.36	0.56 ± 0.031	17.71 ± 1.02	19.95 ± 1.12	0.89 ± 0.02
27	12.24 ± 0.54	21.08 ± 0.38	0.58 ± 0.031	19.10 ± 1.09	21.58 ± 1.26	0.89 ± 0.02
26	12.87 ± 0.64	21.01 ± 0.41	0.61 ± 0.034	21.28 ± 1.27	24.56 ± 1.42	0.87 ± 0.02
24	13.86 ± 0.73	20.95 ± 0.44	0.66 ± 0.037	27.44 ± 1.75	33.09 ± 1.95	0.83 ± 0.01
22	14.51 ± 0.77	20.91 ± 0.46	0.69 ± 0.037	35.04 ± 1.94	43.96 ± 2.39	0.80 ± 0.01
20	15.00 ± 0.77	20.87 ± 0.47	0.72 ± 0.036	46.75 ± 2.48	57.11 ± 2.72	0.82 ± 0.01

2.2.7. Symmetry considerations

The magnetic easy and hard axes corresponds to the direction with the lowest and highest magnetization energies [Dunlop & Özdemir, 1997]. In order to calculate the crystalline anisotropy, the maximum applied field during the course of a hysteresis loop should exceed the anisotropy field, otherwise the crystal will not become fully saturated. Although 1.5 T does not quite saturate the crys-

Figure 2.7: Normalized magnetizing energy calculated by integrating over all moments of the descending branch at positive fields. Lines show the crystallographic a-axes with respect to the a_1 -axis at 0° . The dashed line shows the projection of the crystallographic c-axis on the basal plane. Room temperature values in blue. Unnormalized magnetizing energies can be seen in fig. 2.10 in the appendix of this chapter



tal, we calculated the magnetizing energy ($E_{Mag} = \int_0^{M_s^*} B dM$) from the positive downfield branch for all angles and temperatures. Figure 2.7 plots the normalized magnetizing energy as a function of angle in the basal plane; Supplemental fig. 2.10 (in appendix of this chapter) shows the unnormalized values. While these energies cannot be used to calculate the anisotropy constants, they can indicate the position of the easy axis within the basal plane when the energy attains a minimum. The maximum energy does not indicate the hard axis as it lies perpendicular to the basal plane—at least above T_{Bes} [Bin & Pauthenet, 1963]. Only one dominant easy axis exists above the transition, trending about 20° away from the a_2 -axis. M_s is directionally independent in a fully saturated sample; however, it is interesting that the maximum energy coincides with the maximum of M_s^* and B_c at 160° . The easy axis stays constant to within $\pm 5^\circ$ until 30 K and then abruptly rotates 25° . Both the mean energy as well as the difference between minimum and maximum energy states decrease. The location of the minimum energy at 300 K converts at 30 K into a local maximum with two local minima occurring below T_{Bes} , likely indicative of two, orthogonal easy axes.

The rotational symmetry of the second inflection in the hysteresis loops (fig. 2.4b)

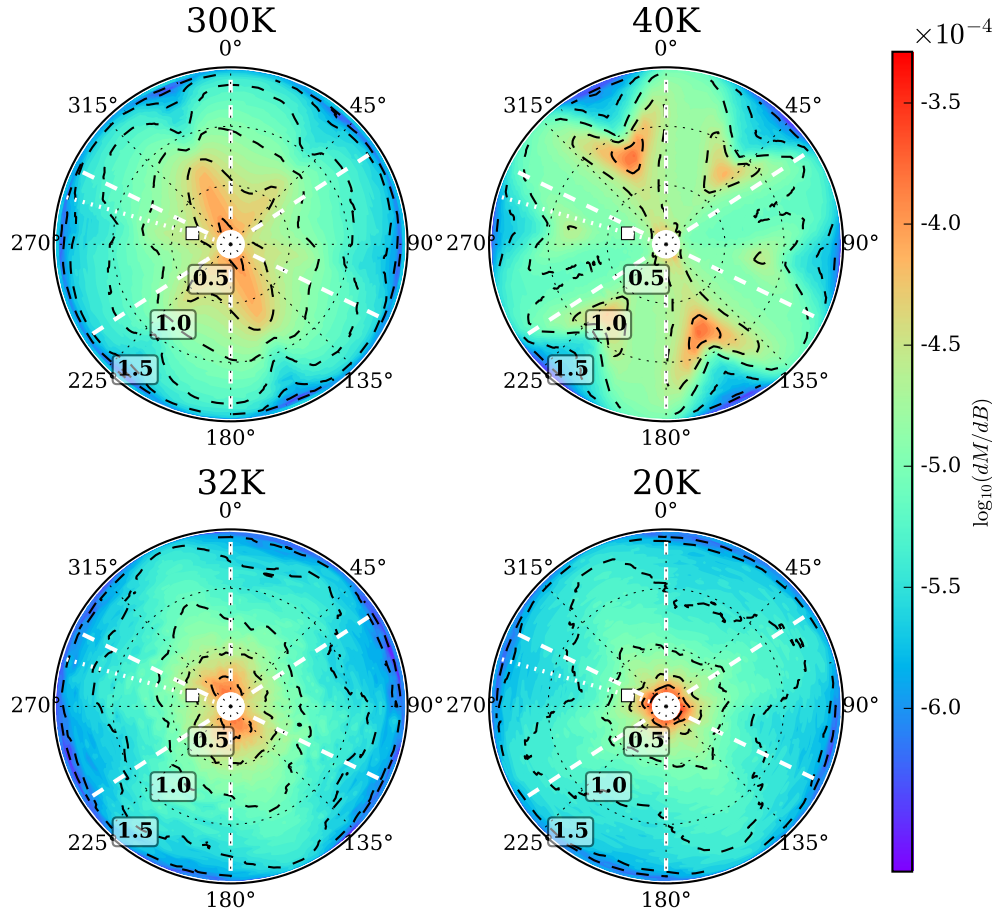


Figure 2.8.: Angular dependence of the first derivative of the ascending branches of the hysteresis loops at four temperatures. Radial distance corresponds to the field value in T. The central area ($B < 40$ mT) was omitted for clarity. White dashed lines indicate the crystallographic a-axes. Pointed line and square represent the c-axis and its projection on the basal plane. A hexagonal pattern is apparent in the data between 50 and 34 K with the second inflections aligned between a-axes.

can be best visualized using the first derivative of the ascending branches (fig. 2.8¹). As above, the second inflection is not visible at room temperature in accordance with Koulialias et al. [2015]. A gap between 300 and 50 K in our study precludes the onset temperature for the second inflection; however, at 50 K, local maxima in the dM/dB curves clearly show a six-fold symmetry dictated by the a-axes.

¹A visualization of all temperatures can be seen in fig. A.5 in the appendix

Not only are the directions consistent with M_s^* maxima, but also their magnitudes, with the strongest inflection coincident with the greatest M_s^* . The peaks in the derivative show a V-shaped pattern aligned with the crystal structure. A likely explanation for the origin of the second inflection is a field induced flipping of the easy axis as suggested by Bin & Pauthenet [1963], who measured the crystalline anisotropy of a spherical Fe_7S_8 crystal. Their calculations of the crystalline anisotropy broke down below 60 K, which they attributed to field induced change in the easy axis direction. The hexagonal pattern disappears around 33 K and then a four-fold symmetry appears below 29 K.

Using the descending branch at positive fields of the hysteresis measured along the dominant axis ($\phi_0 = 75^\circ$) at room temperature as a reference ($M(T_0, B^+, \phi_0)$) we calculated the relative differences to it for all branches measured along other directions (ϕ_n) with:

$$\Delta M(T, B^+, \phi_n) = \left[M(T, B^+, \phi_n) / M(T_0, B^+, \phi_0) \right] - 1$$

in percent (fig. 2.9). Blue colors show regions where the magnetization of the hysteresis branch when measured along ϕ_n is smaller than ϕ_0 for a given field, while red colors show higher moments ($M(T, B^+, \phi_n) > M(T_0, B^+, \phi_0)$). In other words, blue colors indicate harder than average magnetization energies and red, lower. Similar to the derivatives, the relative differences show a hexagonal pattern at temperatures above the Besnus transition. They also show that the moments measured along the magnetic hard axis (160°) is larger than when measured along the easy axis at fields > 0.6 T. This is even more apparent at temperatures (from 50 K to T_{Bes}) and coincides with the second inflections as seen in the derivatives. At $T < 34$ K the hexagonal pattern starts to disappear. At 20 K, the six-fold symmetry has completely disappeared and is replaced by four maxima.

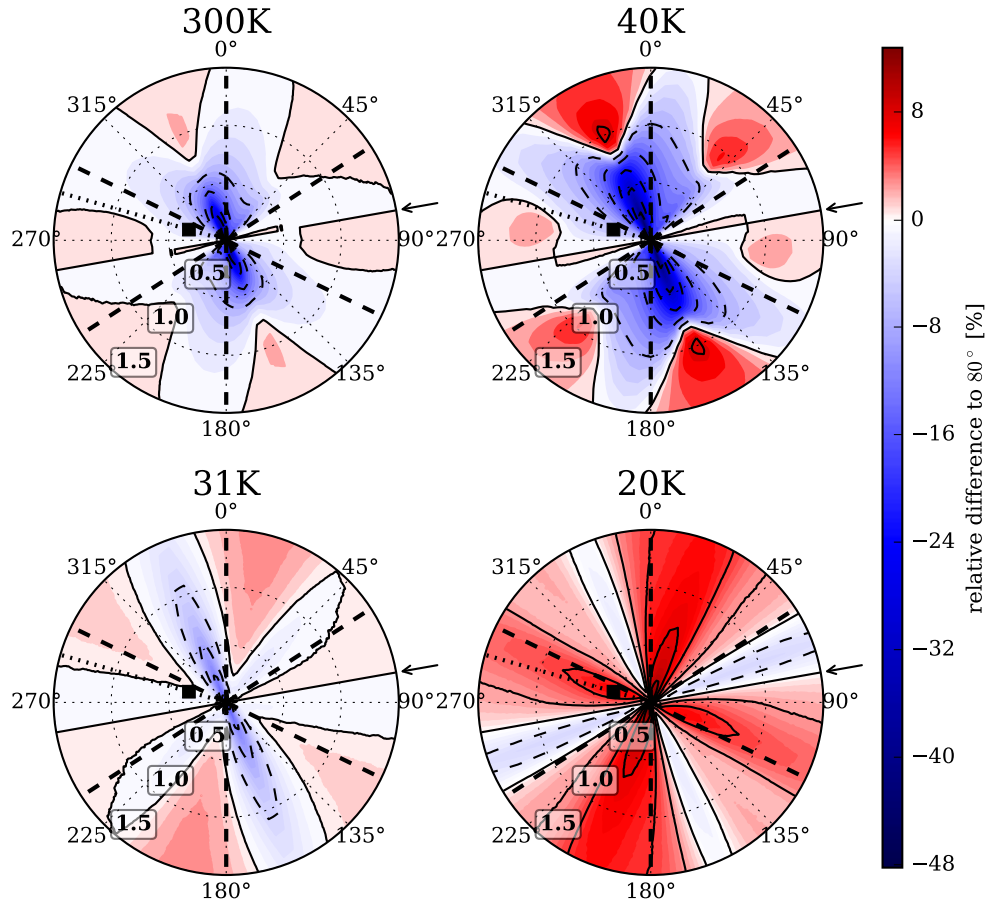


Figure 2.9.: Relative difference of the positive down field branch of each measurement direction with respect to the easy direction at room temperature ($\phi_0=75^\circ$) for selected temperatures. Arrow points along ϕ_0 . Red colors show a positive, blue colors show negative lower magnetic moments. Radial distances correspond to the magnetic field in T.

2.3. Discussion and Conclusions

Repetitive cycling of monoclinic pyrrhotite from 300 K to subsequently lower temperatures until going below the Besnus transition confirms the work of Dekkers et al. [1989] that the amount of magnetization lost is grain size dependent. Pseudo-single domain-rich pyrrhotite loses only $\approx 10\%$ of a room temperature SIRM at 150 K while multidomain-rich pyrrhotite loses $\approx 28\%$ at 150 K. The relative amount of magnetization lost is much less than like grain sizes of magnetite

[Dunlop, 2003]. Dunlop [2003] and Halgedahl [1998] showed that thermoremanent magnetizations generally demagnetizes less than SIRM upon low temperature cycling. If also true for single to pseudo-single domain pyrrhotite, then meteorites that thermally equilibrated in space after acquiring a thermal remanence likely retain most of their original magnetization; paleointensity measurements on them would only slightly underestimate their true intensity. With more temperature cycling experiments, it may be possible to develop a space thermometer to estimate the coldest temperature a meteorite experienced.

From at least 50 K to the Besnus transition, two end-members types of hysteresis loops exist: (1) those resembling magnetic easy axes that quickly saturate by 25 mT and lie parallel to crystallographic a-axes and (2) those that show a double inflection with a maximum change in inflection occurring around 750 mT in-between crystallographic a-axes. These latter curves more closely resemble magnetic hard axes. Although the pattern of hard and easy axis directions mimics six fold symmetry, magnetic energy calculations show one of the axes is relatively easier (lower energy) and one harder (higher energy) than the others (fig. 2.7). The pattern breaks down at T_{Bes} , suggesting independency of the two, just like the isotropic point in magnetite when the two crystalline anisotropy constants change sign is independent of, and ca. 10° higher in temperature than the Verwey transition. Indeed the analogy is intriguing except that in pyrrhotite the "apparent isotropic" point would be temperature and field dependent with the added complication that these dependencies vary with the relative orientation between the crystallographic and applied field directions.

The Besnus transition is characterized by an increase in M_{rs} , B_c and B_{cr} in the 34 to 28 K range, with the most rapid change in M_{rs} or coercivity occurring at 30 K, similar to previous findings [Dekkers et al., 1989, Fillion & Rochette, 1988, Kind et al., 2013, Koulialias et al., 2015, Rochette et al., 1990]. M_s^* remains virtually constant through T_{Bes} from 40 to 20 K.

While a magneto-physical description through T_{Bes} seems clear, the mechanism causing T_{Bes} does not. Likely the most important observation lies in fig. 2.9 where

a clear change from six-fold to four-fold anisotropy occurs. This is further confirmed by the derivative of the loops (fig. 2.8). The most likely cause for change in magnetic symmetry originates in a lowering of the crystallographic symmetry from hexagonal to monoclinic or triclinic. This is consistent with neutron diffraction and magnetic torque measurements that led [Wolfers et al., 2011] to also suggest T_{Bes} arises from a change in crystallography from pseudo hexagonal (slightly monoclinic) to triclinic. We observe one axis of easy magnetization in the magnetizing energy above and two easy directions below T_{Bes} , which is compatible with their findings.

An opposing view of the cause of T_{Bes} interprets the second inflection in the hysteresis loops as evidence for a two phase system [Koulialias et al., 2015]. Koulialias et al. [2015] suggested that interactions between the $5C^*$ and $4C$ magnetic sublattices cause the transition. Our new findings clearly demonstrate a directional dependency of the inflection and its link to the crystallographic a -axes, which argue the phenomenon is related to the crystal lattice. These patterns disappear at the Besnus transition and could be interpreted as field induced switching of easy axis as proposed by Bin & Pauthenet [1963]. We therefore conclude that T_{Bes} owes its origin to changes in crystallographic symmetry and anisotropy rather than interacting superstructures.

Acknowledgments

Parts of this work was performed as a Visiting Fellow at the Institute for Rock Magnetism (IRM) and the Characterization Facility, University of Minnesota. I thank Nicholas Seaton and Joshua Feinberg for their help in obtaining EBSD and EDS data. The IRM is a US National Multi-user Facility supported through the Instrumentation and Facilities program of the National Science Foundation, Earth Sciences Division, and by funding from the University of Minnesota.

Appendix

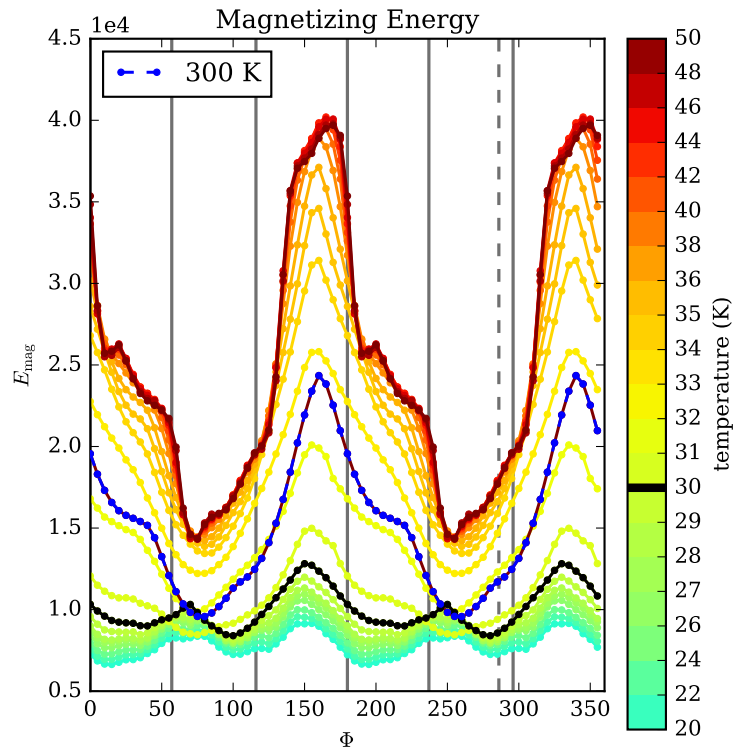


Figure 2.10.: Unnormalized magnetizing energy calculated by integrating over all moments of the descending branch at positive fields. Lines show the crystallographic a-axes with respect to the a_1 -axis at 0° . The dashed line shows the projection of the crystallographic c-axis on the basal plane. Room temperature values in blue.

3. Magnetic Properties of $\text{Fe}_{(100-x)}\text{Ni}_x$ with x from 2 - 20

3.1. Introduction

Meteorites generally form under different conditions and through other processes than terrestrial rocks found at the surface of the Earth. Chondrites, the most abundant type of meteorites (> 80%), are formed by high-temperature processes such as condensation and evaporation in the solar nebular [Krot et al., 2007]. Other meteorite classes are fragments of asteroids and planetesimals that were ejected by meteorite impacts [Stacey, 1976, Weiss et al., 2010]. They represent the only material to be found on earth, which has been exposed and potentially recorded magnetic fields in the early solar system.

While the magnetic remanence in terrestrial rocks is mostly carried by iron oxides, iron oxides rarely exist in extraterrestrial materials [Dunlop & Özdemir, 1997]. The dominant magnetic carriers in meteorites, lunar rocks and lunar soil are iron-nickel alloys [Nagata, 1979b, Rochette, 2003, Rochette et al., 2008, 2009]. Iron meteorites are almost completely composed of iron-nickel alloys with an average Ni content of 5 - 12 wt.% [Albertsen et al., 1983]. Chondrites are predominantly stony and contain grains of metal with similar compositions to iron meteorites [Rochette, 2003, Rochette et al., 2008, Stacey, 1976]. The metal content in stony achondrites is typically nickel poor (<6 at.%) and varies according to their geochemical class (8-20 wt.%) [Rochette et al., 2009].

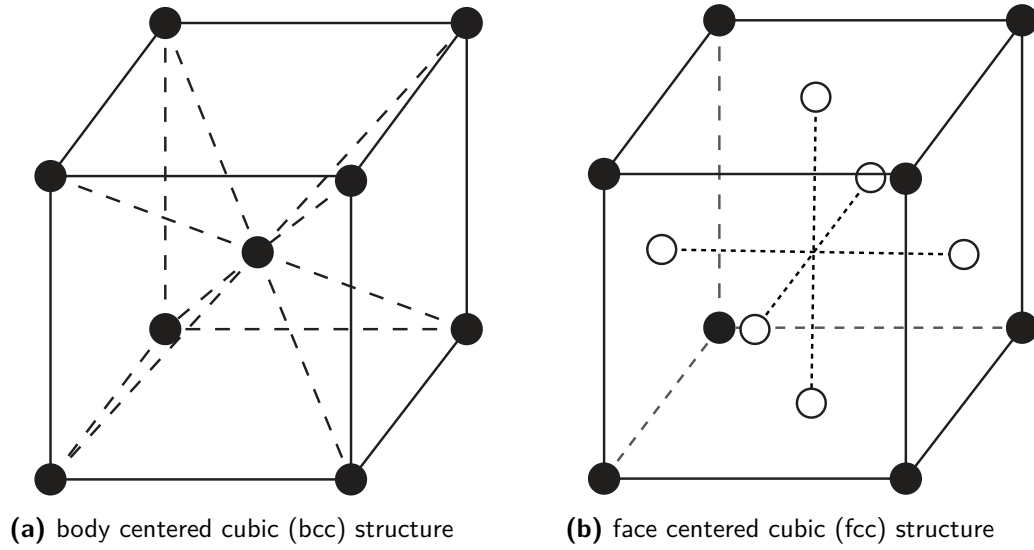


Figure 3.1.: Schematic of the different crystal structures for kamacite (bcc) and taenite (fcc). Lines are guides for the eye.

Some chondrites, with their typical spherical chondrules carry Fe-Ni as tiny inclusions in olivine crystals (dusty olivines) [Fu et al., 2014, Lappe et al., 2011, Van de Moortèle et al., 2007]. These inclusions may not be of primary origin but rather shock induced subsolidus formations from iron-rich olivine [Van de Moortèle et al., 2007]. Similar inclusions have also been reported in other types of meteorites [e.g. Pallasite (stony iron) Tarduno et al., 2012]. The Fe-rich particles often are only several nm in size and can show single domain behavior [Van de Moortèle et al., 2007]. For this reason they have been proposed as suitable carriers for early solar system magnetic fields and have frequently been studied in order to determine the magnetic field strength in the early solar system [e.g. Emmerton et al., 2011, Fu et al., 2014, Uehara & Nakamura, 2006].

The binary iron-nickel system has two equilibrium phases at room temperature. The low nickel (< 6 at.%) α phase with a body centered cubic (bcc, fig. 3.1a) crystal structure is called kamacite [Dunlop & Özdemir, 1997]. Taenite (γ -Fe), the other major phase commonly encountered in meteorites is Ni-rich, crystallizes in a face centered cubic (fcc, fig. 3.1b) structure and is non-magnetic [Dunlop &

Özdemir, 1997]. The Fe,Ni system is an eutectic system, where subsolidus unmixing of α -Fe and γ -Fe happens at temperatures above 349°C [Swartzendruber et al., 1991]. Therefore, certain compositions ($> 6\%$ Ni) unmix from a single phase into two phases below their Curie temperature (T_C , fig. 3.2).

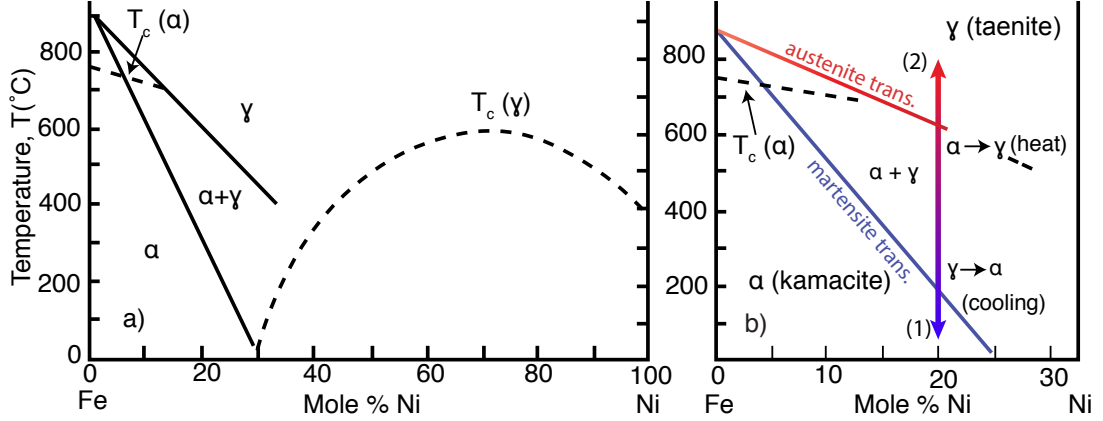


Figure 3.2.: Simplified phase diagram for the iron-nickel system. a) for the complete compositional range for nickel b) enlarged (0-30%) shows the transformations from $\alpha \rightarrow \gamma$ and $\gamma \rightarrow \alpha$. After Dunlop & Özdemir [1997]

Assuming a sample with a Ni content of 20 at.% is heated (arrow in fig. 3.2b) from room temperature (1 in fig. 3.2b) to elevated temperatures (2), it would continuously transform from the α -Fe into the non-magnetic γ -Fe phase [Dunlop & Özdemir, 1997]. This so called austenite ($\alpha \rightarrow \gamma$) transitions is completed at around 600°C for $\text{Fe}_{80}\text{Ni}_{20}$ [Wasilewski, 1981a]. Cooling this sample to room temperature transforms the γ -Fe phase back into the α -Fe phase at the martensite transition (blue line in fig. 3.2b). Since the austenite ($\alpha \rightarrow \gamma$) transition occurs at a higher temperature than the martensite ($\gamma \rightarrow \alpha$) transition, a wide thermal hysteresis is visible in thermomagnetic measurements [Butler, 1972]. It also leads to intergrowths of phases with Ni enriched and depleted parts, compared to the bulk Ni content [Nagata, 1979b].

These transformation complicate the interpretation of magnetic signals in meteorites [Wasilewski, 1974a,b]. The natural remanent magnetization (NRM) is often assumed to be of thermal origin. In this case a mineral is cooled through its

Curie temperature in a magnetic field and records that field. In the case of Fe,Ni alloys the assumption that the magnetization of a meteorite is a thermomagnetic remanence (TRM) may not hold for some Fe,Ni phases [Wasilewski, 1974a, Weiss et al., 2010]. Since atomic rearrangements of the crystal structure happen at temperatures below the Curie point the remanence that was acquired in a magnetic field is of chemical origin. It is typically referred to as a thermo chemical or martensitic remanent magnetization rather than a TRM [Stacey, 1976]. Even though the minerals of the iron nickel system play an important role in meteorite magnetism and industry, their magnetic properties, their dependence on composition and grain size and thermomagnetic behavior are poorly known.

Rock magnetism is concerned with the magnetic domain state of a sample. Domain configurations for a given mineral change depending on the size of the particle. Very small particles (< 30 nm for magnetite) are in the so called superparamagnetic (SP) state [Muxworthy & Williams, 2015]. These particles are not magnetically stable (fig. 3.3) because the thermal energy at room temperature can cause the spontaneous reversal of the particle's magnetization [Dunlop & Özdemir, 1997]. Larger grains (25-60 nm for magnetite) are stable to thermal fluctuations due to their higher energy barrier so that spontaneous reversals are unlikely [Butler & Banerjee, 1975]. These particles are composed of only one uniformly magnetized domain (single domain or SD) and are characterized by a high remanence and coercivity [Newell & Merrill, 1999]. As particles get even larger, it is energetically favorable to diverge somewhat from a strictly parallel spin arrangement [Dunlop & Özdemir, 1997]. Grains in this state behave in a similar way as single domain grains; they are referred to as pseudo-single domain or PSD [Shcherbakova et al., 2000]. Eventually, the particle is divided into complex patterns of two or more magnetic regions (domains) (>20 μm for magnetite). They are divided by domain walls and therefore these particles are called multidomain (MD). The presence of these structures lower the remanent magnetization and coercivities of a particle [Fabian, 2003].

Néel [1955] showed that single domain particles are especially important for pa-

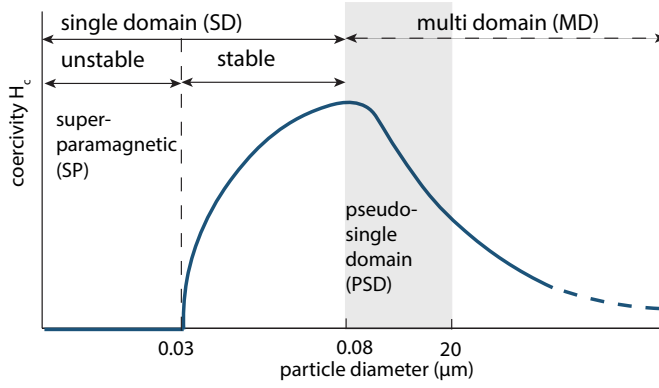


Figure 3.3: Illustration of the changes in coercivity with grain size and domain state for magnetite. After Dunlop [1981], Moskowitz [1991]

leomagnetism because of the stability of their remanent magnetization against thermal fluctuations. These fluctuations can cause a spontaneous reorientation of the magnetic vector in the particle. The relaxation time (τ) is the average time between these magnetization reversals [Mørup et al., 2011].

$$\tau = f_0^{-1} \exp\left(\frac{vH_cM_s}{k_B T}\right) \quad (3.1)$$

where f_0 is the frequency factor ($\approx 10^{-9}/s$), v is the grain volume, H_c is the particle's coercive force, M_s is the saturation magnetization, k_B is the Boltzmann constant, and T is the absolute temperature [Butler, 1972]. Section 3.1 explains why the magnetization of very small particles (SP) is unstable. The relaxation time of a superparamagnetic particle is short enough for the magnetization to flip within the timeframe of a measurement. Thus no remanence can be retained. On the other hand, large multidomain particles have very low H_c values and can lose some of their magnetic moment due to thermal relaxation [Muxworthy & Williams, 2006, Williams & Muxworthy, 2006]. This is of particular importance when dealing with magnetizations that are acquired during the formation of the early solar system and have to be stable for > 4 billion years.

Pullaiah et al. [1975] calculated the relaxation times for magnetite and hematite single domain particles and showed that their magnetic moments can be stable for billions of years. Similar calculations were made for pure iron [Garrick-Bethell

& Weiss, 2010]. The super paramagnetic (SP) to SD threshold for spherical iron particles was calculated using Néel's relaxation equation by Butler & Banerjee [1975]. They showed that spherical iron particles may not possess a stable single domain state and that only a narrow range of very elongate grains between 15 nm and 60 nm will be stable. More recently Muxworthy & Williams [2015] reexamined their findings using micromagnetic modeling and found stable single domain for particles < 25 nm. Snoeck et al. [2008] confirmed that the spin structure of 30 nm particles were in a vortex state and thus in the pseudo single domain (PSD) realm, which is larger than single domain. Besides pure Fe, the single domain threshold for Fe–Ni alloys has yet to be determined and experimentally verified.

Domain state can be estimated by measuring hysteresis loops and backfield curves. In a typical hysteresis measurement, a sample is exposed to a magnetic field. The magnetic moment $M(B)$ is measured while the field is swept from a maximum positive (e.g. 1T) to a negative minimum and back [Dunlop & Özdemir, 1997]. The magnetic moment of the sample is normalized by its mass and plotted against the magnetic field to produce the typical hysteresis loop. If the upper ($+B \rightarrow -B$) and the lower branch ($-B \rightarrow +B$) coincide, the hysteresis is "closed" and the sample does not carry a remanence. Otherwise, the hysteresis is called "open". From this measurement several parameters can be used to characterize the sample. The saturation magnetization M_s is the maximum magnetic moment achievable in a magnetic field ($M(B \rightarrow \infty)$) and a material constant [Dunlop & Özdemir, 1997]. The saturation remanence M_{rs} is the magnetic moment that is retained by the sample when the field is switched off, after reaching saturation ($B = 0$). The field at which the magnetization in a field is zero is called coercivity (B_c).

In a backfield curve a strong positive field is used to saturate the sample. This saturation remanence (M_{rs}) is successively demagnetized by increasing negative fields and the remanence is measured without an applied field after each step. The field that had to be applied for the remanence to be fully demagnetized is

called the remanence coercivity B_{cr} Dunlop & Özdemir [1997]. An important distinction between the coercivity B_c determined from a hysteresis loop and the remanence coercivity B_{cr} calculated from a backfield curve is that B_c is measured in a magnetic field, while B_{cr} is not. Several processes such as domain wall displacements and magnetic viscosity can cause $B_c \neq B_{cr}$. Therefore these parameters can be used to characterize the mineralogy of a sample.

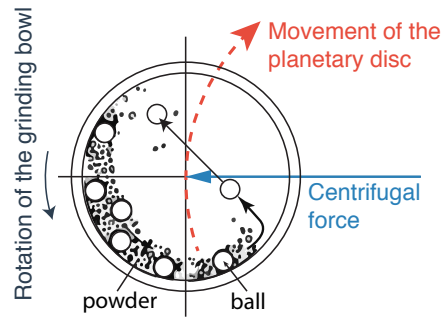
The ratio of saturation remanent magnetization to saturation magnetization (M_{rs}/M_s) as well as remanent coercivity and coercivity ratio (B_{cr}/B_c) can be used to determine whether a sample is single domain [Day et al., 1977, Dunlop, 2002a]. These ratios are well known for most of the terrestrial magnetic materials [e.g. Dunlop, 2002b, Peters & Dekkers, 2003], but less well known for Fe,Ni alloys. A sample containing a randomly oriented assemblage of single domain particles with uniaxial anisotropy has a remanence ratio of $M_{rs}/M_s = 0.5$ [Dunlop & Özdemir, 1997]. In a compilation of several dozen lunar samples, Wasilewski [1981a] showed that the coercivity ratio of lunar samples rarely is below $B_{cr}/B_c = 3$ and M_{rs}/M_s typically does not exceed 0.1.

3.2. Mechanical alloying

Chemical synthesis of fine particles of these minerals is difficult and traditional alloying techniques have several shortcomings. Slow diffusion rates often result in inhomogeneous samples [Crangle & Hallam, 1963]. Material is melted at high temperatures making it vulnerable to oxidation and needs to be quenched in order to inhibit the unmixing of the phases. Finally the material has to be reduced to grain sizes of a few nanometers. After a thorough literature review, we decided to generate nano particles via mechanical alloying.

Mechanical alloying is a technique that works by repeated cold welding, fracturing and re-welding of elementary powders to create very fine particles (fig. 3.4). It is commonly used in industry. In contrast to conventional techniques, it can produce non-equilibrium phases such as α -Fe,Ni alloys that have not unmixed

Figure 3.4: Workings of a planetary ball mill. Bowl and planetary disk (not shown) rotate in opposite directions. The centrifugal force causes the grinding medium (balls) to accelerate (≤ 95 G) and powder caught between balls to be fractured / cold welded. After Suryanarayana [2001]



[Suryanarayana, 2001].

The planetary ball mill is commonly used for MA. It consists of a planetary disk where the milling bowls can be attached. Disk (fig. 3.5a) and bowls (fig. 3.5b) rotate in opposite directions creating centrifugal forces up to ≈ 100 G that accelerate the grinding balls (fig. 3.5c). Whenever two balls collide, a small amount of powder is trapped in between them and is fractured and cold welded [Suryanarayana, 2001]. The repeated shocks cause a grain size reduction of the particles and the transformation of the different starting powders into a single crystal structure. This method can produce homogeneous alloys with crystallites of a few nm [Suryanarayana, 2001].

The results of the milling process rely on many factors [Moys, 2015]. Higher rotation speeds generate stronger centrifugal forces and the milling medium is accelerated to higher velocities. Friction and shock energies depend on the ratio of planetary disk rotation speed (Ω) compared to that of the bowls (ω) [Gaffet et al., 2004]. While large ω/Ω results in increased frictional energy a reduced ratio tends to increase shock energies and reduces the particle size faster. The size of the milling balls as well as the powder to ball ratio will also influence the resulting sample [Koch, 1997, Suryanarayana, 2001].

When the powder is suspended in liquid (e.g. water or ethanol) during milling the process is referred to as wet milling. Water is not a viable choice when the products are prone to oxidation. A more suitable choice are alkanes such as Hexane ($\text{CH}_3(\text{CH}_2)_4\text{CH}_3$) or Heptane ($\text{CH}_3(\text{CH}_2)_5\text{CH}_3$). They are constituents

of gasoline and highly flammable. Sometimes surfactants are added (surfactant assisted milling) to reduce interactions between particles [Akdogan et al., 2009]. These surfactants create a layer of material between individual particles and thus increase their mean distance. The temperature inside the bowl during milling can rise to $> 100^{\circ}\text{C}$ within a few minutes, especially at higher rotation speeds. Since the milling bowls can only withstand temperatures of up to 130°C , temperature and pressure have to be constantly monitored.

Mechanical alloying has been used to synthesize a variety of magnetic phases. Magnetite was produced by milling of hematite with metallic iron in stoichiometric proportions [Petrovský et al., 2000]. Mechanically alloyed iron-nickel alloys, typically with high Ni concentrations, have been frequently studied in the context of material science because of their technological relevance. Most studies, however are mainly concerned with structural properties and their evolution with milling time [Baldokhin et al., 1999, Djekoun et al., 2004, Kaloshkin et al., 2001, Zhu & Huang, 2003]. Studies that are seeking to determine the magnetic properties of mechanically alloyed Fe-Ni, typically are less concerned with grain size from a rock magnetic point of view [Gaffet et al., 2004, Hamzaoui et al., 2003, Li et al., 1997]. To my knowledge this is the first study to systematically investigate differences in magnetic properties with Ni concentration and grain size.

3.3. Synthesis

I used a Fritsch Pulverisette Premium (P7) planetary ball mill (fig. 3.5a) with a maximum rotation speed of $\Omega = 1100$ rpm and place for two bowls for alloying of the powders. Elementary powders of Fe (Sigma Aldrich $\geq 99.5\%$) and Ni (Sigma Aldrich $\geq 99.7\%$) were used as received. Several different powder mixtures – with the correct atomic weight ratio – were produced with Ni concentrations ranging from 2-20%. They were filled into a 80 mL bowl together with 100 g yttrium stabilized zirconium oxide ceramic beads in two different sizes (3 and 0.5 mm) as milling medium. Even though their density is lower than other milling media (e.g.



(a) Fritsch Pulverisette 7 Premium high energy planetary ball mill



(b) 80 ml bowl for the mill with pressure and temperature sensor



(c) Grinding medium consists of 3 mm Yttrium stabilized Zirconia ceramic beads



(d) Glovebox with vacuum port, where all sample handling was done under Ar atmosphere

Figure 3.5.: Milling setup: a) mill b) bowls c) 3 mm grinding medium d) glovebox

steel) they have the distinct advantage of being extremely abrasion resistant, and most importantly, do not contain iron, which could distort the iron to nickel ratio and influence the purity of the sample[Koch, 1997].

Because iron is prone to oxidation, all sample handling steps are done under Argon atmosphere. For this we used a three port glovebox with a vacuum port. The glovebox (fig. 3.5d) was flushed with Argon and the oxygen level was constantly monitored using an oxygen gas sensor. A slight overpressure was maintained in the glove box in order to keep oxygen levels at a minimum, which never exceeded 2%.

3.3.1. Milling Protocol

The rotation speed of the disc can be set and the transmission is fixed to 1:2 with the bowls rotating at twice the rate of the planetary disk ($\Omega = 0.5 \times \omega$). Thus the milling process described here is mainly in friction mode [Gaffet et al., 2004]. In order to produce different grain sizes, milling was done for different times and at two different speeds ($\Omega = 400$ rpm and $\Omega = 1100$ rpm).

One of the bowls used during the mechanical alloying process is equipped with temperature and pressure sensors. Due to the increased energy when milling at 1100 rpm the sample bowl quickly heats up. The sensors give the possibility to interrupt the run so that temperatures and pressures do not reach preset limits ($T_{\max} = 70^{\circ}\text{C}$, $P_{\max} = 5$ bar). Since the temperatures were always kept within these predefined limits, high and low energy milling regimes are easier to compare. At 400 rpm the T,P limits were barely reached during continuous operation, while at 1100 rpm, 2 min milling was followed by 15 min cooling time, prolonging a 1 hr milling run to 8 1/2 hours.

Several protocols including wet and surfactant assisted milling techniques were tested on different compositions (table 3.1). Only few of them gave the desired results. Protocols with small grinding balls generally did not produce properly alloyed or homogeneous powders, likely due the small mass of the balls. A thick

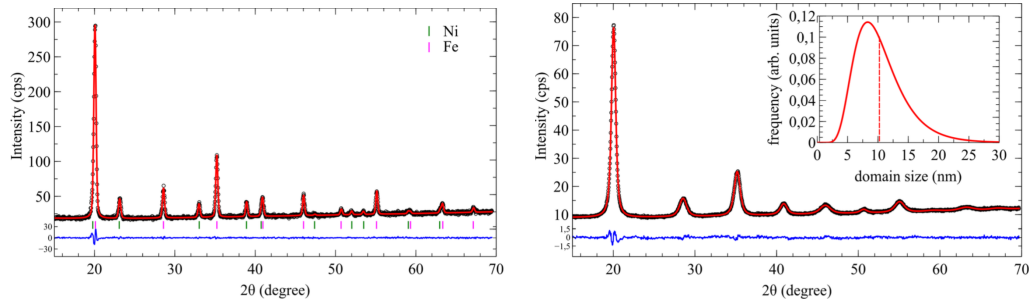
rpm	Liquid	Quantity	Surfactant	Quantity	Ball size
400	-	-	-	-	0.5 mm
400*	-	-	-	-	3mm
400	-	-	Oleic Acid	10 wt. %	3mm
400	Heptane	10 wt. %	Oleic Acid	10 wt. %	3mm
1100	-	-	-	-	0.5mm
1100*	-	-	-	-	3mm
1100	Heptane	10 wt. %	Oleic Acid	10 wt. %	0.5mm
1100	Heptane	10 wt. %	Oleic Acid	10 wt. %	3mm
1100	Si-Oil	10 wt. %	-	-	3mm
1100	-	-	Oleic Acid	10 wt. %	3mm

Table 3.1.: Overview of the tested milling protocols of this study. Not all protocols proved to produce the desired alloys or sizes. * denotes protocols that were adopted in the study.

shell of material covered the balls in wet techniques, especially for 0.5 mm and made extracting the sample nearly impossible. In addition, the mass of the (Fe,Ni) powder was difficult to determine because of the added mass of surfactant and milling liquid. Therefore, only dry milling techniques with 3 mm beads were used.

3.4. Samples

The milling procedure was monitored by opening the bowls and subsampling the milled powder for the $\text{Fe}_{80}\text{Ni}_{20}$ composition. To reduce the risk of oxidizing the material, all handling of powders was done inside the glovebox. Subsamples were taken after milling times of 1, 2, 4, 6, 10, 16, 30, 60, 120, 240, 480, 960, 1440, and 2160 min. During the high energy milling protocol (1100 rpm) the sample solidified and milling times longer than 240 minutes were not possible. After the optimal milling time was determined, as described in the next section, several other compositions ($\text{Fe}_{98}\text{Ni}_2$, $\text{Fe}_{96}\text{Ni}_4$, $\text{Fe}_{94}\text{Ni}_6$, $\text{Fe}_{92}\text{Ni}_8$ and $\text{Fe}_{88}\text{Ni}_{12}$) were milled for 2160 min at 400 rpm.



(a) $\text{Fe}_{80}\text{Ni}_{20}$ starting powder. Green lines indicate Ni (fcc) peaks, pink lines indicate Fe (bcc) peaks

(b) X-ray diffraction of $\text{Fe}_{80}\text{Ni}_{20}$ after 2160 min of milling. The inset shows the log-normal domain size distribution with its arithmetic mean size.

Figure 3.6.: X-ray diffraction and of starting $\text{Fe}_{80}\text{Ni}_{20}$ mixture and 2160 min milled powders (400 rpm). Observed intensities (black circles), calculated pattern (red), and the difference curve (blue)

3.4.1. Sample Preparation

For each sample of each milling time, energy and composition, three specimen were prepared. About 50 mg of powder was filled into a gel cap with the rest of the volume filled with fine quartz sand. A second set of samples was prepared by diluting about 0.5 g of (Fe,Ni) powder with 9.5 g quartz sand in an attempt to minimize interactions between particles. For each diluted sample we prepared three gel cap samples in the same fashion as described earlier.

3.5. X-ray diffraction

X-ray diffraction (XRD) measurements were performed with a STOE Stadi P diffractometer in Debye-Scherrer geometry. Data were recorded in the range from 10° to 70° 2θ and a counting time of 360 s per step, using $\text{Mo-}\alpha_1$ ($\lambda = 0.7093\text{\AA}$) radiation and a curved position-sensitive detector with a step size of 0.15° 2θ . Glass capillaries of 100 μm diameter and 10 μm wall thickness were used as sample holders.

The XRD patterns were analyzed using the Rietveld method [Rietveld, 1969] implemented in the program MAUD [Lutterotti et al., 1999]. The instrumental resolution was determined by measuring a NIST SRM 660b (LaB_6) standard under the same conditions used for the ball-milled samples. Size and strain broadening was fitted using the anisotropic size/strain model after Popa & Lungu [2013]. All X-ray diffraction work was done with the help of Dr. Bernd Maier, Ludwig-Maximilians Universität München.

Figure 3.6a shows the XRD pattern of the 80% iron, 20% nickel powder mixture before ball milling at 400 rpm. Reflections from both phases, i.e. Fe (bcc) and Ni (fcc), are visible. Both phases show no resolvable sample broadening, i.e. the mean domain size for both phases is above 100 nm and no detectable strain broadening. Rietveld refinement of the unmilled powder shows a Ni concentration of $18.7 \pm 2\%$.

For both milled and unmilled powders, no other phases (e.g. iron oxides) can be found. Milling times of > 120 minutes show a significant broadening of the peaks due to grain size reduction and increased microstrain. After 960 minutes of milling the reflections from the Ni (fcc) phase disappeared completely, i.e. nickel has been completely incorporated into the bcc structure (fig. 3.6b). The mean crystallite size ($t = 960$ min, 400 rpm) has been reduced from 75 ± 4 nm to 10.9 ± 2 nm while the microstrain has increased to $1.18 \pm 2\%$. Further milling has less impact on the crystallite size and microstrain. Particles with a mean size of 10.24 ± 3 nm and microstrain of $1.38 \pm 2\%$ are observed (see inset of fig. 3.6b and fig. 3.7) after 2160 minutes. Similar grain sizes were reported in previous studies on various Fe,Ni compositions [e.g. Baldokhin et al., 1999, Gaffet et al., 2004, Hamzaoui et al., 2003, Otmani et al., 2009].

3.6. Magnetic Measurements

Rock magnetic measurements consisting of hysteresis loops, backfield curves, isothermal remanent acquisition (IRM) curves and FORC measurements were

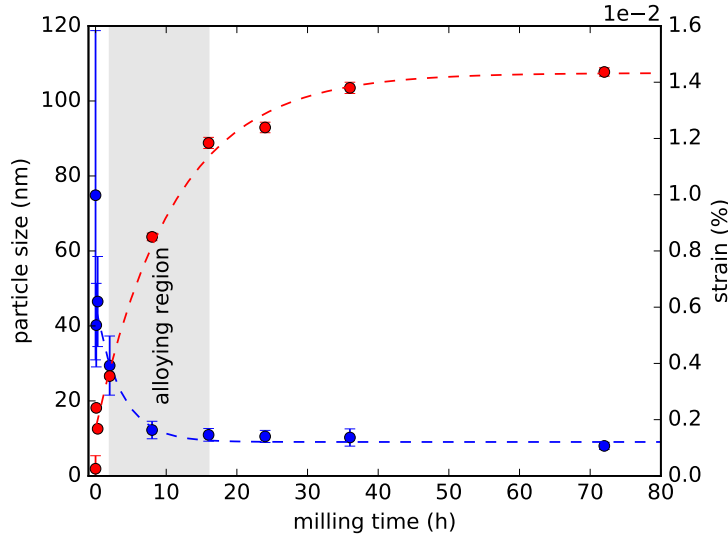


Figure 3.7: Crystallite size and strain calculated by Rietveld method for $\text{Fe}_{80}\text{Ni}_{20}$. Dashed lines show a least squares fit of an exponential function for size (blue) and strain (red). Particle size decreases rapidly within the first few hours of milling. Shaded area marks the alloying region.

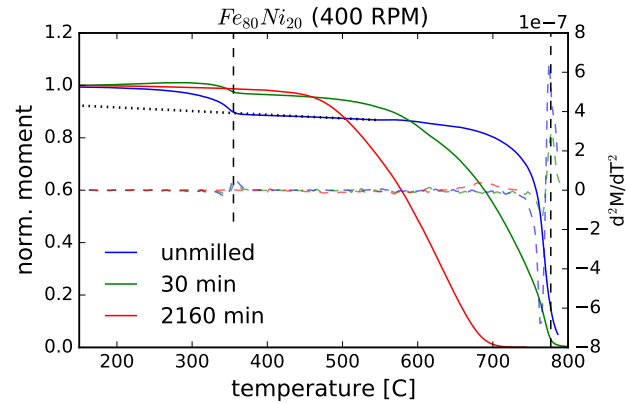
done with a *Lake Shore* PMC MicroMag 3900 Series vibrating sample magnetometer (VSM). High temperature measurements were done using a Ar-flow furnace in the VSM. Further thermomagnetic measurements were done on a Petersen instruments variable fields translation balance (VFTB) in air.

3.6.1. Changes of magnetic properties during alloying

In order to verify the alloying progress, Curie temperatures were measured in Argon atmosphere of several $\text{Fe}_{80}\text{Ni}_{20}$ samples at different milling times. The unmilled sample gave 2 Curie temperatures, one for iron (770°C) and one for nickel (358°C). At the Curie point of nickel the magnetic moment of the powder is reduced by 9.5%. At temperatures above $T_c(\text{Ni})$ the magnetization shows a shallow linear decrease up to temperatures close to the Curie point of Fe, which is marked by a sharp drop in magnetization.

Calculating the concentration of nickel from the loss in moment after the Curie temperature gives a value ($\approx \text{Fe}_{70}\text{Ni}_{30}$) higher as determined by XRD. Using the linear decrease in magnetization at $450\text{--}550^\circ\text{C}$ and assuming a similarly linear decrease in the range $20\text{--}450^\circ\text{C}$, a linear regression can be used to determine the

Figure 3.8: Moment versus temperature heating cycles for different milling times for $\text{Fe}_{80}\text{Ni}_{20}$. Blue shows unmilled mixture, green milled for 30 minutes. Red shows fully alloyed powder. Heating was done in Ar. Dashed vertical lines show Curie points for iron (770°C) and nickel (358°C). Dotted line shows linear regression of $M(450\text{--}550^\circ\text{C})$. Dashed line shows d^2M/dT^2



initial magnetic moment of the iron (see dashed black line in fig. 3.8). This yields a Ni concentration of 19.2% in agreement with the value determined by XRD and the initial mixing ratio of the elementary powders.

With increasing milling time (green line fig. 3.8) both Curie temperatures become less pronounced indicating that a portion of the Ni has already been incorporated into the $\alpha\text{-Fe,Ni}$ structure, while XRD shows little to no alloying has happened even at milling times of 60 min. Subtle changes in magnetization are easily visible within magnetic data, while these are not yet visible in XRD. After milling for 2160 min at 400 rpm the Ni has been completely absorbed into the bcc structure (red line in fig. 3.8). Compared to the pure iron, the transition is less sharp with only one Curie temperature at $T_C = 688^\circ\text{C}$ close to the Curie point of iron-nickel alloys of similar composition [Swartzendruber et al., 1991].

3.6.2. Rock Magnetic Measurements

Mass normalized hysteresis loops were corrected for symmetry and the arithmetic mean of the three subsamples was calculated after linear interpolation. Calibration of the absolute moment of the VSM was done once a day using the NIST 772a nickel standard. Figure 3.9c shows hysteresis loops for three different milling times of the $\text{Fe}_{80}\text{Ni}_{20}$ composition at 400 rpm and 1100 rpm. Hysteresis

Table 3.2.: Hysteresis and backfield parameters for all milling time for the $\text{Fe}_{80}\text{Ni}_{20}$ composition. Milling times longer than 240 min not possible at 1100 rpm.

time (min)	M_s (Am^2/kg)		M_{rs} (Am^2/kg)		B_c (mT)		B_{cr} (mT)	
	400 rpm	1100 rpm	400 rpm	1100 rpm	400 rpm	1100 rpm	400 rpm	1100 rpm
1	187.3±5.0	179.3±0.8	2.2±0.1	4.0±0.3	2.8±0.8	3.5±1.0	22.1±0.8	16.6±1.0
2	180.0±2.2	178.7±2.2	2.3±0.1	4.9±0.4	2.9±0.5	3.7±0.5	21.9±0.5	16.2±0.5
4	180.1±1.6	177.6±0.5	2.6±0.0	3.9±0.0	3.1±0.3	3.4±0.5	21.0±0.3	18.1±0.5
6	180.3±1.4	177.8±0.8	2.9±0.1	3.4±0.1	3.3±0.5	2.8±0.3	20.0±0.5	16.0±0.3
10	177.8±0.9	178.2±0.2	3.4±0.3	2.7±0.2	3.5±1.0	2.7±0.7	18.7±1.0	19.7±0.7
16	177.2±0.6	175.2±1.1	4.3±0.1	2.9±0.1	3.8±0.4	3.3±0.7	16.3±0.4	23.6±0.7
30	176.7±2.5	168.3±2.6	5.4±0.0	3.9±0.2	4.1±0.1	4.6±0.7	15.6±0.1	24.7±0.7
60	175.3±0.8	164.5±3.0	5.5±0.1	4.0±0.1	4.5±0.2	4.8±0.6	17.6±0.2	25.7±0.6
120	176.0±0.9	155.5±2.5	4.4±0.2	3.8±0.2	4.5±0.7	4.7±0.4	23.0±0.7	26.6±0.4
240	179.2±0.8	142.3±0.4	2.8±0.2	4.1±0.1	3.5±1.8	5.2±0.1	28.8±1.8	26.7±0.1
480	187.2±1.7		2.4±0.1		3.0±0.3		27.9±0.3	
960	192.5±1.2		2.5±0.1		3.2±0.7		26.6±0.7	
1440	189.3±0.5		2.4±0.0		3.3±0.1		28.5±0.1	
2160	189.6±5.4		2.8±0.0		3.5±2.1		28.3±2.1	

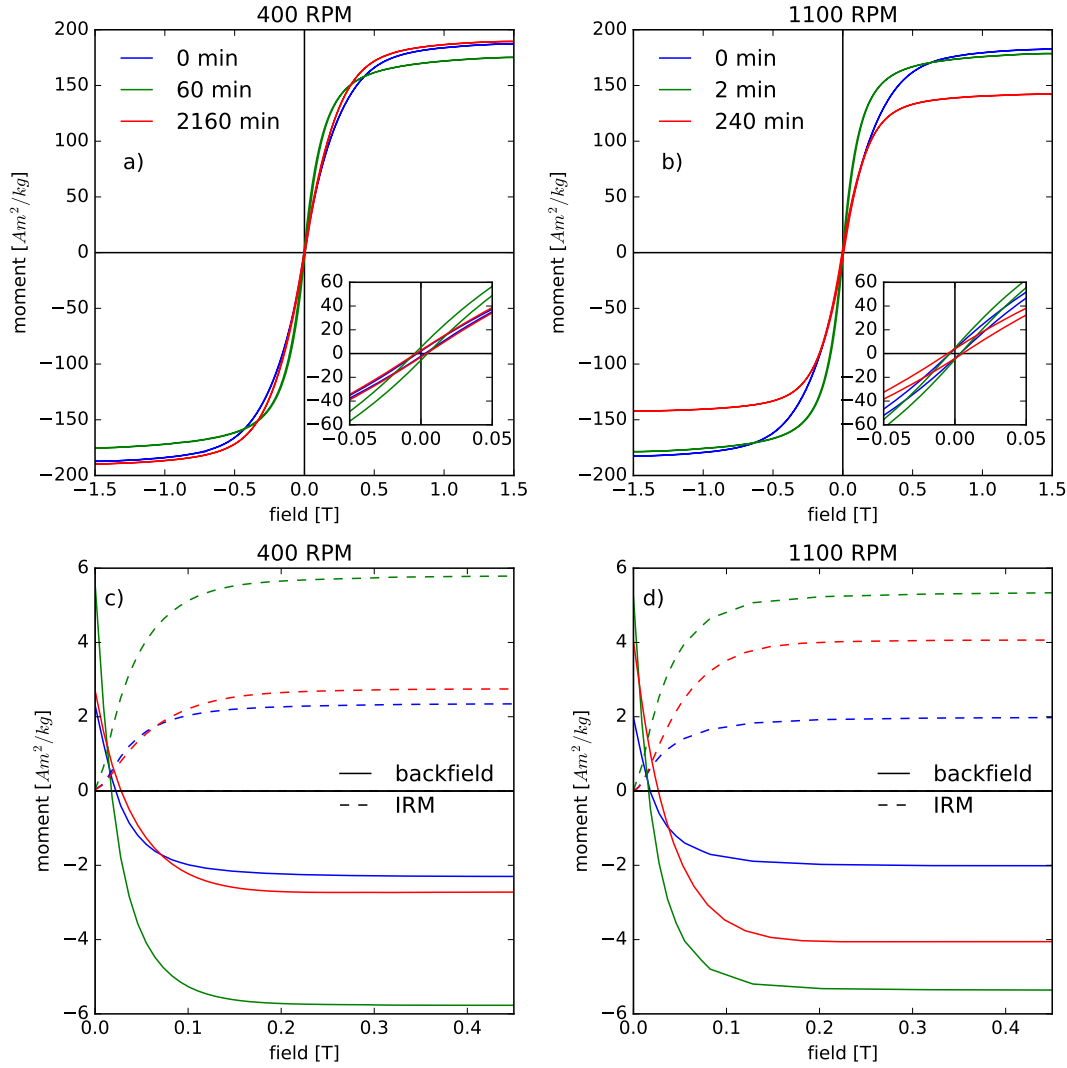


Figure 3.9.: Comparison of room temperature rock magnetic measurements for 400 rpm (left row) and 1100 rpm (right row) milled $\text{Fe}_{80}\text{Ni}_{20}$. **a,b)** show hysteresis loops for unmilled powder (green) and 2 different milling times. Inset shows hysteresis at field range (± 50 mT). **c,d)** shows backfield (solid lines, absolute field) and IRM acquisition (dashed lines). Red curves show the longest milling time for either sample. Inset in a) shows enlarged field region from -50 - 50 mT.

loops of the unmilled powders are almost closed, with low coercivity ($B_c = 2.7$ mT) and saturation remanence ($M_{rs} = 2.2 \text{ Am}^2/\text{kg}$) (table 3.2). The saturation magnetization ($M_s = 182.7 \pm 3 \text{ Am}^2/\text{kg}$) is within error of the calculated value $M_s(\text{Fe}_{80}\text{Ni}_{20}) = 183.8 \text{ Am}^2/\text{kg}$ [Crangle & Goodman, 1971] for a mixture of 80

at.% Fe ($217.7 \text{ Am}^2/\text{kg}$) and 20 at.% Ni ($55.1 \text{ Am}^2/\text{kg}$). IRM acquisition curves (dashed lines in fig. 3.9) show saturation remanence is reached in a field of 350 mT, while slightly lower fields (250 mT) are needed in the backfield measurement. M_{rs} values for both IRM and backfield correspond well to the value obtained from hysteresis measurements.

Domain state can be estimated by the remanence (M_{rs}/M_s) and coercivity ratios (B_{cr}/B_c) [Day et al., 1977, Dunlop, 2002a]. Determined values for the unmilled powders indicate that the sample is in a multidomain state with $B_{cr}/B_c = 8.0$ ($B_{cr} = 22 \text{ mT}$) and $M_{rs}/M_s = 0.01$ consistent with the expected domain state for initial grain sizes of $>100 \text{ nm}$ (table 3.3)[Dunlop, 2002a].

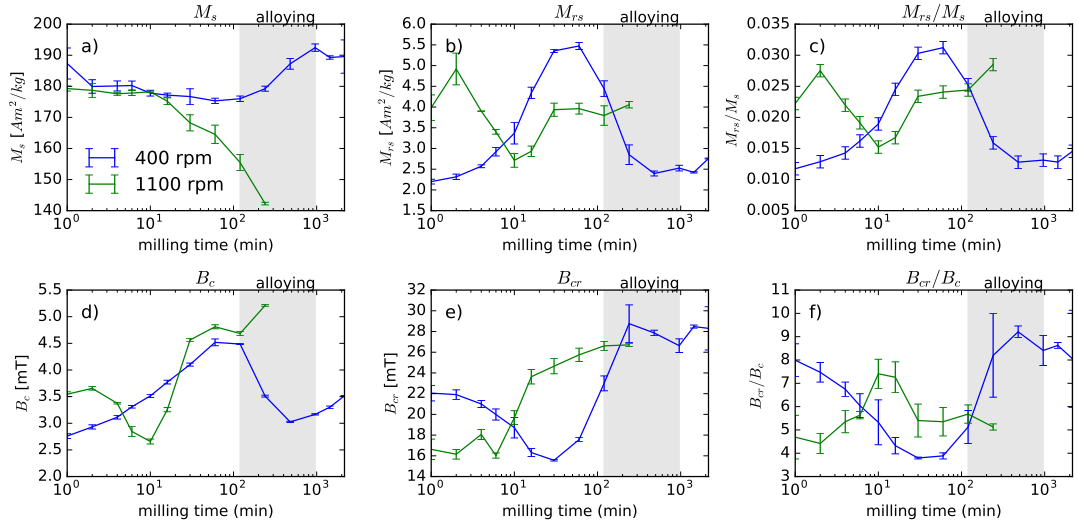


Figure 3.10.: Evolution of the mean rock magnetic properties with milling time, error bars show one standard deviation. The shaded region indicates where alloying starts and ends in the 400 rpm samples as determined by XRD.

With increasing milling time at low energy (400 rpm), M_s decreases slightly to a minimum at 60 minutes ($M_s(60 \text{ min}) = 175.3 \text{ Am}^2/\text{kg}$) and increases during the alloying phase to $M_s(2160 \text{ min}) = 189.6 \text{ Am}^2/\text{kg}$. The saturation remanence peaks ($M_{rs}(60 \text{ min}) = 5.5 \text{ Am}^2/\text{kg}$) then decreases and stabilizes. The increased M_{rs} value causes a maximum of the $M_{rs}/M_s = 0.03$ ratio. The coercivity increases up to 60 min $B_c(60 \text{ min}) = 4.5 \text{ mT}$ and then decreases. Remanence coercivity

shows a minimum at 30 minutes $B_{\text{cr}}(30 \text{ min}) = 15.5 \text{ mT}$, leading to a reduction of remanence ratio from 8 to 4. For milling times longer than 60 min the opposite behavior is visible with M_s and B_{cr} increasing while M_{rs} and B_c are decreasing, even though the grain-size is further reduced.

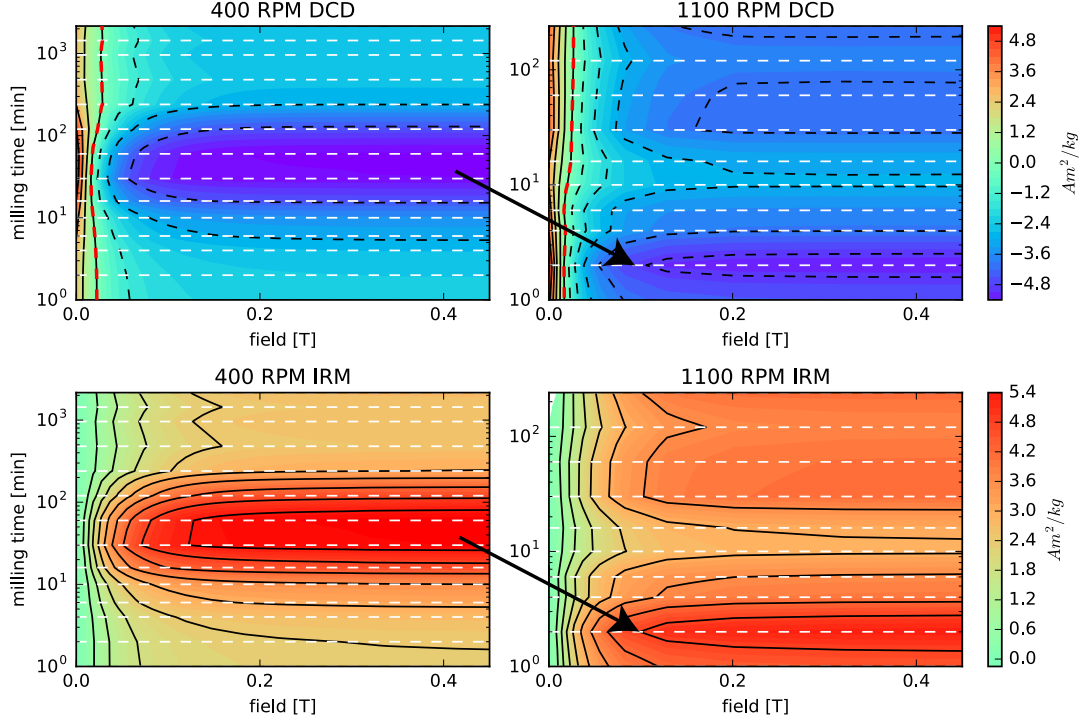


Figure 3.11.: Contour plots for backfield (top) and IRM acquisition (bottom) for 400 rpm (left) and 1100 rpm (right). Dashed red line in the backfield plot shows the value of B_{cr} . Color scales are equal for all plots and show the magnitude of magnetization. Dashed lines represent the actual measurements, the rest is determined by linear interpolation. Dashed contour lines show negative values; solid lines show positive values. A cross section along the 0.5 T value corresponds to $\pm M_{\text{rs}}$ and is within 2% of the value determined from hysteresis measurements (see fig. 3.10).

The highest values for M_{rs}/M_s and B_{cr}/B_c (table 3.3) are found near the start of the alloying region as determined by XRD (shaded region fig. 3.10). At this stage both XRD and thermomagnetic curves show that the sample is comprised of multiple components (i.e. Fe, Ni and inhomogeneous FeNi alloy). Both the increase in remanence ratio as well as the decrease in coercivity ratio indicate a change in grain size towards a more single domain like state for at least one of

the components [Dunlop, 2002a].

Plotting backfield and IRM in a contour plot shows changes in remanence with milling time. Each dashed line in fig. 3.11 corresponds to the mean of three separate samples measured at each milling step. Maximum (IRM) and minimum (backfield) value correspond to the M_{rs} value as determined by hysteresis loops (see fig. 3.10, table 3.2). A blue patch in the backfield curves as well as the red patch in the IRM acquisition show a maximum of M_{rs} between 16 and 120 minutes of milling at low energies. Comparing the 400 rpm data to the high energy milling shows a similar patch at much lower milling times (1-10 min, see arrow in fig. 3.11), pointing towards a faster alloying process and grain size reduction at higher energies. Using this relation it is likely that a homogeneous alloy is achieved after only 10 minutes of milling at 1100 rpm, an increase in milling efficiency by a factor of approximately 40 over 400 rpm milling times. Saturation remanence peaks at 2 min ($M_{rs}(2 \text{ min}, 1100 \text{ rpm}) = 4.9 \text{ Am}^2/\text{kg}$) and declines to a minimum at 10 minutes then increases again. Coercivity ($B_c(2 \text{ min}, 1100 \text{ rpm}) = 3.7 \text{ mT}$) peaks at 2 min, decreases at 10 min followed by an increase to $B_c = 5.4 \text{ mT}$, while B_{cr} continuously increases with increasing milling time with a maximum of $B_{cr} = 26.7 \text{ mT}$.

High energy milling causes a continuous decrease in saturation magnetization after 10 min of milling. This could be an indication for oxidation, due to a lower M_s value of iron oxides. However, Curie temperatures and XRD do not show a significant oxide contribution; e.g., there is no evidence for Curie temperatures corresponding to magnetite or hematite. Using the increased milling efficiency to compare the high to the low energy milling, the sample milled for 240 min at 1100 rpm would correspond to 9600 minutes (160 hrs) of milling at 400 rpm. Milling times of that length have been shown to produce amorphous alloys [Hamzaoui et al., 2003, Suryanarayana, 2001], which could explain the anomalous behavior of the saturation magnetization with increasing milling time. Unfortunately X-ray diffraction data is not available for this alloy at the time of this writing, thus the presence of an amorphous phase cannot be tested.

Neither 400 rpm nor 1100 rpm samples approach an SD-like value for remanence (fig. 3.10e) or coercivity ratios (fig. 3.10f and table 3.3), even though their size supposedly approaches the proposed SD range for iron [Butler & Banerjee, 1975, Muxworthy & Williams, 2015]. There are several possible explanations that could lead to this.

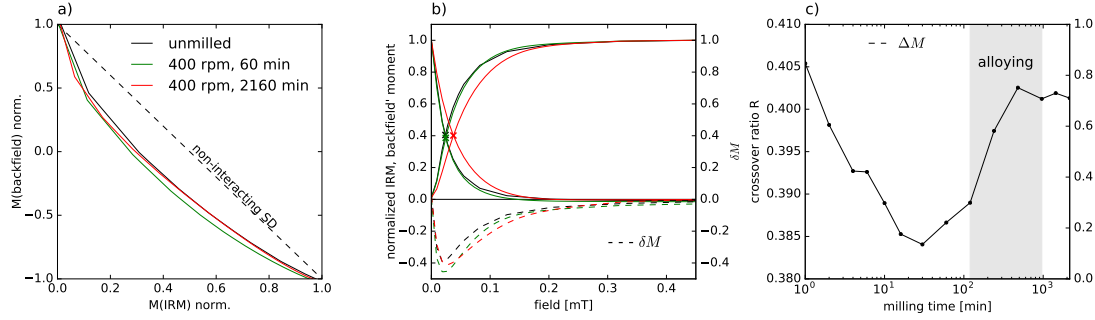


Figure 3.12.: Visualization of interactions. **a)** Henkel plot for unmilled and milled powders, dashed line shows ideal Henkel line for non interacting single domain particles **b)** Cisowski plot and $\delta M(H)$. Crosses mark the crossing point (R) of backfield and IRM curves. **c)** shows the change in interactions with milling time. Solid line shows the crossing points in the Cisowski plot and dashed line the integral over all $\delta M(B)$ values. Shaded part shows alloying region (400 rpm).

Interactions, both electrostatic and exchange coupling, can influence on the magnetic properties of a material [Mørup et al., 2010], that can, for example, alter the SP-SD threshold in magnetite [Muxworthy & Williams, 2009]. Wohlfarth [1958] showed, that IRM acquisition and backfield have a linear relationship in the absence of interactions. In an IRM acquisition, an initially demagnetized particle assembly is magnetized in successively larger magnetic fields. This saturated IRM moment is then demagnetized and replaced by an equal but opposite magnetization in a backfield measurement.

Several ways to show if a sample experiences interactions exist. The Henkel plot [Henkel, 1964] utilizes the relationship from Wohlfarth [1958]. A non-interacting particle system shows a linear relationship when the backfield moment is plotted against the IRM acquisition (fig. 3.12a). A different method is the Cisowski plot where both the IRM acquisition as well as an alternating field (AF) demagnetization of an SIRM are plotted against the magnetic field [Cisowski, 1981]. The

crossing point of the two curves (crossover ratio R) has a value of $0.5 \times M_{rs}$ if the particles are non interacting. In many cases it is more convenient to use the reduced backfield moment ($M'_{\text{backfield}}(B) = 0.5 \times (M_{rs}(B) + M_{\text{backfield}}(-B))$) instead of an AF demagnetization (fig. 3.12b) and typically gives similar results [Jackson, 2007]. Deviations from these criteria, a non-linear Henkel plot or crossover points $\neq 0.5$, indicate the presence of interactions. A way to determine the type and strength of the interactions is to calculate the $\delta M(B)$ value.

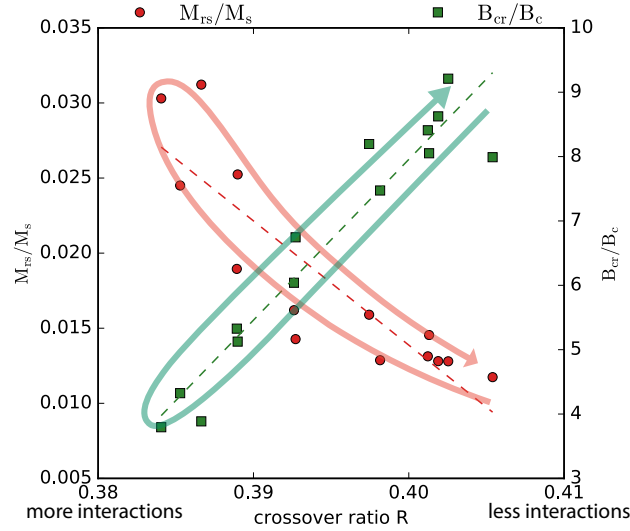
$$\delta M(B) = M'_{\text{backfield}}(B) - [1 - 2M_{\text{IRM}}(B)]$$

Positive values of $\delta M(B)$ indicate a dominance of exchange coupling, while negative values show that interactions are predominantly caused by dipolar interactions [Gao et al., 2001].

The Henkel plot for all samples is non-linear and the crossover points in the Cisowski plot appear at values lower than 0.5 for all samples (fig. 3.12). This indicates that the material is harder to magnetize than demagnetize. Dashed lines in fig. 3.12b show the $\delta M(B)$ value for each field step. Dipolar interactions dominate and cause negative $\delta M(B)$ values until saturation is reached. With increased milling times at 400 rpm, the crossing point of the Cisowski plot decreases from 0.410 to 0.385 at 60 minutes of milling (fig. 3.12c) and increases during alloying to 0.403 at 480 min. Comparing this to the rock magnetic data in fig. 3.10, shows that with decreasing grain size towards the SD range, interactions become more pronounced. This is especially visible when the crossover ratio is plotted against the remanence and coercivity ratio. When M_{rs}/M_s and B_{cr}/B_c trend towards more single domain like values, interactions become more important (low R values in fig. 3.13). At this stage the sample is still an inhomogeneous two component system, because the alloying process is not yet completed. Most likely grains of various compositions between pure iron and pure nickel exist. During alloying, the ratios increase again towards multidomain like values. This is somewhat surprising since the grain size is still lowered during alloying.

In an attempt to minimize interactions, the samples of the composition $\text{Fe}_{80}\text{Ni}_{20}$

Figure 3.13: Remanence ratio and coercivity ratio versus the crossover points determined from the Cisowski plot. Arrows indicate path of increasing milling time. Dashed lines show the linear correlations.



were subjected to several procedures. Grinding nano-particles with an inert material has been shown to decrease interactions [Xu et al., 2004], so we diluted the material with SiO_2 -powder and milled the diluted mixture for 15 min at 200 rpm to homogenize the mixture as described in the samples section. While the procedure seemed to reduce interactions for nanoparticles of $\alpha\text{-Fe}_2\text{O}_3$ [Xu et al., 2004], no reduction could be found for $\text{Fe}_{80}\text{Ni}_{20}$ particles. This is likely due to the much higher remanence of FeNi metals compared to $\alpha\text{-Fe}_2\text{O}_3$. In a second step the procedure was repeated, with the addition of 10 wt.% oleic acid. Oleic acid is a common surfactant used for coating nanoparticles [e.g. Mørup et al., 2010, Yin & Chow, 2009]. A mixture of 20 ml Heptane and 10 ml oleic acid was produced and 100 mg sample were added. The suspension was placed in an ultrasonic bath for 60 min. Hysteresis loops, backfield curves and IRM acquisition of these samples did not change in form nor indicate a decrease in magnetic interaction.

First Order Reversal Curves

First order reversal curves (FORC) help visualize the magnetic state of a sample and can be used to discriminate between different magnetic components [Pike et al., 1999, Roberts et al., 2014]. The possibility of assessing magnetic interac-

Table 3.3.: Coercivity and remanence ratios for all milling times for the Fe₈₀Ni₂₀ composition. Milling time longer than 240 min was not possible at 1100 rpm.

time (min)	B _{cr} /B _c		M _{rs} /M _s	
	400 rpm	1100 rpm	400 rpm	1100 rpm
1	8.0	4.7	0.012	0.022
2	7.5	4.4	0.013	0.028
4	6.7	5.4	0.014	0.022
6	6.0	5.6	0.016	0.019
10	5.3	7.4	0.019	0.015
16	4.3	7.3	0.025	0.017
30	3.8	5.4	0.030	0.023
60	3.9	5.4	0.031	0.024
120	5.1	5.7	0.025	0.024
240	8.2	5.1	0.016	0.029
480	9.2		0.013	
960	8.4		0.013	
1440	8.6		0.013	
2160	8.1		0.015	

tions among particles make FORC measurements the ideal tool for characterizing the samples for this study [Roberts et al., 2014].

The diagrams are calculated from partial hysteresis loops. From a saturated state of the sample, the field is decreased to a reversal field H_a and the loop is measured while the field is increased until saturation is reached again. After each partial loop H_a is decreased. From the moments at the applied field H_b and reversal field H_a , ($M(H_a, H_b)$) one can determine the FORC distribution ($\rho(H_a, H_b)$) by calculating the mixed second derivative [Pike et al., 1999]:

$$\rho(H_a, H_b) = -\frac{\partial^2 M(H_a, H_b)}{\partial H_a \partial H_b}$$

It is more convenient to change the coordinate system from H_a, H_b to $H_u = (H_a +$

$H_b)/2$ and $H_c = (H_b - H_a)/2$ [Roberts et al., 2014]. Since the mixed second derivative increases the measurement noise, sophisticated smoothing algorithms have to be employed [e.g. Egli, 2013].

The FORC diagram measured for $\text{Fe}_{80}\text{Ni}_{20}$ milled for 1440 minutes at 400 rpm was measured using very fine field steps ($500 \mu\text{T}$) so that the narrow coercivity band is sufficiently covered. The data were corrected for thermal and instrumental drift with all processing done with the mathematica package VARIFORC by Egli [2013].

Despite the apparently multidomain hysteresis loops, the processed FORC diagram reveals the presence of particles with a high coercive force. The central ridge, marked by (1) in fig. 3.14 indicates the presence of single domain particles. The coercivity distribution along the peak extends to fields $> 150 \text{ mT}$ much higher than coercivities determined from hysteresis loops ($B_c = 3.5 \text{ mT}$). However, the main, much stronger peak ((2) in fig. 3.14) is located at $H_c = 0$ and spreads $\pm 50 \text{ mT}$. Such a peak is typically interpreted as a multidomain contribution to the FORC distribution.

A slight downward shift can be seen in the central ridge. Super paramagnetism (SP) is a phenomenon that arises when particles are so small that the thermal energy ($k_B T$) spontaneously changes their magnetization. Super paramagnetic particles do not contribute remanent magnetization within the typical timeframe of a measurement but the decay of its magnetic moment can be visible in FORC diagrams. The presence of superparamagnetic particles in a sample can shift the central ridge towards low H_c values [Roberts et al., 2014] and cause a downward shift [Roberts et al., 2001]. The occurrence of these features, together with the grain sizes determined by XRD suggests that some of the particles after milling for 1440 minutes are in a superparamagnetic state. Furthermore a small negative contribution (3) can be seen at negative H_u values. This indicates interactions between particles, in agreement with the Henkel and Cisowski plots.

The magnetic moment of these particles, scaled by the saturation magnetization,

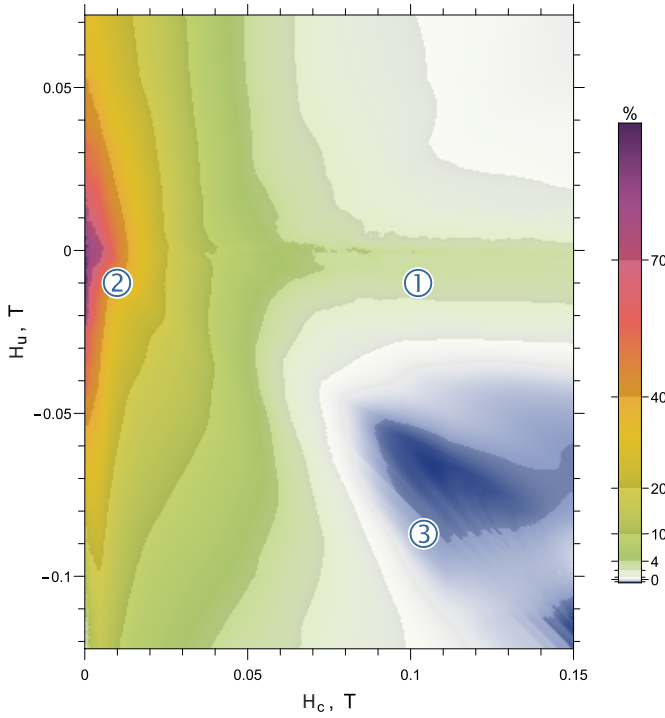


Figure 3.14: High resolution FORC diagram of $\text{Fe}_{80}\text{Ni}_{20}$ milled for 1440 minutes at 400 rpm (10.9 nm).

Measurements were performed on a VSM with $500\mu\text{T}$ step sizes between measurement points. Calculations to construct the diagram were done using VARIFORC [Egli, 2013].

- 1) shows central ridge
- 2) shows a maximum at $H_c = 0$
- 3) shows a negative contribution caused by interaction fields

can be described by:

$$\frac{M}{M_s} = \coth\left(\frac{\mu H}{k_B T}\right) - \frac{k_B T}{\mu H} = L\left(\frac{\mu H}{k_B T}\right) \quad (3.2)$$

Where μ is the magnitude of the magnetic vector of the particle, H is the applied field, k_B is the Boltzmann constant, T is the temperature and L is the Langevin function. This shows that an assemblage of super paramagnetic particles can be described by the Langevin function.

A common technique in rock magnetism is to model hysteresis loops and coercivities with a series of hyperbolic base functions (tanh and sech) [Leonhardt, 2006]. These have been shown to accurately describe hysteresis loops for single as well as multidomain particles [Jackson & Solheid, 2010, von Dobeneck, 1996].

This gives two separate properties that can be used to model the hysteresis behavior of a sample and estimate the SP contribution of the the system.

1. Superparamagnetic particles can be described by the Langevin function
2. Other particles can be described by by hyperbolic base functions

First the hysteresis is decomposed into their remanent hysteretic (M_{rh}) and in-

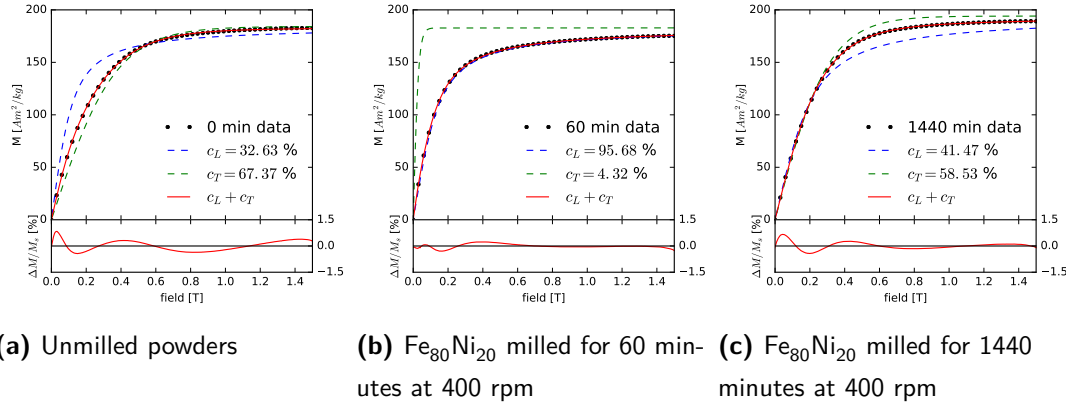


Figure 3.15.: Examples for fitting Langevin and hyperbolic base functions to the measurement data, using eq. (3.5) for three different milling times. Only positive fields are shown. Black circles show the measured data. Dashed blue line shows the Langevin part, green dashed line shows the tanh component of the fit, scaled by M_s . The red line shows the fit using both components. The misfit (in percent of the M_s value) is shown in the lower part of the plot.

duced hysteretic (M_{ih}) parts [von Dobeneck, 1996]. The induced hysteretic part is the mean of the two hysteresis branches and the remanent hysteretic part is their difference.

$$M_{rh} = [M^-(B) - M^+(B)]/2 \quad (3.3)$$

$$M_{ih} = [M^-(B) + M^+(B)]/2 \quad (3.4)$$

Where $M^+(B)$ is the upper, descending and $M^-(B)$ is the lower, ascending branch of the hysteresis. Since M_{rh} is the difference between the two branches, it represents the non reversible components and can be used to determine coercivities and remanence. The M_{ih} on the other hand only contains the reversible (induced) magnetization of the hysteresis loop [von Dobeneck, 1996]. Using a least squares approach a linear combination of the two function is fit to M_{ih} as determined by eq. (3.4). The function used to fit the hysteresis loops is:

$$M(B) = c_L M_s L(B/b_1) + c_T M_s \tanh(B/b_2) \quad (3.5)$$

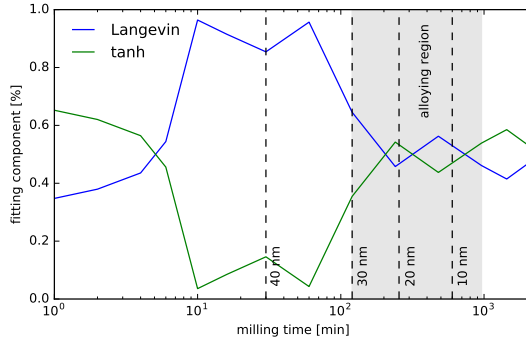


Figure 3.16: Components from fitting a combination of Langevin function and tanh to the induced hysteretic part of the hysteresis with eq. (3.5). Weights of the two components as a function of milling time. Dashed lines indicate grain sizes, shaded area shows the alloying region as determined by XRD.

c_L is the amount of Langevin-type behavior and c_T is the amount of *tanh*-like behavior ($c_L + c_T = 1$). b_1, b_2 are scaling factors that change the steepness of the functions. While the values determined from the fit can not be taken as the absolute value of the amount of SP, it can give an indication on the main constituent of the particle system.

Fitting the unmilled powder (fig. 3.15a) gives a c_L value of 33% ($c_T = 67\%$) so tanh is the main component. At low fields (< 0.4 T), the Langevin component overestimates the magnetization and the tanh component fits the data better owing to the multidomain character of the sample. A maximum of c_L is found in the 10-60 minute range (fig. 3.16). At milling for 60 minutes, the c_L component accounts for 96% of the data and on its own gives a good representation of the measurement. At these milling times the grain sizes of both Fe and Ni are reduced from several μm to 30-40 nm (see dashed lines in fig. 3.16) without much alloying visible in the diffraction spectra. The high c_L component indicates that a part of the Fe or nickel might be in a SP state and therefore is better approximated by a Langevin function.

For even longer milling times c_L increases again and both components are equally important ($c_L \approx c_T$). Since longer milling times cause a reduction in grain size and this reduction ultimately leads to an increase in the amount of superparamagnetic particles in the sample, seeing an increase in the c_T component is somewhat surprising. However, during alloying, the two phase system is continuously transformed into a single phase $\text{Fe}_{80}\text{Ni}_{20}$ alloy, which likely possess a different single

domain threshold size [Muxworthy & Williams, 2015]. A change in stable single domain size could explain this behavior.

3.7. Dependence on Ni concentration

3.7.1. Thermomagnetic Measurements

Magnetic moment versus temperature curves for all other compositions were measured on the VFTB using two different methods. Approximately 20mg of sample was heated in air at a rate of 60 °C/min. In a second experiment, in order to create a reducing environment, a similar amount of sample was thoroughly mixed with twice the mass of powdered sugar as a reducing agent. Curie temperatures were calculated using the maximum of the second derivative using the RockMag analyzer [Leonhardt, 2006]. The measured curves can be seen in fig. 3.17.

When heated in air, the moment ($B = 120$ mT) is more or less stable up to 400°C for samples with less than 10 at.% nickel and then decays more or less linearly. This stands in stark contrast to the sharp transition of pure iron when heated in inert atmosphere (fig. 3.8). A change from convex to concave is visible for nickel concentrations higher than 6%. This change in demagnetization behavior can be attributed to the continuous transformation from the α -Fe to the non magnetic γ -Fe phase at high temperatures [Dunlop & Özdemir, 1997]. These alloys technically do not show a Curie temperature but the austenite transformation, where the bcc phase is transformed into the fcc phase. In the literature however, the two are often used synonymously. The transition temperature decreases with increasing Ni concentration as can be seen in fig. 3.2. All samples show low Curie temperatures when compared to literature values (fig. 3.18). Especially the samples with the composition $\text{Fe}_{80}\text{Ni}_{20}$ yielded low Curie points ($T_c(\text{Fe}_{80}\text{Ni}_{20}, 400 \text{ rpm}) = 538^\circ\text{C}$, $T_c(\text{Fe}_{80}\text{Ni}_{20}, 1100 \text{ rpm}) = 543^\circ\text{C}$).

Heating the samples with sugar shows a more rounded demagnetization for $\text{Ni} < 8$ at.% and yields sharper transitions with slightly higher ($19 \pm 3^\circ\text{C} [\text{Ni} \leq 12 \text{ at.\%}]$)

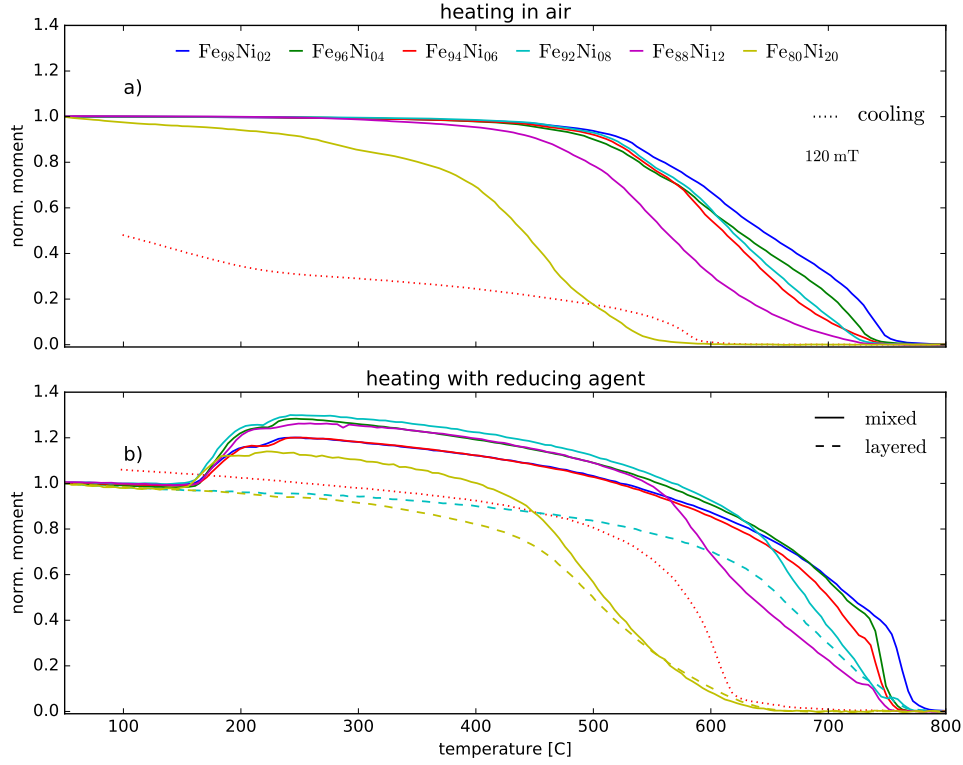
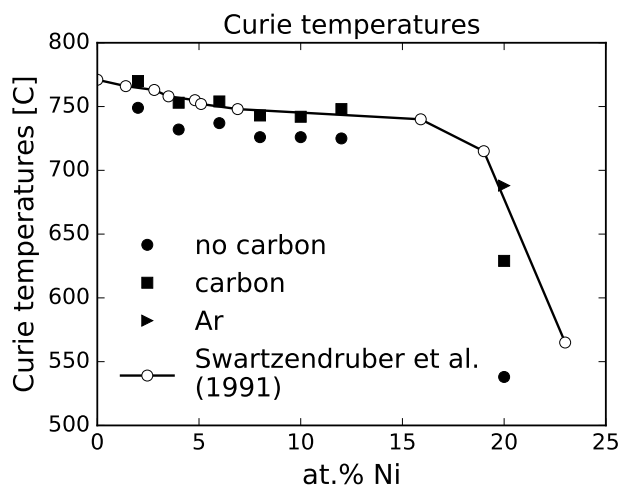


Figure 3.17.: Moment versus temperature measurements in air for all compositions. **a)** shows samples heated in air. dashed line shows cooling curve for $\text{Fe}_{94}\text{Ni}_{06}$, other cooling curves omitted for clarity. **b)** shows thermomagnetic measurements carried out in a reducing environment (i.e. added carbon). Carbon mixed into the sample powder is shown as solid lines, while measurements with a separate layer of carbon is shown as dashed lines.

Curie points in accordance with previous studies [Swartzendruber et al., 1991]. All curves with added sugar show a slight inflection just before the Curie temperature, which might be caused by the incorporation of carbon from the sugar into the FeNi structure [Wilson, 1994]. An exception is the composition $\text{Fe}_{80}\text{Ni}_{20}$ (see fig. 3.18), which still gives a low transition temperature. Comparing the VSM (fig. 3.8) and VFTB curves $\text{Fe}_{80}\text{Ni}_{20}$ shows a more convex shape and a Curie temperature close to that determined by earlier studies [Kuhrt & Schultz, 1993, Wasilewski, 1981a].

Upon cooling, a 15-30% increase in magnetic moment at 150°C and a less pro-

Figure 3.18: Curie temperatures, determined from heating cycle for $\text{Fe}_{(100-x)}\text{Ni}_x$ compositions. Heating was done in air (circles), in Ar (triangle) and with sugar as reducing agent (squares). Heating rate $60^\circ\text{C}/\text{min}$. Magnetic field during heating was 100 mT. White circles show data from [Swartzendruber et al., 1991].



nounced increase at 215°C is visible after heating with carbon (fig. 3.17). In order to verify that this behavior is not related to a reduction of iron oxides, the carbon was added as a separate layer underneath the sample material. In this case the sugar was not mixed and did not get into direct contact with the sample but would hopefully still create a reducing atmosphere upon heating. Two examples can be seen as dashed lines in fig. 3.17. The absence of the initial increase indicates that it is not related to a reduction of oxides but more likely an incorporation of carbon into the crystal structure. Since the transition temperature for both mixed carbon and layered carbon are comparable to within 5°C , alteration to oxide phases in the samples is unlikely.

When cooled in air most of the material is transformed to magnetite (see dashed red line fig. 3.17a). In alloys with a high Ni concentration ($>6\%$) a second inflection can be found at temperatures lower 250°C . Similar to the austenite ($\alpha \rightarrow \gamma$) transformation, this increase in magnetization correlates to the transformation from $\gamma \rightarrow \alpha$ [Dunlop & Özdemir, 1997, Wasilewski, 1981a]. The transformation is barely visible in most measurements due to the magnetite contribution and a more thorough analysis isn't possible. Interestingly, the cooling curves after heating with sugar also show an increase in magnetization (see red dotted line in fig. 3.17b) on cooling. It is located at a higher temperature and recovers most of

the pre heating magnetization. Oxidation to magnetite can be excluded since the transition does not correlate with the Curie point of Fe_3O_4 . Adding carbon, can change the martensite transformation temperature [Wilson, 1994], which leads to different heating and cooling behavior in the thermomagnetic curves. This should be investigated more closely, especially for C-rich meteorites (e.g., carbonaceous chondrites). Unfortunately our experiments only show that there is an effect but we can not quantify it. Experiments under more controlled conditions and atmosphere are in preparation.

3.7.2. Rock Magnetic Measurements

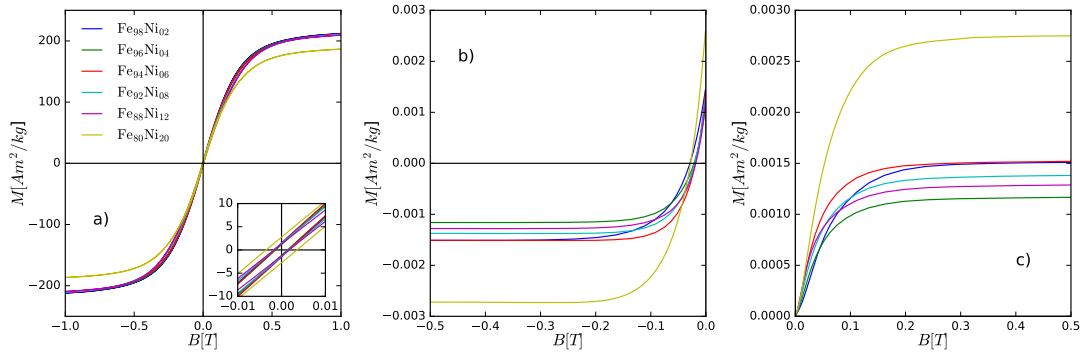


Figure 3.19.: Hysteresis (a), backfield (b) and IRM acquisition (c) measurements for different $\text{Fe}_{100-x}\text{Ni}_x$. Inset in a) shows a zoom into the hysteresis loop at fields from -10 - 10 mT.

Using the same measurement protocol and corrections as described earlier, hysteresis loops, backfield curves and IRM acquisition curves were analyzed for the other compositions. Figure 3.19a) shows that hysteresis loops for concentrations with $\text{Ni} < 12$ at.% vary little in shape or parameters. The exception is $\text{Fe}_{80}\text{Ni}_{20}$, with increased remanence ($M_{\text{rs}} = 2.75 \text{ Am}^2/\text{kg}$) and coercivity ($B_c = 3.5 \text{ mT}$) and lower saturation magnetization ($M_s = 190 \text{ Am}^2/\text{kg}$). This is especially visible in the backfield and IRM measurements (fig. 3.19b and 3.19c).

The saturation magnetization (fig. 3.20a) is close to the literature value of pure iron ($M_s(\text{Fe}) = 217.6 \text{ Am}^2/\text{kg}$) [Crangle & Goodman, 1971]) and constant with

increasing nickel concentration up to 12 at.% Ni ($M_s = 214.9 \pm 0.7 \text{ Am}^2/\text{kg}$). Measured M_s values correspond well with data of ball milled alloys published in earlier studies (see. fig. 3.20) [Hamzaoui et al., 2003, Kuhrt & Schultz, 1993]. For higher nickel concentrations (≥ 12 at.%), the saturation magnetization decreases. Our $\text{Fe}_{80}\text{Ni}_{20}$ data show lower values than previous work. However previous studies used stainless steel milling balls that could potentially contaminate the sample material and increase the iron content [Koch, 1997]. Since M_s varies little for low Ni content, contamination would only be visible in alloys with higher Ni concentrations.

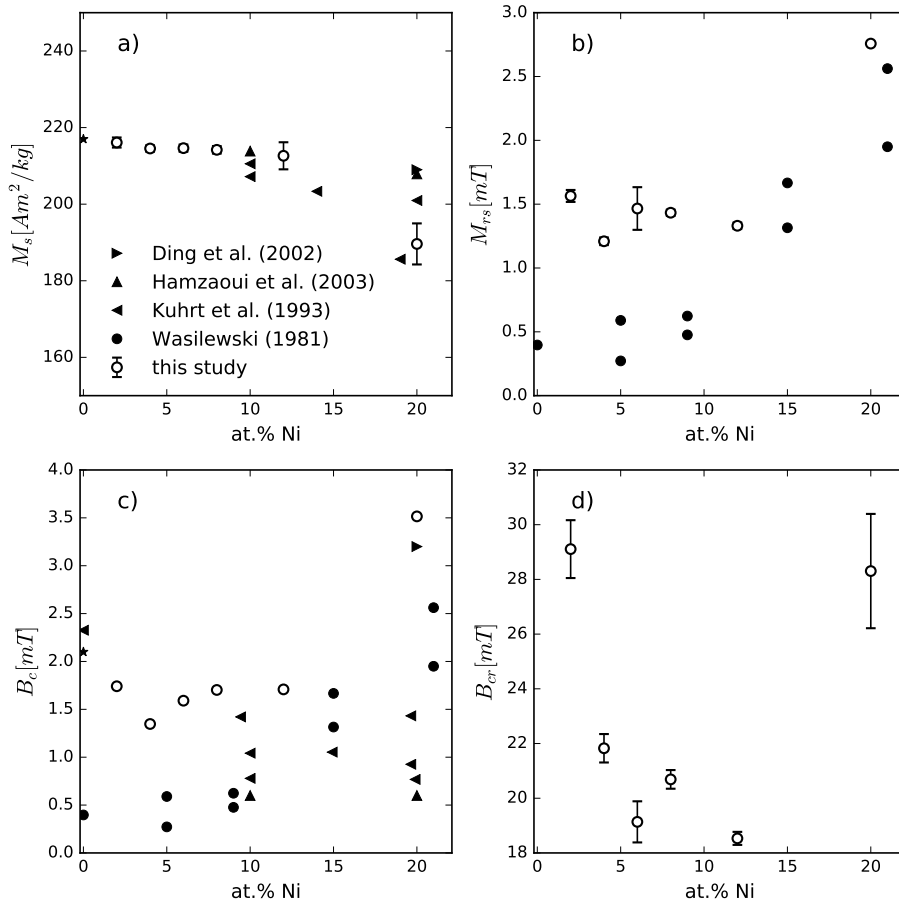


Figure 3.20.: Mean results from hysteresis measurements for different compositions. Errorbars are one standard deviation ($n=3$), for M_s and B_c errorbars are smaller than the marker. Star marks M_s for pure iron [Crangle & Goodman, 1971] and B_c for pure iron [Glaubitx et al., 2011].

The saturation remanence (fig. 3.20b) is similarly stable for low Ni compositions. $\text{Fe}_{80}\text{Ni}_{20}$ on the other hand nearly doubles the M_{rs} values of the other samples. Saturation remanence is rarely measured in studies focused on magnetic properties from a material sciences perspective. To our knowledge, Wasilewski [1981a] is the only study reporting M_{rs} for Fe,Ni alloys of different compositions and yielded lower values than our alloys when Ni ($< 12\%$). We note that the samples used in the Wasilewski [1981a] study were produced by an entirely different method. Iron-nickel wire was brought to melting temperatures in a drop tower where the molten droplets were solidified by "zero g" solidification. Compared to the method used here, their samples are not only much bigger (1 mm spheres) but likely contain less crystal defects. Nevertheless it seems that increasing the Ni concentration to more than 15 at.% increases the remanence carrying capability.

As with the other hysteresis parameters, little change is found in coercivity (fig. 3.20c) with increasing Ni content for ≥ 12 at.%. $\text{Fe}_{80}\text{Ni}_{20}$ has the highest value with 3.5 mT while other compositions are close to half that value ($B_c = 1.6 \pm 0.1$ mT). While the coercivities are low ($B_c = 1.5 - 3.5$ mT) compared to other minerals, they are large compared to the samples of other studies, both ball milled and zero-g synthesized. Literature values for B_c generally have a large scatter but show a trend towards larger coercivities with higher Ni content. To our knowledge our study is the first to determine B_{cr} values for synthetic FeNi alloys. Figure 3.20d shows that compared with B_c the coercivity of remanence is large. It rapidly decreases with increasing Ni from $B_{cr}(\text{Fe}_{98}\text{Ni}_2) = 29 \pm 1.0$ mT to a minimum at 12 at.% nickel ($B_c(\text{Fe}_{28}\text{Ni}_{12}) = 19 \pm 0.2$ mT).

3.8. Discussion

Magnetic properties of mechanically alloyed iron-nickel powders change significantly during the milling process. In a first stage the grain sizes of the different starting powders are reduced while maintaining a two component system. This is visible by an increase in M_{rs} and B_c and a decrease in B_{cr} consistent with a

trend towards more single domain behavior. At longer milling times, hysteresis and backfield measurements show the start of the alloying process as a decrease in remanent magnetization and coercive force. The magnetic measurements seem more sensitive to the subtle changes due to alloying than X-ray diffraction. Milling for 960 minutes at 400 rpm produces fully alloyed powders. Grain size reduction takes place within the first 400 minutes of milling (400 rpm) and little to no change is visible in the XRD data for milling times longer than 2160 minutes. No other magnetic phase could be found in XRD or thermomagnetic curves; high M_s values, close to that of iron, further indicate the purity of the samples.

The mean particle size for alloyed powders after 1440 min at 400 rpm is ≈ 10 nm, within the theoretical limits for single domain iron [Butler & Banerjee, 1975, Muxworthy & Williams, 2015]. This raises the question as to why the hysteresis parameters do not indicate the presence of single domain material? Strong dipolar interactions as seen in the Henkel and Cisowski plots are known to bias the magnetic state of a sample [Mørup et al., 2010]. Moreover particles of this size (≈ 10 nm) have very large surface area to volume ratios. Uncompensated spins on the surface can intensify interactions [Bødker et al., 1994]. Unfortunately the magnetic measurements do not give conclusive evidence for a domain state interpretation. Two conflicting interpretations are possible. Either the particles are still predominantly multidomain, or the grain size has already passed the single domain threshold and is in a mainly superparamagnetic state. The fact that interactions and the SP component of the Langevin fit are at a maximum after 60 minutes (400 rpm) of milling suggests that grain sizes are in fact approaching the SP size. The central ridge in the FORC distribution leads to a similar conclusion. This question could be resolved by the measurement of frequency dependent susceptibility, which is able to quantify the SP contribution [Bowles et al., 2009]. These measurements are planned in the near future.

An increase in Ni concentration to ≤ 12 at.% has only little effect on the magnetic properties. Curie temperatures, M_s , M_{rs} and coercivity vary little. A much larger effect is seen in the remanence coercivity (fig. 3.20), which decreases from 29 mT

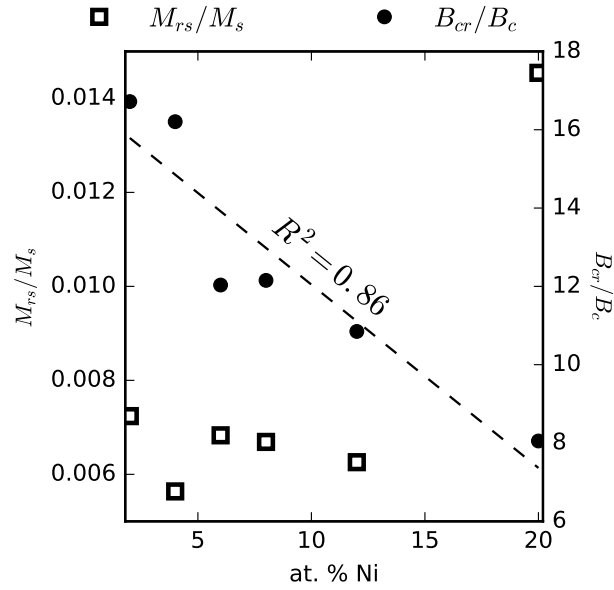
at 2 at.% to about half for 12 at.%. Since milling conditions are the same for all compositions, it seems unlikely that their grain size or internal strain varies considerably. Thus the increase in remanence coercivity is most likely related to the increased Ni content. Remanence coercivity is a little known quantity for Fe–Ni alloys, but seems to be a good indicator for Ni concentration in α -Fe alloys.

Figure 3.21 shows the changes of B_{cr}/B_c and M_{rs}/M_s ratio with nickel concentration. The remanence ratio stays constant with increasing Ni while the coercivity ratio decreases almost linearly. A change in the SD/MD threshold is a potential cause for the decrease in B_{cr}/B_c . Whether the threshold size decreases or increases can not be determined with confidence until the domain state of the samples is clarified. High coercivity ratios can be due to the presence of superparamagnetic as well as multidomain particles [Dunlop, 2002a]. This causes an ambiguity in the interpretation. Assuming most particles in the sample are too small (SP), the single domain to superparamagnetic threshold needs to be lowered in order for the 10 nm particles to show a more single domain behavior. On the other hand, if the particles are too large (i.e. MD) a shift SD/MD threshold would need to be shifted towards larger sizes.

Independent of whether the samples produced here are too large (i.e. in a MD state) or too small (SP), our study shows the limits of mechanical alloying for producing single domain iron nickel alloys. Larger particles can not be produced by mechanical alloying alone, because fully alloyed, homogeneous powders need milling times of 960 minutes (400 rpm) or more. At this time the size is already reduced to ≈ 11 nm. On the other hand, much longer milling times will be needed to reduce the size further due to the exponential decay of milling efficiency. This is further complicated by the theoretical calculations that show that iron possesses only a very narrow SD range, which is likely also true for FeNi alloys [Muxworthy & Williams, 2015]. Finding the right milling conditions, to produce a purely single domain sample seems unlikely.

The samples produced here show rock magnetic values typical of those found in iron bearing meteorites [e.g. Gattacceca et al., 2014, Wasilewski, 1981a]. Curie

Figure 3.21: Remanence and coercivity ratios for different mechanically alloyed (400 rpm, 2160 min) $\text{Fe}_{100-x}\text{Ni}_x$ compositions. Dashed line shows linear regression.



temperature measurements showed that the identification of remanence carriers in meteorites may be more complicated than previously thought. Thermally acquired remanences for Ni concentrations of more than 6 at.% are likely thermal chemical remanences due to the martensitic transformation ($\gamma \rightarrow \alpha$) as discussed by [Wasilewski, 1981a]. Furthermore both the martensite as well as the austenite ($\alpha \rightarrow \gamma$) transitions depend on the carbon concentration in the sample and on the oxygen fugacity of the heating experiments. Especially higher Ni concentrations (i.e. $\text{Fe}_{80}\text{Ni}_{20}$) suffer from this. Heating $\text{Fe}_{80}\text{Ni}_{20}$ in air yields a Curie temperature at 538°C , adding carbon 629°C , while heating in Ar, 688°C . Adding carbon can therefore shift the martensite transition temperatures [Wasilewski, 1981a, Wilson, 1994]. Furthermore Kuhrt & Schultz [1993] showed that the $\gamma \rightarrow \alpha$ transition can be influenced by the maximum temperature of the measurement. When measuring thermomagnetic curves on $\text{Fe}_{80}\text{Ni}_{20}$, they found the martensite temperature to be 180°C by heating to 690°C , while cycling to 900°C yielded $\approx 200^\circ\text{C}$. Both martensite and austenite transitions are commonly used to characterize magnetic minerals in meteorites [e.g. Butler, 1972]. Given these findings, interpreting the magnetic signal from carbon-bearing meteorites like carbonaceous chondrites (2

wt% of organic matter) may be further complicated [Sephton, 2002].

3.9. Conclusions

We have successfully synthesized α -Fe,Ni alloys with different Ni-concentrations ranging from 2-20 at. % by mechanical alloying. XRD as well as thermomagnetic measurements show no sign of contamination of the samples by other magnetic phases. The alloying process was monitored by hysteresis, backfield and IRM acquisition measurements. The magnetic and XRD data identify three distinct phases during the mechanical alloying process: 1) grain size reduction of the elementary powders (≈ 60 min at 400 rpm), 2) alloying (60 - 960 min), and 3) slow reduction of grain size of the finished alloys. Milling efficiency increases 40 times when increasing the rotation speed from 400 rpm to 1100 rpm. The ability to easily synthesize FeNi alloys in the laboratory opens up many new ways to study the magnetic carriers of most meteorites. The samples can be used to produce better calibration factors for non-heating paleointensity methods and generally help to understand this complicated mineral system.

Grain sizes on the order of 10 nm do not show typical SD characteristics. This is likely due to strong magnetic interactions between particles. However, at this stage determining whether the particles are too large (MD) or too small (SP) to lie in the narrow SD range is not possible. Further measurements of frequency dependent susceptibility are planned to resolve this question. The data, however suggest a change in SD threshold with increasing Ni content, which was previously only hypothesized [Muxworthy & Williams, 2015].

Determining the composition of the magnetic carriers is crucial to the interpretation of the signal. Thermomagnetic measurements are a commonly used tool. The study shows that the $\alpha \rightarrow \gamma$ and $\gamma \rightarrow \alpha$ transitions are extremely sensitive to the experimental setup. Heating and cooling rate [Wilson, 1994], maximum heating temperature [Kuhrt & Schultz, 1993] and carbon content influence the results. In the absence of chemical analyses, identifying magnetic minerals could thus be prone to misinterpretation and these effects need to be studied in more detail.

4. Design of a Paleomagnetic Oven

Paleomagnetism is the study of the ancient Earth's magnetic field preserved in the rock record; it is this discipline that has led to several of the major modern discoveries of the Earth system, including the theory of plate tectonics. Magnetic information can be retrieved from trace amounts of ferromagnetic minerals present in most rocks that record the paleomagnetic field direction and intensity in at the time the rock formed [Kirschvink et al., 2008]. The geomagnetic direction is recorded either during sedimentation (detrital remanent magnetization [DRM]) or by cooling through the rocks Curie temperature (thermal remanent magnetization [TRM]). This information can be obtained from rock samples collected in the field and measured in the laboratory. A typical paleomagnetic investigation is based on stepwise thermal or alternating field demagnetization of hundreds or thousands of samples. Samples are successively stepwise heated to increasing temperatures and the natural remanent magnetization (NRM) is measured after each heating cycle at room temperature. This procedure is very time consuming because the samples are often heated to 10 or more temperatures.

Since the first paleomagnetic laboratories were founded in the 1950's, technological advancements in magnetometer technology, Superconducting Quantum Interference devices (SQUIDS) have made measuring the NRM increasingly fast, accurate and convenient. In recent years more sophisticated systems that are capable of measuring large numbers of samples autonomously have been developed. These not only have the advantage of minimizing human error but also considerably increases the throughput of samples. In addition, the user does not have to be present at all times. Several such systems are used in laboratories all over

the world. Some of them have the capacity to measure more than 90 samples in succession (e.g. University of Bremen (unpublished), California Institute of Technology [Kirschvink et al., 2008], SushiBar at our institute [Wack & Gilder, 2012]). The latter system, named after its visual similarity to a running sushi restaurant, is able to measure 99 samples without user intervention.

Several commercial paleomagnetic furnaces are available for purchase (table 4.1) and the maximum number of samples that can be heated simultaneously vary between 30-80. In order to utilize the full capacity of the SushiBar, an oven with a bigger capacity was needed. During the course of my doctoral thesis I planned, built and tested a paleomagnetic thermal demagnetizing furnace with a capacity for ca. 100 samples.

Table 4.1.: Comparison of commercially available thermal demagnetizing furnaces.

Name	No. samples ¹	Field Noise (nT)	Thermal Gradient
SOGO fine-TD ²	30	<30nT	< 5%
ASC Model TD48 ³	48	50/10nT	10 °C
MMTD80A ⁴	80	10nT (66 nT ⁵)	6 °C

4.1. Setup

The furnace needs to be able to heat and cool a complete set of samples within the measurement time of the SushiBar, which is approximately 4 hours [Wack, 2016]. Heating and cooling in the same region is impractical so we decided to implement a two chamber system. The two chambers are connected so that the boat, that holds the samples can be easily pushed from the heating section into the cooling section of the furnace. This approach is adopted by most commercial ovens and reduces the working time because two sets of samples can be heated and cooled simultaneously.

¹simultaneous heating

²Zheng, Zhong et al. [2010]

³ASC scientific [2016]

⁴Magnetic-Measurements [2016], Shaw [2010]

⁵Zheng et al. [2010], Zheng, Zhong et al. [2010]

4.1.1. Magnetic Shielding

Rocks that cool in a magnetic field typically acquire a thermoremanence, therefore samples have to be isolated from direct current (DC) magnetic fields (e.g. the Earth's field). Passive shielding is possible by using materials with a high magnetic permeability such as Permalloy or Mu-Metal (Iron–Nickel alloys (70-80% Nickel), that are frequently used in paleomagnetic furnaces. Their high permeability creates a low resistance path for magnetic field lines, which are diverted from the inside of the furnace and pass through the material. Depending on number and thickness of the layers, modern shielding techniques can reduce the low frequency magnetic fields inside a furnace to a few nT, a fraction of the Earth's magnetic field.

The magnetic permeability of Mu-Metal strongly depends on the crystalline structure and internal stresses. High temperature annealing removes stress and recrystallizes the material, which results in an increase in permeability and reduces coercivity [Sekels GmbH, 2016]. Since machining and annealing of the material requires special equipment, tools and large furnaces, design and construction of the shield was outsourced to the company *Magnetic Shields Ltd.*

Specifications for the shield was a reduction of the static magnetic field to <10 nT within the sample region (1200 mm) of the furnace. A two layer system with 2mm thick Mu-Metal cylinders (fig. 4.1) was proposed by the company and two removable lids were added to the shield to reduce field leakage at the ends. Figure 4.1 shows a schematic drawing of the shield and the magnetic field inside, which does not exceed 15 nT in the cooling chamber.

4.1.2. The Boat

The boat is designed for 96 cylindrical samples, 2.5 cm in diameter and 2.2 cm in height that are arranged in a hexagonal pattern with $16 \text{ samples} \times 6 \text{ rows}$. Samples in the center of the boat would be thermally shielded by the surrounding samples,

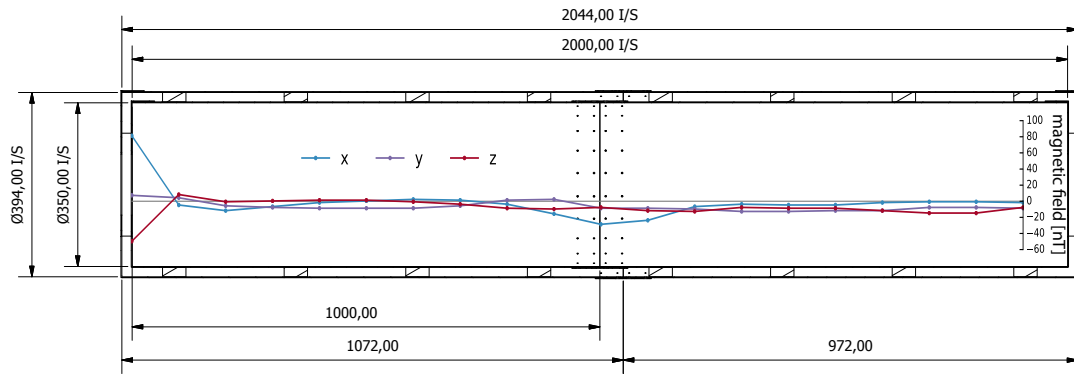


Figure 4.1.: Cross section of the magnetic shield designed and constructed by Magnetic Shields Ltd., all measurements in mm.

to balance out uneven heating. I incorporated an Inconel 600 tube in the center with the samples placed in a circle around it (see fig. 4.2a). The tube has a higher thermal conductivity (14.9 W/m K [Special Metals Corporation, 2008]) than the rocks (typically 2-12 W/m K [Eppelbaum et al., 2014]) and flattens the thermal gradient inside the chamber. Furthermore, it increases the flow of air during cooling thereby decreasing cooling time.

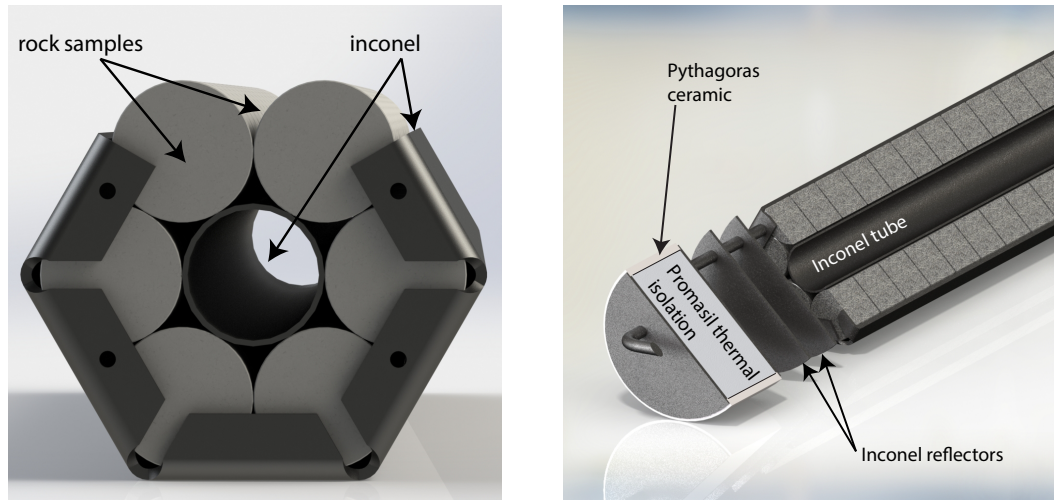
In order to thermally isolate the heating region from the rest of the furnace, Promasil⁶ plugs, covered by Pythagoras⁷ ceramic tubes (fig. 4.2b) were placed at the ends of the boat. We positioned four radiation shields between the thermal isolation and the sample region of the boat. They reflect infrared radiation back into the sample chamber and decrease thermal gradients (Dr. John Shaw, personal communication).

4.1.3. Heating Chamber

An important concern when designing a demagnetizing furnace is the thermal gradient inside the sample chamber. It needs to be low, otherwise some rocks may already demagnetize because their temperature is higher, while others still carry

⁶High performance calcium silicate, Promat GmbH

⁷The Morgan Advanced Materials Company plc.



(a) Front view of a filled boat. Shows the hexagonal arrangement of samples around an Inconel tube.

(b) Cross section of the boat. Left half shows a slice through the boat with thermal reflectors and ceramic, promasil thermal isolation.

Figure 4.2.: Design of the sample boat. It holds 96 samples in a hexagonal pattern with an Inconel 600 tube in the center **a)**.

a magnetization. This can be falsely interpreted as differences in mineralogy or blocking temperature of the sample. To counter this we split the heating chamber into three zones with separately controlled heating sections.

Three heating zones are arranged symmetrically with respect to the center of the tube with the inner one spanning the entire sample zone (372 mm). Each of the zones has a separate thermocouple (TC) (T1-T3 fig. 4.4) so that they can be controlled individually. For proper temperature control, the thermocouple needs to measure the temperature inside that zone so the thermocouples for channels 1 and 3 were placed as close as possible to the sample region (marked by an x in fig. 4.4). Each section is controlled by a commercially available multi-zone PID⁸ temperature controller (*Nolden Reglersysteme*, Germany, 6×3.5 kW, 16A).

Most thermal demagnetizing units consist of temperature controlled resistance

⁸proportional–integral–derivative controller

furnaces. The simplest design would be a single high resistance wire wound in a single spiral around the main furnace tube and glued into place. However, we must also achieve a near zero field (< 10 nT [Collinson, 1982]) in order to avoid the acquisition of partial thermal remanent magnetizations (pTRM). A solenoid with only one path creates a magnetic field (Ampere's law). Thus, wiring can produce magnetic fields that render the measurements unusable. Paleomagnetic ovens typically have bifilar windings to counteract this effect. Several such designs (fig. 4.3) are possible. Preliminary testing showed that the wiring scheme fig. 4.3a) would be the most suitable for this project. A single wire for each section is used, bent 180° around a piece of ceramics and wound back, resulting in antiparallel current directions so the magnetic fields cancel out.

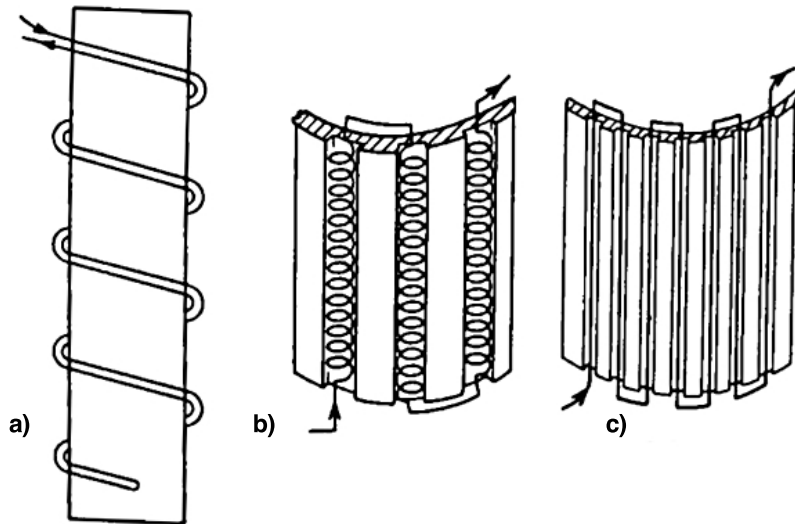


Figure 4.3.: Some common heating wire schemes. Oppositely running electrical currents cancel out their magnetic fields generated during operation. [Collinson, 1982]

The wire dimensions are chosen so that the heat produced by the element can be dissipated fast enough. A common way of calculating this is by the surface loading, the power per surface area of the element.

$$S = \frac{P}{l \times d \times \pi} \quad (4.1)$$

Where S is the surface loading, P is the power of the element in Watts, l the length of the wire and d is the diameter of the wire in cm. According to the Kanthal [2002] handbook, the suggested surface loading for a spiral element in air, that is embedded in grooves should be between 4-5 W/cm²(at 800 °C). To keep within the surface loading limits and the maximum power of the controller, a diameter of \varnothing 0.7 mm was chosen for the auxiliary (outer) heating sections and a diameter of \varnothing 1 mm for the inner (main) one. Surface loading values calculated with eq. (4.1) are $S_{1,3} = 13.9$ and $S_2 = 2.1$ W/cm² for outer and main section, respectively. Due to the high surface loading, the maximum power for the outer sections was reduced to 30% of the maximum value, resulting in $S_{1,3} = 4.2$.

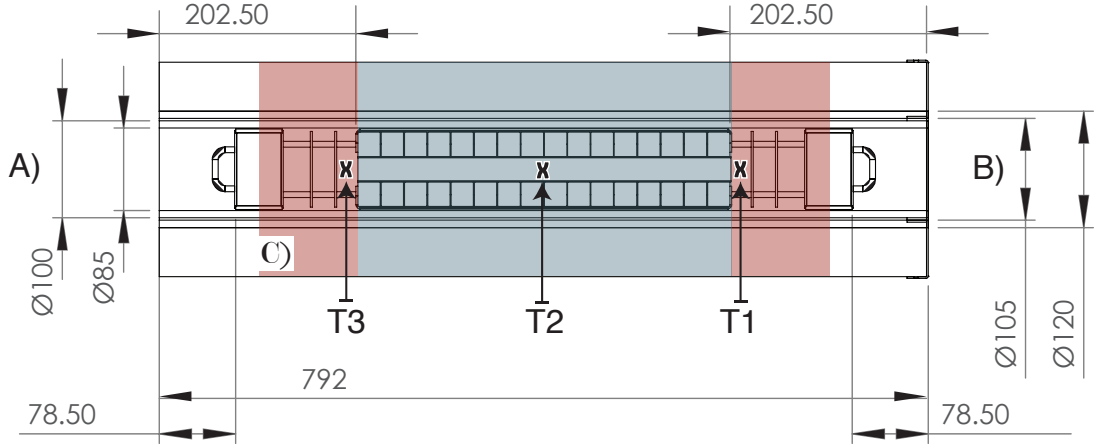


Figure 4.4.: Heating chamber dimensions and heating section / thermocouple positions with boat positioned inside. Red sections are the outer, auxiliary heating sections. A) shows the dimensions of the inner heating tube, B) shows the dimensions of the protection half tubes. C) is the thermal isolation made from Promaform. T1-T3 point to approximate thermocouple positions marked with a x.

The tube material (Sillimantin 60) was chosen for its superior thermal stability and a higher porosity that makes the material more stable against temperature gradients (see fig. 4.4 for size measurements). Sillimantin is slightly softer than alumina ceramics, thus it is easier to machine so more sophisticated designs can be adopted. Two 1 mm deep grooves with a pitch of 10 mm and an offset of 5 mm (fig. 4.5b) were ground using an electroplated diamond grinding wheel over the length of all three sections. Using ceramic glue (Cotronics Resbond 903HP) at

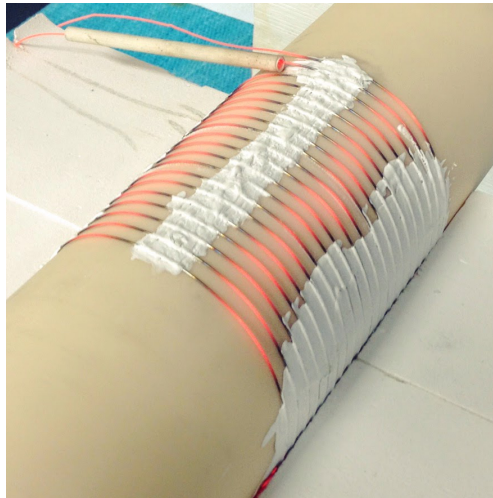
Table 4.2.: Wiring configuration for each channel of the final heating chamber design. Channel 1&3 are reduced in power, full power in brackets. Wire is Nicrothal 80 from *Kanthal*

sect.	length	wire \varnothing	Ω / m	wire length	windings	Ω	power (kW)
1	125 mm	0.7 mm	2.81	7.85 m	25	22.0	0.7 (2.4)
2	372 mm	1.0 mm	1.39	25.75 m	74	32.7	1.7
3	125 mm	0.7 mm	2.81	7.85 m	25	22.0	0.7 (2.4)

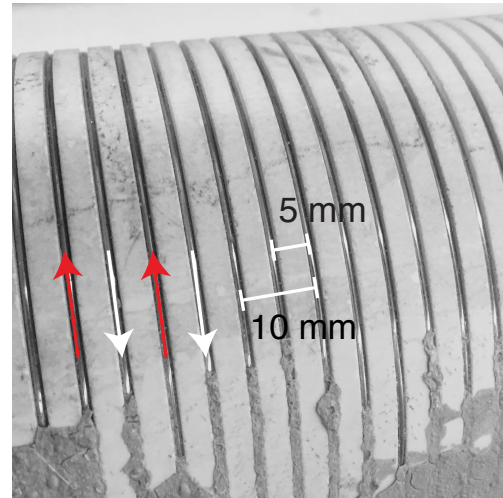
several positions, the wire was directly embedded into the grove of the ceramic. In the case that the glue does not hold, the wires were fastened with an additional layer of quartz fabric (fig. 4.6).

The heating chamber was designed as a separate unit, and thus can be easily taken out of the frame and replaced if needed. Thermal isolation is achieved by two half shells made of a mixture of aluminum-silicate and aluminum-oxide fabric (Promaform). It is able to withstand temperatures of up to 1600 °C with a low thermal conductivity of 0.22 W/m K. When fully assembled, the heating chamber is held together by two aluminum plates connected by aluminum strips. Inconel rings facilitate the connection with the cooling section and center the heating chamber inside of the frame. A cross sectional view of the completed furnace can be seen in fig. 4.8. Before it can be inserted, the thermocouples are slid through ceramic pipes into the main chamber and copper cables are connected to the heating wires.

Operation of the furnace is done via software written by Michael Wack. A screenshot can be seen in fig. 4.7. The user enters the desired set temperature in 1). Heating times are set automatically by the software and shown in 2) but can be adjusted if needed. Adding an email address into field 3) allows the user to be automatically notified after the set temperature is reached and when the heating run is finished. Heating trends for all three channels are shown in 4) and can be saved using the save function (5). Panels 6 (set temperatures) and 7 (measured temperatures) show the current state of the furnace. The heating ratio is the supplied power to each heating section and can be seen in 8). The remaining



(a) First heating test with bifilar winding on top of AL23 alumina ceramics. 1mm wire are glued in strips of ceramic glue.



(b) Second version of Sillimantite 60 heating tube. Wire is glued into grooves. Arrows show the current direction. Distance between grooves = 5 mm

Figure 4.5.: Tubedesign AL23 (a) and Sillimantite 60 (b) heating chamber tubes.

heating time is displayed in 9).

The software handles offset corrections and heating rate changes in the background without user interference. Offsets are adjusted dynamically as a function of temperature to ensure optimal accuracy. Each second, the measured temperatures from all 6 channels, heating ratios and several other parameters are written to a file on the computer that can later be consulted to check for irregularities in the heating pattern. Even though only 3 channels are used for the normal operation of the furnace, all 6 are recorded so that calibrations can be performed. To our knowledge this is the first software controlled, fully automatic paleomagnetic demagnetization furnace.



Figure 4.6.: Final design of the heating chamber. Sillimantin inner tube with wires (top) covered by Pythagoras outer tube (bottom). The heating wires are glued into the grooves and covered by high temperature quartz fabric (blue strip top). Red arrows mark the positions for the thermocouples. The heating chamber is thermally isolated with Promaform.

4.1.4. Cooling Chamber

To insure a low magnetic field environment, all materials have to be non-magnetic like aluminum [Collinson, 1982]. The frame for the oven was made from off the shelf parts, produced by *item*. It is comprised of the outer frame (fig. 4.8 and 4.9) and an inner cooling chamber. A hexagonal item piece with an inner tube with \varnothing 87 mm serves as cooling chamber and connects for the rest of the frame construction.

One concern when constructing the furnace was the structural integrity of the

aluminum at high temperatures. Samples in the cooling chamber can reach up to 700 °C, potentially heating up the room, frame and Mu-metal shield. Thus, we decided to add a water cooling system (water temperature = 15 °C). The horizontal item pieces have a continuous hole through their center, that are normally used for connecting them to other pieces. These holes have a diameter of 5 mm in the outer frame and 8 mm in the inner frame. Copper pipes were installed directly into the frame and the water is pumped into the inlet, through the four cooling chamber pipes and finally through the outer frame. A leak detector was installed at the base of the oven. Electricity is automatically cut if any water escapes.

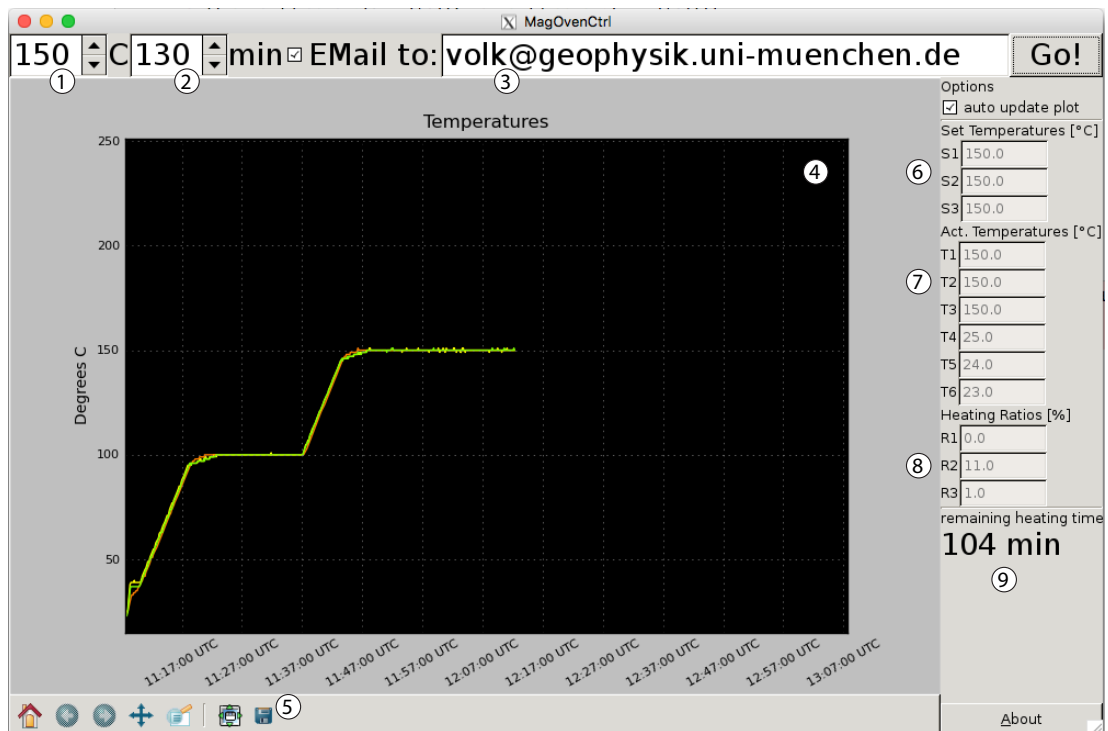


Figure 4.7.: Screenshot of the software (written by Michael Wack) that controls the furnace. User enters the T_{set} in 1. 2 shows the pre-determined heating time, 3) field for email notification after heating is completed, 4) visual representation of the heating run as measured on the three thermocouples T1-3 can be saved with 5). Current state of the furnace can be seen in 6) set temperature, 7) measured temperature, 8) heating ratio. Remaining heating time as entered in 2) can be seen in 9).

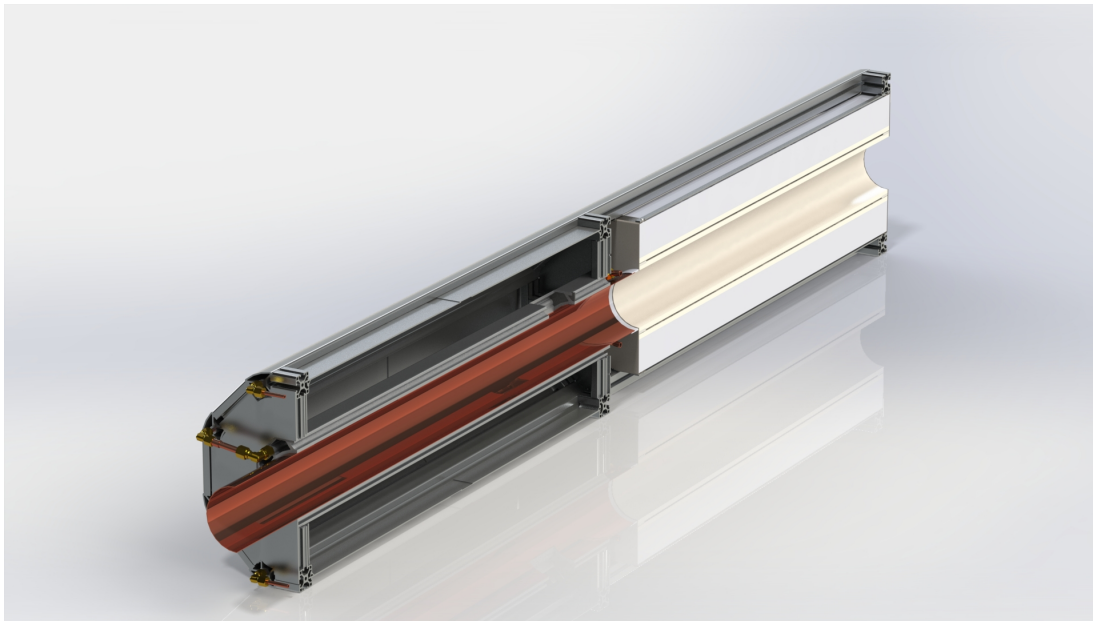


Figure 4.8.: Section through the center of the oven chamber. Left is the cooling chamber with the long copper tube sticking out. On the right side is the modular heating chamber.

High temperature furnaces can considerably heat the laboratory. Furthermore, rocks may contain organic material, that burns and smells. In order to minimize these effects and decrease cooling times, air cooling was implemented (fig. 4.10). Room air is pulled through holes into the sample chamber. As the air passes through the Inconel tube and around the samples, it transports heat away from the samples. In order to keep a flat thermal gradient in the heating chamber, air is diverted away through an opening at the top of the chamber and pulled out of the furnace by a vacuum that sits well outside the room.

4.2. Calibration and Testing

Temperatures are measured by thermocouples inside the heating chamber, therefore the samples' temperatures are only known indirectly through prior calibration. Given enough time, the whole system will be in thermal equilibrium and the sample temperature should be equal to the measured temperatures, but generally

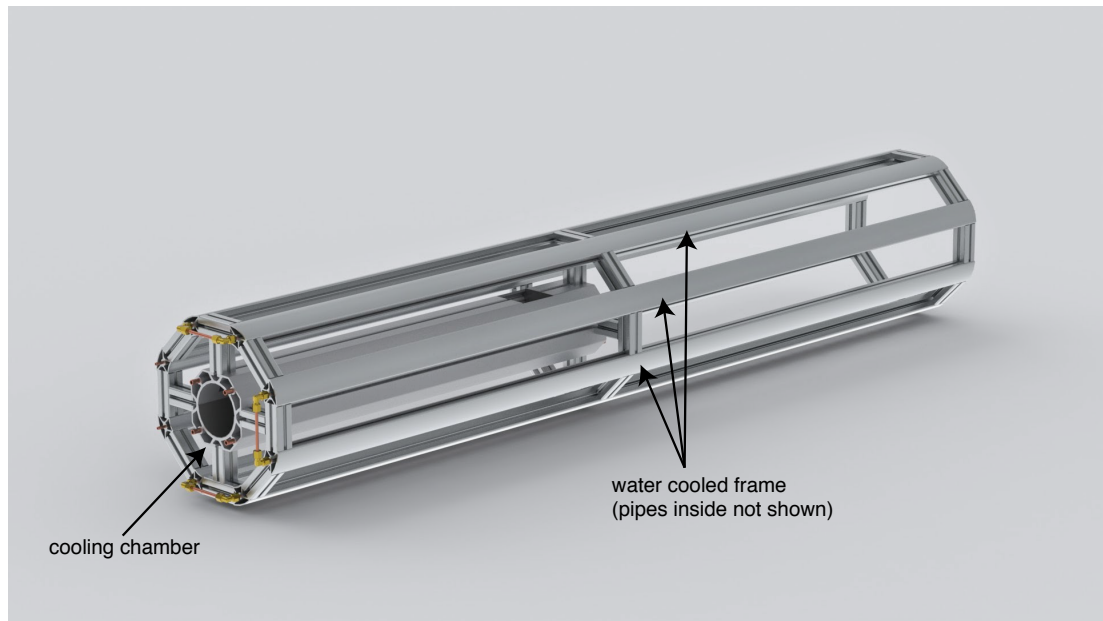


Figure 4.9.: The empty Frame for the paleomagnetic oven including the cooling chamber. Water-cooling is achieved by copper pipes inside the outer (\varnothing 5mm) and inner (\varnothing 8mm) frame pieces. Empty space on the right is for the heating chamber. The final frame is closed to ensure air circulation.

small offsets are unavoidable. Calibration measurements were done to correct for these offsets and to check for the linearity of the thermal gradient inside the furnace. Offsets can occur when the thermocouple position for one channel differs to the position of another channel (e.g. is slightly closer to the heating wire). On top of this, calibration measurements enable us to determine optimal heating and cooling times.

The first step is to optimize the settings in the controller (PID). Choosing wrong PID settings can cause the temperatures to "overshoot" and/or oscillate around the set temperature. Several heating runs were done in order to find a suitable PID setting in the controller. The furnace was heated to 400 °C while monitoring the overshoot and oscillation. Then the controller parameters were adjusted accordingly and a new run to the same temperature was started. This was repeated until the setting showed no visible overshoot or oscillation. A heating rate of 7 °C per minute was chosen and is reduced to 1 °C/min upon reaching the a

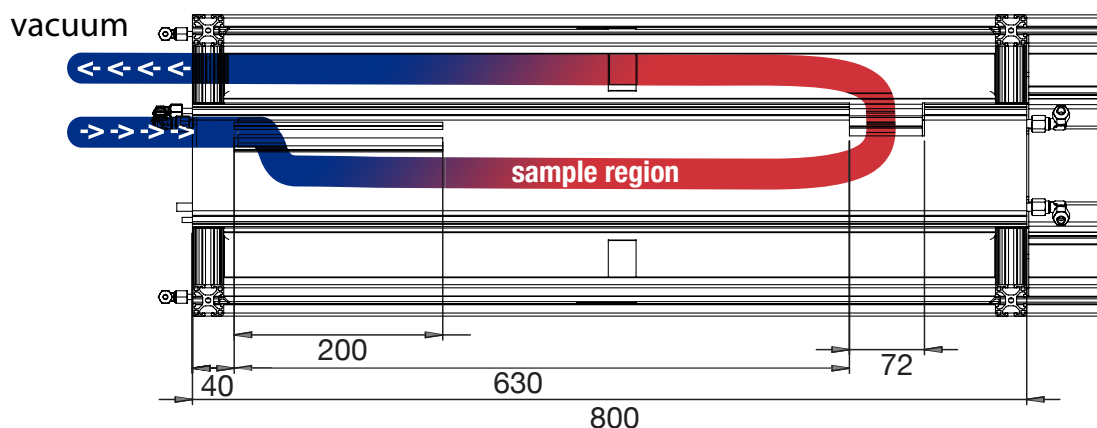


Figure 4.10.: Configuration of the cooling region. Cold air is sucked through the item profile with a high-powered vacuum into the sample region, passes over the samples and is sucked out through an opening in the profile. All measurements are in mm.

temperature $10\text{ }^{\circ}\text{C}$ lower than T_{set} . In this way, the heating rate is constant for all temperatures up to the maximum of $700\text{ }^{\circ}\text{C}$ (fig. 4.12b).

To calibrate absolute temperatures and heating/cooling times, a full boat (96) of rock samples was prepared. Three of the rocks were fitted with thermocouples (S_1, S_2, S_3) by drilling a hole into the cylindrical sample and fixing the thermocouple into the hole with high-temperature ceramic.⁹ glued into their center with a high temperature ceramics glue. This simulates the thermal inertia of the case during intended operation and allows for the calibration of needed heating and cooling times as well as absolute temperature calibration of the furnace. The samples were placed in the top row of the boat with two samples at the ends (S_1, S_3) and one (S_2) in the center of the boat.

Measurements were done in $100\text{ }^{\circ}\text{C}$ steps from $100\text{--}700\text{ }^{\circ}\text{C}$. For each step I calculated the offset ΔT for each thermocouple ($T_n - S_n$). A linear regression was used to fit the offsets. The slopes of the linear regression was used to dynamically adjust the offset in the ovens operating software.

⁹The number of the channel in the controller, thermocouple in the heating chamber and thermocouple in the test sample correspond to each other, e.g. channel 1 \rightarrow T1 \rightarrow S1.

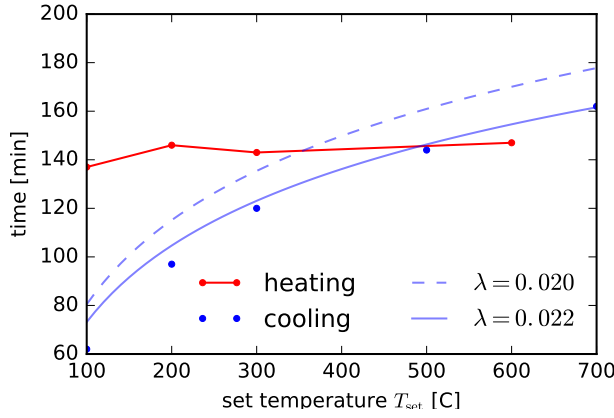


Figure 4.11: Heating and cooling times measured during calibration. Heating times (red) more or less constant for all set temperatures, while cooling times (blue) increase with increasing temperature. Blue lines show cooling times calculated using eq. (4.2) with $\lambda = 0.022$ (solid) and $\lambda = 0.020$ (dashed).

Finally several steps (100, 200, 300 and 600 °C) were repeated in order to check the accuracy of the offset calibration. The samples were placed in the furnace at room temperature and then heated to the set-temperature, where they remained for 2.5 hours in order to achieve thermal equilibrium. Figure 4.12a) shows that temperature overshoot in the sample chamber (T_{1-3}) are lower than $< 1\%$. Thermal gradients in the test samples showed a maximum thermal gradient (ΔT) of 5 °C at $T_{\text{set}} = 700$ °C.

Heating times (Δt_{heat}) and cooling times (Δt_{cool}) were calculated from the calibration measurements. Δt_{heat} is defined as the time needed for all three samples ($S_1 - S_3$) to reach the set temperature (T_{set}) to ± 1 °C, while the cooling time is taken after all samples reached a threshold temperature ($T_{\text{thresh}} = 45$ °C) after being pushed into the cooling chamber. Heating times are more or less independent of T_{set} ($\Delta t_{\text{heat}} = 143 \pm 3$ min), when heating started from room temperature (T_0) (table 4.3 and fig. 4.11).

Cooling times on the other hand depend on the set temperature (fig. 4.11). The decay approximately follows $T = T_{\text{set}} \exp(-\lambda t) + T_0$, with the decay constant λ depending on the set temperature as well as the position in the boat. Samples close to the exit of the cooling chamber are passed by the cold air first, thus they cool the fastest. The decay constants determined at the maximum temperature (700 °C) are $\lambda = 0.023/\text{min}$, $0.021/\text{min}$ and $0.035/\text{min}$ for $S_1 - S_3$, respectively. Since heat capacity between rocks may vary, a lower λ should be used, so that

Table 4.3.: Measured heating and cooling times for selected temperatures 100-700 °C. Calculated cooling times were determined using eq.4.2 with $\lambda = 0.2$. Values in brackets show thermal gradient ΔT (°C) determined from repeated heating experiment (see. fig. 4.12)

T_{set}	100	200	300	400	500	600	700
t_{heat} (measured) [°C]	137(2)	146(2)	143(2)	(0)	(5)	147 (4)	(5)
t_{cool} (measured) [°C]	62	97	120		144		162
t_{cool} (eq. 4.2) [°C]	80	115	135	150	161	170	178

cooling times are independent of rock type. Cooling times can be calculated with:

$$\Delta t_{\text{cool}} = \frac{\log \left(\frac{T_{\text{set}}}{45^{\circ}\text{C} - T_0} \right)}{\lambda} \quad (4.2)$$

Choosing a λ , 5% lower than the lowest value determined in the calibration measurements ($\lambda = 0.020$) calculated using e.q. (4.2) and the measured cooling and heating times for selected temperatures are shown in table 4.3 and fig. 4.11.

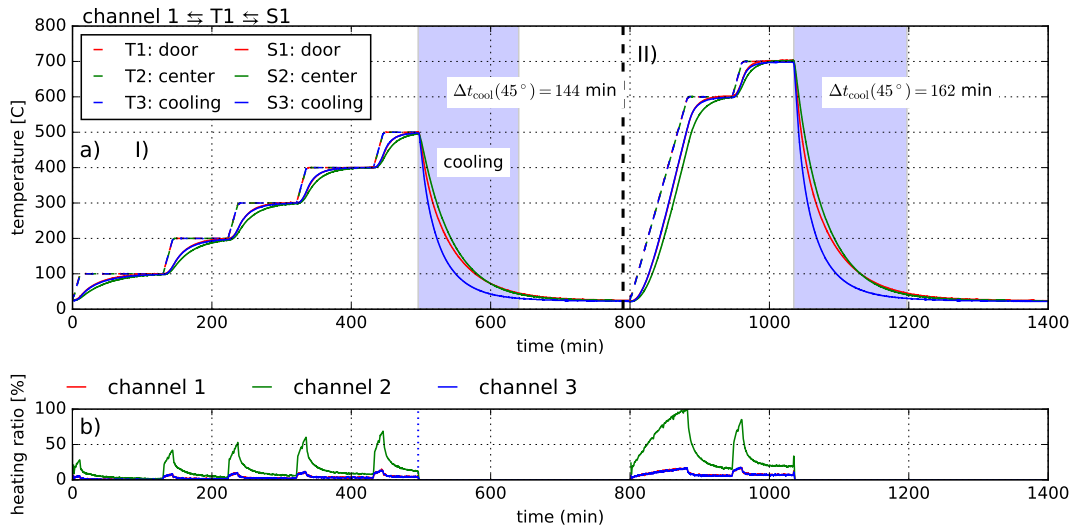


Figure 4.12.: a) Two final calibration tests (I: 100-500 °C, II: 600-700 °C). Thermocouple for channel 1 corresponds to T1 and the thermocouple in sample S1. Shaded region shows cooling of the samples. b) Heating ratios for I) show symmetry of channels 1 and 3.

4.2.1. Lowrie test

The so called Lowrie test [Lowrie, 2012] is commonly used in paleomagnetism to help determine the magnetic mineralogy of a rock. Some minerals like hematite ($\alpha\text{-Fe}_2\text{O}_3$) with a Curie temperature of 680 °C have high coercivities while others like magnetite (Fe_3O_4) with a Curie temperature of 580 °C have lower coercivities. To test for the presence of these phases, one can apply a strong magnetic field (e.g. 1 T) along one of the sample's axes (e.g. x). This gives minerals with a coercivity lower than the applied field a saturating remanent magnetization in that direction. A second, weaker field (e.g. 0.3 T) is then applied along an orthogonal axis direction (e.g. y), which causes a realignment of the moment for minerals with "intermediate" coercivities like magnetite. The third step is to apply an even weaker field (e.g. 0.1 T) along the third axis. One can characterize magnetic carriers of the sample as well as the blocking temperature spectrum of the mineral by thermally demagnetizing the sample and plotting their x, y, z components against temperature.

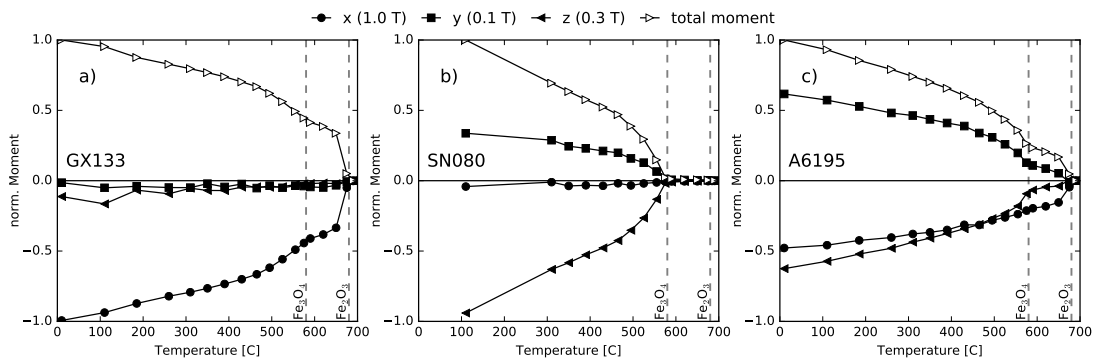


Figure 4.13.: Lowrie test of two samples. Three fields were applied to the sample. X(1 T), Y(0.3 T), Z(0.1 T). Dashed lines show Curie temperatures for magnetite 580 °C and hematite 680 °C.

We carried out Lowrie tests on several samples (fig. 4.13) to detect of several possible issues with the furnace (stray magnetic fields, temperature homogeneity, etc.). Internal temperature gradients could be seen if samples at one side of the boat demagnetize at different temperatures than samples on the other. Offsets in absolute temperature would be visible in the demagnetization pattern and Curie

temperatures. Furthermore, magnetic pollution could be seen if the samples acquire a remanence instead of lose a remanence.

Thermal demagnetization of three samples at different positions in the boat can be seen in fig. 4.13. Sample GX133 (fig. 4.13a) shows only a high coercivity component but two different minerals, visible by the inflections near the magnetite and hematite Curie temperatures. Demagnetization of a granite from the Sierra Nevada (SN080) reveals only one magnetic mineral. All of its magnetic moment is lost at a temperature of 570 °C, corresponding to magnetite with a slight amount of titanium. It also shows that when comparing it to GX133, a large portion of the moment is carried by low coercivity particles, likely in a multidomain state. Medium coercive, small magnetite particles are carrying the remaining part of the moment. Sample A6195 (fig. 4.13c) shows the demagnetization of two different minerals with largely different coercivities in the same rock. In the high coercivity component, only one Curie temperature, that demagnetizes at 670 °C (hematite) can be found. Most of the medium coercivity component on the other hand is demagnetized at a temperature of 570 °C around the Curie temperature of magnetite, with only a small fraction of the magnetization being stable to higher temperatures. At 570 °C the major part of the low coercivity component is unblocked.

All samples show smooth demagnetization up to 680 °C where the remaining hematite component is demagnetized. The Lowrie test shows that the set and real temperatures coincide well and the thermal gradient in the oven is negligible, because all samples demagnetize at the same temperature. No appreciable partial thermal remanence was acquired in any sample, which indicates that magnetic fields during cooling are insignificant.

4.3. Conclusions

The furnace is capable of heating 96 samples to a maximum temperature of $T_{\max} = 700 \text{ }^{\circ}\text{C}$ with a low ($\Delta T < 5 \text{ }^{\circ}\text{C}$) thermal gradient at T_{\max} . Figure 4.14

shows the finished furnace inside the Mu-metal shield installed in the laboratory. Temperature offsets were calibrated and do not exceed 5 °C. The magnetic field in the shield was < 15 nT over the length of the sample section of the furnace. During calibration and testing of the furnace we were unable to detect any remanence acquisition in the samples.



Figure 4.14.: Finished furnace inside the Mu-metal shield installed in the lab.

Heating times were determined from a cold state of the furnace and vary little with temperature ($\Delta t_{\text{heat}} = 143 \pm 3$ min). Cooling times can be calculated using eq. (4.2) and seen in table 4.3. A complete set of samples can be heated and cooled to the set temperatures in less than 330 min (5.5 hrs), when heating to 700 °C. Even though a single heating run takes longer than the average running time of the SushiBar (4 hrs), one boat can be heated while the second one is in the cooling chamber, thereby halving the time needed. Furthermore, heating times can be greatly reduced by using a pre-heated oven.

5. Conclusions

In order to reconstruct the features of the magnetic fields in the early solar system and planetesimal bodies, accurate and reliable estimates of the ancient field intensity are needed. At present, thermal remanent magnetizations (TRM) are the only form of magnetization that can be used for obtaining absolute paleointensities. Consequently, experimental protocols usually try to mimic this acquisition process. Since the classic Thellier-Thellier method can cause thermal alterations, especially in meteorites, other methods based on anhysteretic (ARM) and isothermal remanent magnetization (IRM) evolved [Weiss et al., 2010]. Non heating, relative methods are not grounded on a rigorous theory and have large margins of error. Thus paleointensities derived from meteorites often yield varying results. For one this is likely due to the magnetic mineralogy, which is not well understood. On the other hand, the acquisition process can be complicated and the resulting magnetization is often disturbed by pressure events or low temperature demagnetization. In the course of this study I have worked on confirming several open questions concerning the validity of paleomagnetic studies on meteorites.

Pressure cycling of rocks with a low-Ti pseudosingle domain magnetite can cause a loss of remanent magnetization and others have shown similar effects for different minerals. It mainly influences grains with low coercivity and unblocking temperatures. This can even happen at relatively low pressures (e.g. 0.6 GPa), which typically don't leave any petrographic indications. Since absolute paleointensity methods relate the natural remanent magnetization to a laboratory acquired thermally acquired magnetization, the loss of moment can cause a change in the slope in the NRM-TRM diagram and consequently an underestimation of

the past field intensity. Leading to the conclusion that paleointensities derived from pressurized materials can only be taken as a lower limit. Pressure cycling can also have an effect of the remanence carrying capability of the sample by lowering its mean unblocking temperature. Through straightening of the arai plots and apparently enhancing the quality of the data, the magnetic state of the sample can be misinterpreted.

On the other hand, demagnetization of pyrrhotite bearing samples due to low temperature cycling from their equilibrium temperature in space to room temperature on Earth has little effect on the remanent moment. This leads credibility to paleointensity derived from meteorites with pyrrhotite as a magnetic carrier for example the Martian meteorites. The pyrrhotite phase transition, which is an important tool for identifying the magnetic minerals in a sample has been intensely studied. The mechanism behind the transition, however is not clear and conflicting interpretations exist. Hysteresis loops in the the basal plane of the crystal show a increase in magnetic parameters during the transition. Surprisingly the values for coercivity of remanence increases faster with decreasing temperature than the coercivity of the crystal, yielding a coercivity of less than unity. Rotational hysteresis loops and backfield curves show a change from a six-fold symmetry above the transition to a fourfold symmetry below T_{Bes} . This indicates a crystallographic change rather than changes in interactions of superstructures.

Our data for iron-nickel alloys, the most common magnetic mineral in meteorites, are less encouraging. While being able to synthesize pure alloys with a relatively novel technique in earth sciences (mechanical alloying) no clear evidence for the presence of a single domain grain size could be found. SD remanence carrier, however are especially important when dealing with magnetizations that were acquired several billions of years ago during the formation of the solar system. Due to thermal relaxation effects the magnetic moment can only be stable for these timescales if the particle carrying it is in the single domain size range. The failure to find SD particles, even though grain sizes are within the proposed limits [Butler & Banerjee, 1975, Muxworthy & Williams, 2015] could be partly masked

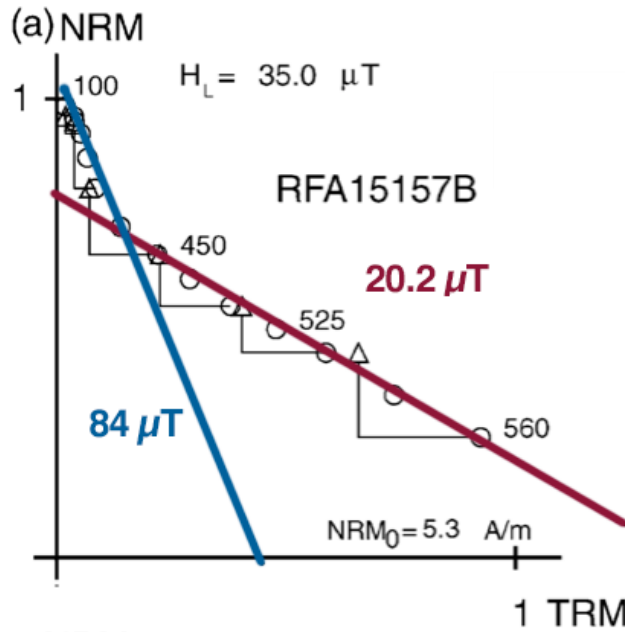


Figure 5.1: Arai diagram: Ambiguity of paleointensity determined from PSD and MD grains. The lower temperature portion would yield a paleointensity of 84 μT while the high temperature portion (right) only recovers an intensity of 20.2 μT [Chauvin et al., 2005]

by the presence of strong dipolar interactions in the sample. Moreover, our data shows that phase transitions in these alloys are sensitive to many factors, such as carbon content, heating and cooling rate and maximum heating temperature. This further complicates the interpretations of the remanent magnetization. The study shows that a lot more work has to be done in order to understand the magnetic signature of metal bearing meteorites. The synthesis technique described in here, however could pave the way for new experiments on synthetic Fe,Ni alloys, to further the understanding of their magnetic properties.

Outlook

Our community has generated an impressive number of paleointensity protocols, but the most commonly used methods are variants on the approach of Thellier & Thellier [1959] [Biggin & Perrin, 2007, Coe, 1967, Coe et al., 1978, Yu et al., 2004]. All of these methods require a linear dependence of TRM intensity on the inducing field and the additivity, independence, and reciprocity of partial-TRMs (pTRMs). These properties are exhibited by populations of non-interacting single-domain

(SD) grains, but not by multidomain (MD) or pseudo-single domain (PSD) particles [Levi, 1977]. However, most natural materials contain a range of magnetic grain sizes, which results in non-ideal behavior during paleointensity experiments. The prevalence of non-SD grains and thermochemical alteration during repeated heating cycles are the most frequent causes of failure in paleointensity studies.

Examples of non-ideal behavior are shown in fig. 5.1 and are manifest as excessive curvature in the Arai plots. This curvature causes ambiguity in calculations of the ancient magnetic field strength. Which part of the data set is more reliable? When higher temperature data points are discarded (blue line in fig. 5.1) the intensity may be overestimated. If one chooses to only use the higher temperature data, then the intensity may be underestimated (red line in fig. 5.1) [Biggin & Thomas, 2003, Chauvin et al., 2005, Dunlop, 2005]. In an effort to avoid this non-ideal behavior, some researchers have introduced alternative paleointensity protocols [Dekkers & Böhm, 2006, Fabian & Leonhardt, 2010, Xu & Dunlop, 2004], while others have developed experimental checks that can be incorporated into Thellier-style protocols to monitor the contribution of remanence from PSD and MD grains as well as their stability during repeated heating cycles [Biggin & Perrin, 2007, Coe, 1967, Coe et al., 1978, Krása et al., 2003, Riisager & Riisager, 2001, Yu et al., 2004]. Another approach has been to determine statistical parameters that can be used to exclude spurious data [Paterson et al., 2012, 2010, 2014, Perrin, 1998].

During the work of this study we found that pressure cycling preferentially demagnetizes the remanence held by PSD and MD grains, while leaving the remanence held by SD grains largely intact. By treating specimens to pressure treatments prior to paleointensity experiments, non-ideal behavior can be strongly inhibited and Arai diagrams straightened. This method begins by measuring a specimens natural remanent magnetization (NRM) and then pressure cycling to e.g. 1 GPa. The reduced NRM is remeasured (NRM_P) and the moment lost (ΔM_P) calculated. Then a standard Thellier-style experiment is conducted. For specimens containing Fe-rich titanomagnetite in predominantly PSD grain sizes, increasingly

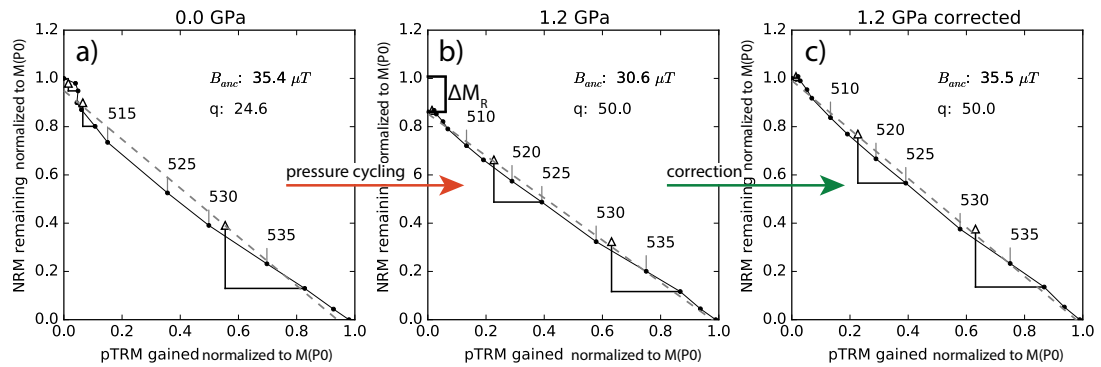


Figure 5.2.: Arai diagrams for the same sample before (a) and after pressure cycling (b) shows demagnetization ΔM_R . There is a significant decrease in curvature and the quality factor q increased by factor of 2. Data of b corrected for ΔM_R (c) gives correct paleointensity and increased q

large pressure treatments progressively reduce the curvature in Arai diagrams (fig. 5.2). The final paleointensity estimate from the pressure-cycled material correlates with the amount of pressure demagnetization. Thus, the magnetic moment lost after pressure cycling can be used to correct the generally lowered paleointensity to its correct value. Additionally, the quality factor (q) [Coe et al., 1978] increases with increasing pressure demagnetization. Since the quality factor has proven to be a good measure of the overall robustness of the data [Chauvin et al., 2005], this method of removing non-ideal remanences and then correcting for ΔM_P should lead to more robust data. This method may also allow specimens that would otherwise be dismissed from a study, because of their ambiguous NRM-TRM diagrams, to yield usable and reliable paleointensities.

A. Appendix

A.1. Effect of static pressure on absolute paleointensity recording

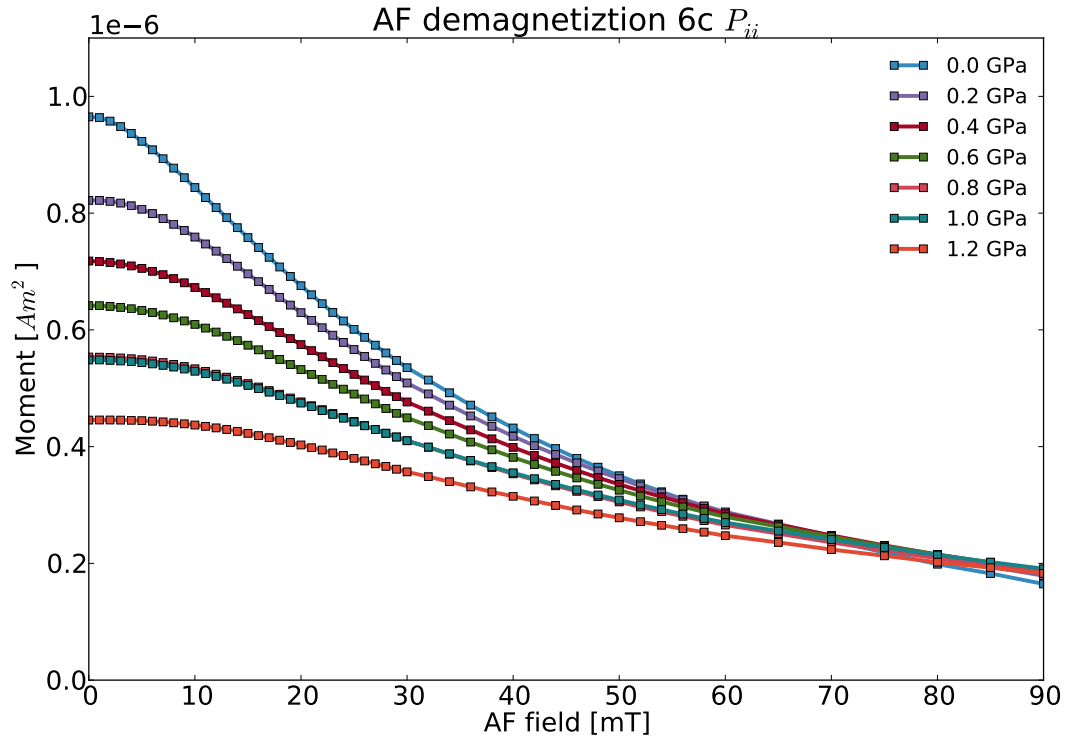


Figure A.1.: Alternating field (AF) demagnetization of a 1.2 T SIRM of an obsidian sample after cycling to successively higher pressure. The sample was given a new SIRM moment after each AF-demagnetization.

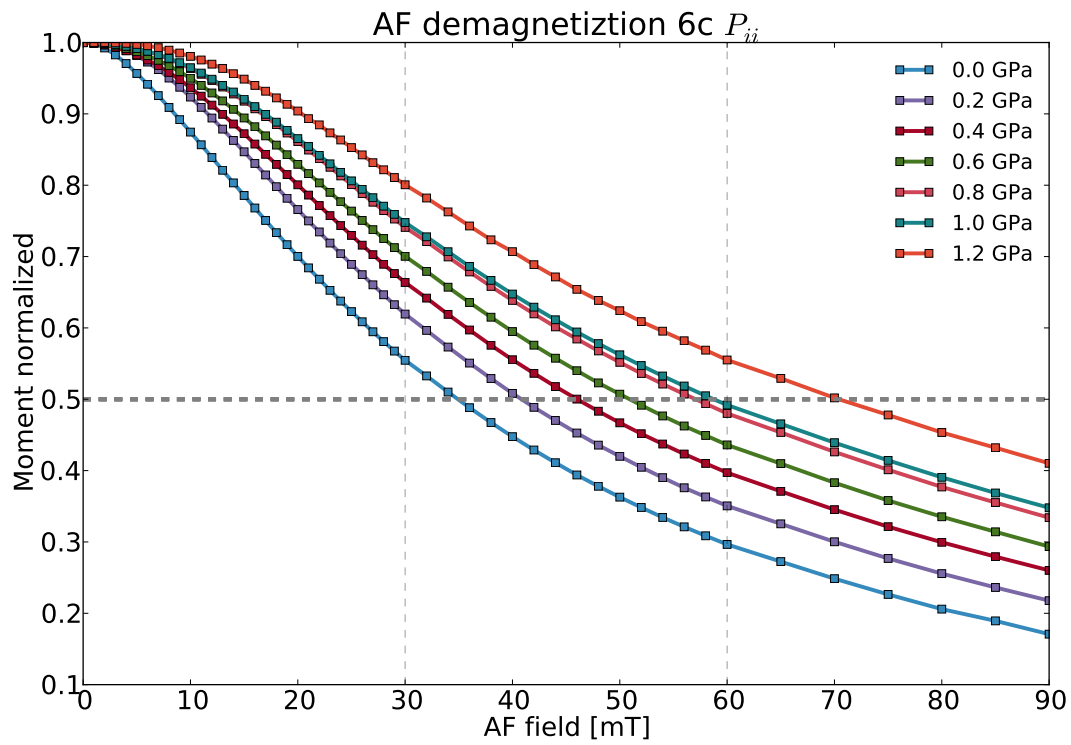


Figure A.2.: Data from fig. A.1 normalized. Crossing point with dashed line shows field at which 50% of the moment is demagnetized known as the median destructive field (MDF). The data shows that pressure demagnetization affects the low coercivity components, thereby increasing its apparent MDF.

A.2. Low temperature magnetic properties of monoclinic pyrrhotite

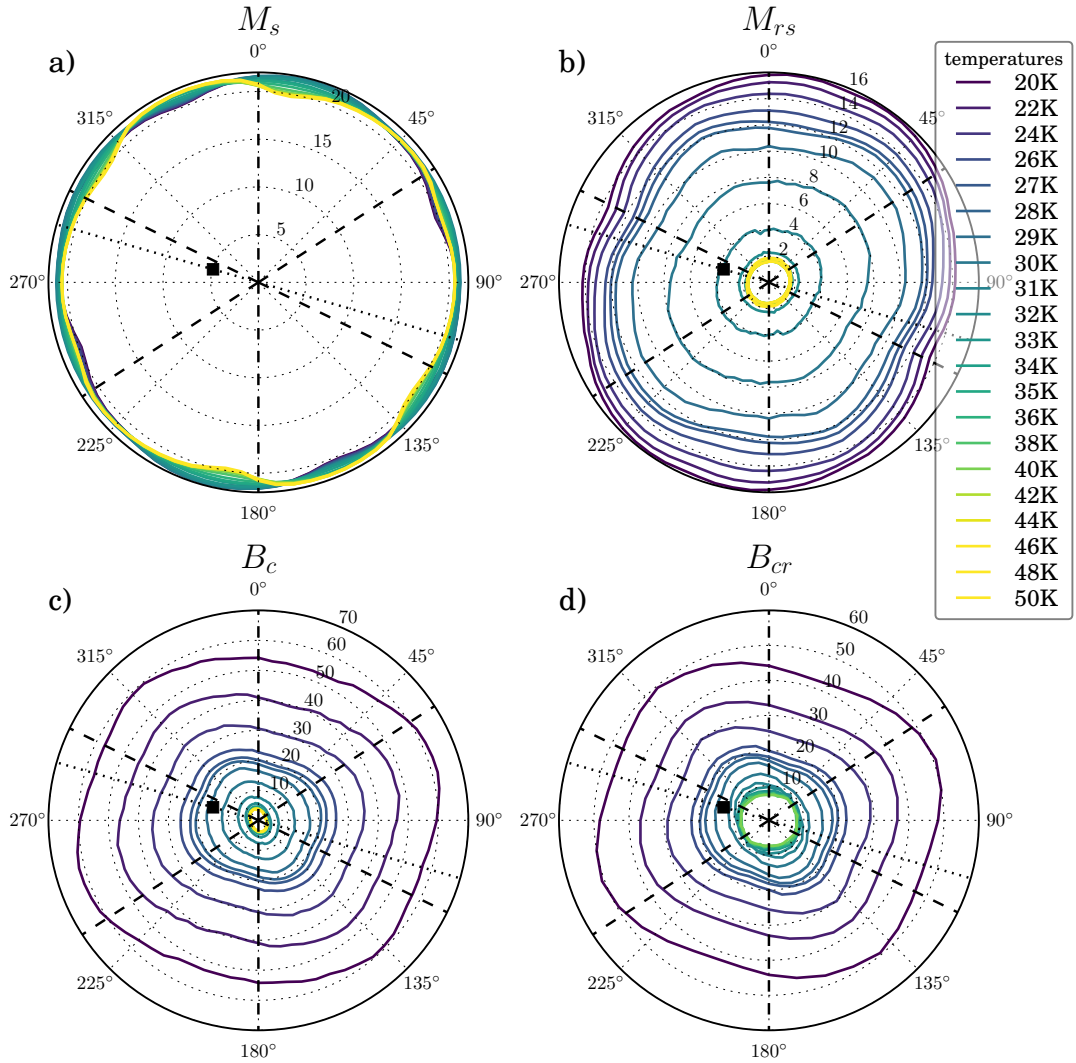


Figure A.3.: Polar representation of non normalized rock magnetic results of pyrrhotite single crystal. Data shown for all temperatures with respect to the a_1 axis at 0°. **a)** shows pseudo M_s^* , radial distance in Am^2/kg , **b)** shows remanent saturation magnetization M_{rs} , radial distance in Am^2/kg , **c)** shows coercivity B_c and **d)** shows remanence coercivity B_{cr} . **b, c)** radial distance in mT.

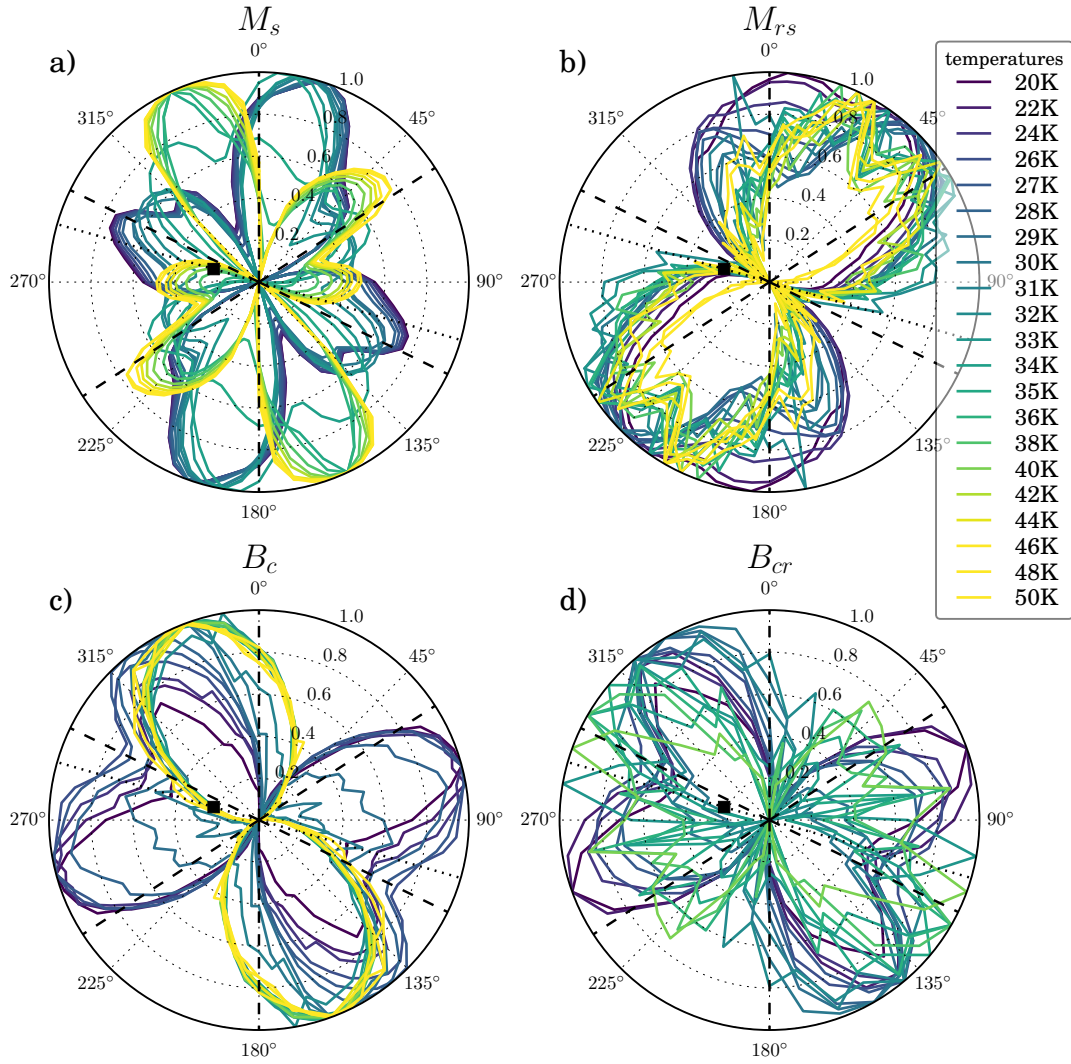


Figure A.4.: Polar representation of normalized rock magnetic results for all temperatures with respect to the a_1 axis at 0° . Data from fig. A.3 normalized to the minimum and maximum value of that temperature. 0 = min(T), 1 = max(T).

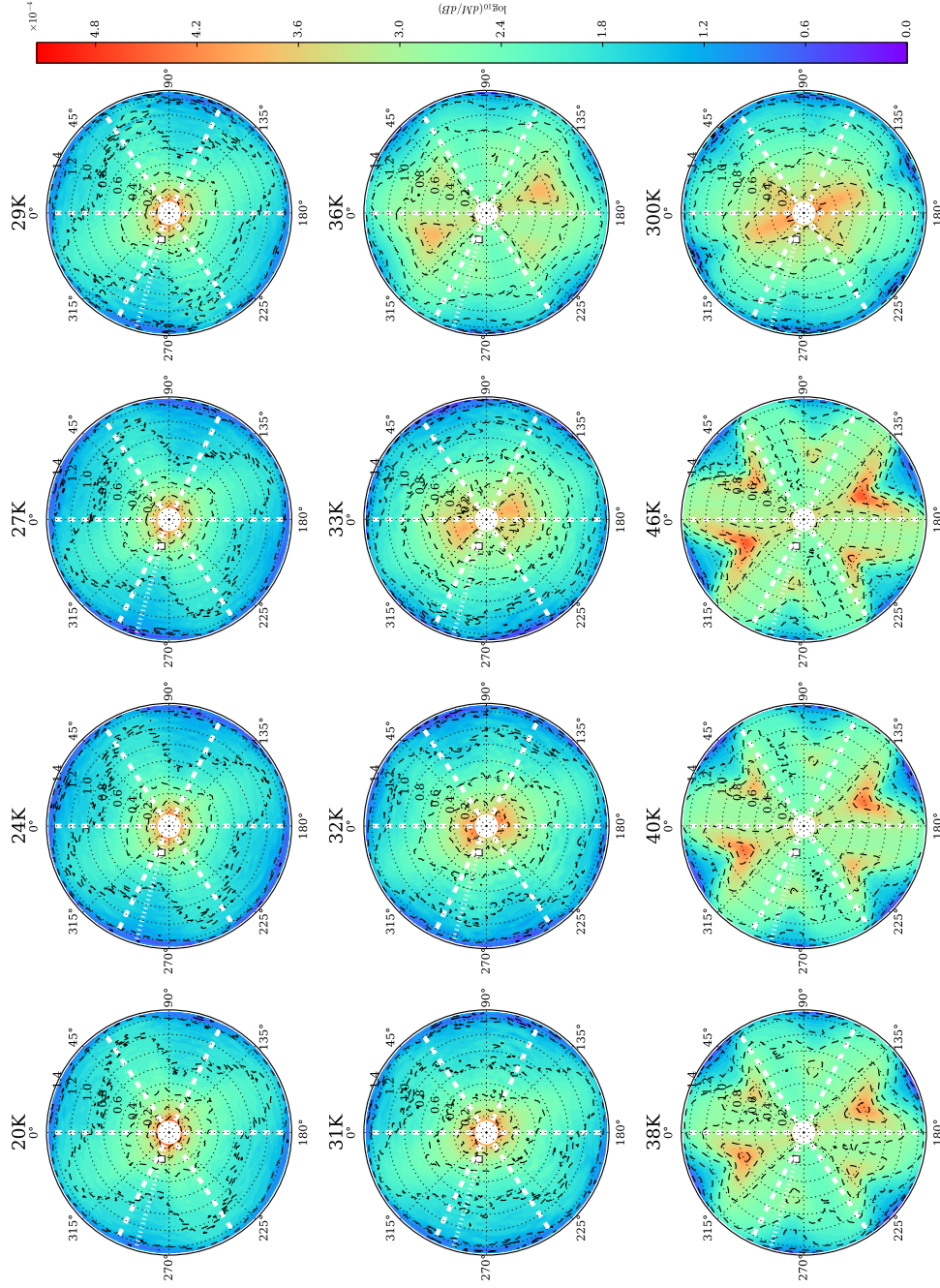


Figure A.5.: Angular dependence of the ascending branches of the hysteresis loops. Radial distance corresponds to the field value in T. The central area ($B < 40$ mT) was omitted for clarity. White dashed lines indicate the crystallographic a-axes. Pointed line and square represent the c-axis and its projection on the basal plane. A hexagonal pattern is apparent in the data between 50 and 34 K with the second inflections aligned between a-axes.

Bibliography

- Acton, G., Yin, Q. Z., Verosub, K. L., Jovane, L., Roth, A., Jacobsen, B., & Ebel, D. S. (2007). Micromagnetic coercivity distributions and interactions in chondrules with implications for paleointensities of the early solar system. *J. Geophys. Res. Solid Earth*, 112(B3), B03S90.
- Akdogan, N. G., Hadjipanayis, G. C., & Sellmyer, D. J. (2009). Anisotropic Sm-(Co,Fe) nanoparticles by surfactant-assisted ball milling. *Journal of Applied Physics*, 105(7), 07A710.
- Albertsen, J. F., NIELSEN, H. P., & Buchwald, V. F. (1983). On the Fine-Structure of Meteoritical Taenite-Tetrataenite and Its Interpretation. *Physica Scripta*, 27(4), 314–320.
- Anders, E. (1971). Meteorites and the Early Solar System. *Annual Review of Astronomy and Astrophysics*, 9(1), 1–34.
- ASC scientific (2016). ASC Model TD48 High-capacity dual-chamber thermal specimen demagnetizer for geologic samples. <http://www.ascscientific.com/td48.html>.
- Baldokhin, Y. V., Tcherdyntsev, V. V., Kaloshkin, S. D., Kochetov, G. A., & Pustov, Y. A. (1999). Transformations and fine magnetic structure of mechanically alloyed Fe–Ni alloys. *Journal of Magnetism and Magnetic Materials*, 203(1-3), 313–315.
- Banerjee, S. K. & Hargraves, R. B. (1972). Natural remanent magnetizations of carbonaceous chondrites and the magnetic field in the early solar system. *Earth and Planetary Science Letters*, 17(1), 110–119.
- Bastin, G. F. & Heijligers, H. J. M. (1991). Quantitative Electron Probe Microanalysis of Ultra-Light Elements (Boron-Oxygen). In *Electron Probe Quantitation* (pp. 145–161). Boston, MA: Springer US.
- Bertaut, E. F. (1953). Contribution à l'étude des structures lacunaires: la pyrrhotine. *Acta Crystallographica*, 6(6), 557–561.
- Besnus, M. J. & Meyer, A. J. (1964). *Nouvelles données expérimentales sur le magnétisme de la pyrrhotine naturelle*, volume 20. Proc. Int. Conf. Mag.
- Bezaeva, N. S., Gattacceca, J., Rochette, P., Sadykov, R. A., & Trukhin, V. I. (2010). Demagnetization of terrestrial and extraterrestrial rocks under hydrostatic pressure up to 1.2 GPa. *Physics of the Earth and Planetary Interiors*, 179(1–2), 7–20.
- Bezaeva, N. S., Rochette, P., Gattacceca, J., Sadykov, R. A., & Trukhin, V. I. (2007). Pressure demagnetization of the Martian crust: Ground truth from SNC meteorites. *Geophysical Research Letters*, 34(23).

- Biggin, A. J. & Perrin, M. (2007). The behaviour and detection of partial thermoremanent magnetisation (PTRM) tails in Thellier palaeointensity experiments. *Earth, Planets Sp.*, 59(7), 717–725.
- Biggin, A. J., Strik, G. H. M. A., & Langereis, C. G. (2009). The intensity of the geomagnetic field in the late-Archaeon: new measurements and an analysis of the updated IAGA palaeointensity database. *Earth, Planets and Space*, 61(1), 9–22.
- Biggin, A. J. & Thomas, D. (2003). The application of acceptance criteria to results of Thellier palaeointensity experiments performed on samples with pseudo-single-domain-like characteristics. *Physics of the Earth and Planetary Interiors*, 138(3-4), 279–287.
- Bin, M. & Pauthenet, R. (1963). Magnetic Anisotropy in Pyrrhotite. *Journal of Applied Physics*, 34(4), 1161.
- Bødker, F., Mørup, S., & Linderøth, S. (1994). Surface effects in metallic iron nanoparticles. *Physical Review Letters*, 72(2), 282–285.
- Bowles, J., Jackson, M. J., Chen, A., & Solheid, P. (2009). Interpretation of low-temperature data part 1: superparamagnetism and paramagnetism. *The IRM Quarterly*, 19(3).
- Brecher, A., Stein, J., & Fuhrman, M. (1977). The magnetic effects of brecciation and shock in meteorites: I. The Ll-chondrites. *Moon*, 17(3), 205–216.
- Butler, R. F. (1972). Natural remanent magnetization and thermomagnetic properties of the Allende meteorite. *Earth and Planetary Science Letters*, 17(1), 120–128.
- Butler, R. F. & Banerjee, S. K. (1975). Single-Domain Grain-Size Limits for Metallic Iron. *Journal of Geophysical Research: Solid Earth*, 80(2), 252–259.
- Carporzen, L., Weiss, B. P., Elkins-Tanton, L. T., Shuster, D. L., Ebel, D. S., & Gattacceca, J. (2011). Magnetic evidence for a partially differentiated carbonaceous chondrite parent body. *Proc. Natl. Acad. Sci.*, 108(16), 6386–6389.
- Charilaou, M., Kind, J., Koulialias, D., Weidler, P. G., Mensing, C., Löffler, J. F., & Gehring, A. U. (2015). Magneto-electronic coupling in modulated defect-structures of natural Fe_{1-x}S. *Journal of Applied Physics*, 118(8), 083903–6.
- Chauvin, A., Roperch, P., & Levi, S. (2005). Reliability of geomagnetic paleointensity data: the effects of the NRM fraction and concave-up behavior on paleointensity determinations by the Thellier method. *Physics of the Earth and Planetary Interiors*, 150(4), 265–286.
- Cisowski, S. M. (1981). Interacting vs. non-interacting single domain behavior in natural and synthetic samples. *Physics of the Earth and Planetary Interiors*, 26(1-2), 56–62.
- Cisowski, S. M. & Fuller, M. D. (1978). The effect of shock on the magnetism of terrestrial rocks. *J. Geophys. Res.*, 83(B7), 3441.

- Cisowski, S. M., Fuller, M. D., & Wu, Y. M. (1975). Magnetic effects of shock and their implications for magnetism of lunar samples. *Lunar and Planetary Science Conference Proceedings*, 5, 3123–3141.
- Clement, B. M., Haggerty, S., & Harris, J. (2008). Magnetic inclusions in diamonds. *Earth and Planetary Science Letters*, 267(1-2), 333–340.
- Coe, R. S. (1967). The Determination of Paleo-Intensities of the Earth's Magnetic Field with Emphasis on Mechanisms which Could Cause Non-ideal Behavior in Thellier's Method. *Journal of geomagnetism and geoelectricity*, 19(3), 157–179.
- Coe, R. S., Grommé, S., & Mankinen, E. A. (1978). Geomagnetic paleointensities from radiocarbon-dated lava flows on Hawaii and the question of the Pacific nondipole low. *J. Geophys. Res.*, 83(B4), 1740.
- Collinson, D. (1982). *Methods in Rock Magnetism and Palaeomagnetism*. Techniques and instrumentation. Chapman and Hall.
- Cournede, C., Gattacceca, J., Gounelle, M., Rochette, P., Weiss, B. P., & Zanda, B. (2015). An early solar system magnetic field recorded in CM chondrites. *Earth and Planetary Science Letters*, 410, 62–74.
- Crangle, J. & Goodman, G. M. (1971). The Magnetization of Pure Iron and Nickel. *Proceedings of the Royal Society A: Mathematical, Physical and Engineering Sciences*, 321(1547), 477–491.
- Crangle, J. & Hallam, G. C. (1963). The Magnetization of Face-Centred Cubic and Body-Centred Cubic Iron + Nickel Alloys. *Proceedings of the Royal Society of London A: Mathematical, Physical and Engineering Sciences*, 272(1348), 119–132.
- Day, R., Fuller, M. D., & Schmidt, V. a. (1977). Hysteresis properties of titanomagnetites: Grain-size and compositional dependence. *Physics of the Earth and Planetary Interiors*, 13(4), 260–267.
- Dekkers, M. J. (1988). Magnetic properties of natural pyrrhotite Part I: Behaviour of initial susceptibility and saturation-magnetization-related rock-magnetic parameters in a grain-size dependent framework. *Physics of the Earth and Planetary Interiors*, 52(3-4), 376–393.
- Dekkers, M. J. (1989). Magnetic properties of natural pyrrhotite. II. High- and low-temperature behaviour of Jrs and TRM as function of grain size. *Physics of the Earth and Planetary Interiors*, 57(3-4), 266–283.
- Dekkers, M. J. & Böhnell, H. N. (2006). Reliable absolute palaeointensities independent of magnetic domain state. *Earth and Planetary Science Letters*, 248(1-2), 508–517.
- Dekkers, M. J., Mattéi, J.-L., Fillion, G., & Rochette, P. (1989). Grain-size dependence of the magnetic behavior of pyrrhotite during its low-temperature transition at 34 K. *Geophysical Research Letters*, 16(8), 855–858.
- Djekoun, A., Bouzabata, B., Otmani, A., & Greneche, J. M. (2004). X-ray diffraction and Mössbauer studies of nanocrystalline Fe–Ni alloys prepared by mechanical alloying. *Catalysis Today*, 89(3), 319–323.

- Dunlop, D. J. (1981). The rock magnetism of fine particles. *Physics of the Earth and Planetary Interiors*, 26(1-2), 1–26.
- Dunlop, D. J. (2002a). Theory and application of the Day plot (Mrs/Ms versus Hcr/Hc) 1. Theoretical curves and tests using titanomagnetite data. *Journal of Geophysical Research: Solid Earth*, 107(B3), 2056.
- Dunlop, D. J. (2002b). Theory and application of the Day plot (Mrs/Ms versus Hcr/Hc) 2. Application to data for rocks, sediments, and soils. *Journal of Geophysical Research: Solid Earth*, 107(B3), 2057.
- Dunlop, D. J. (2003). Stepwise and continuous low-temperature demagnetization. *Geophysical Research Letters*, 30(11), 1–4.
- Dunlop, D. J. (2005). Linear and nonlinear Thellier paleointensity behavior of natural minerals. *J. Geophys. Res.*, 110(B1), 1–15.
- Dunlop, D. J. & Argyle, K. S. (1997). Thermoremanence, anhysteretic remanence and susceptibility of submicron magnetites: Nonlinear field dependence and variation with grain size. *J. Geophys. Res.*, 102(B9), 20199.
- Dunlop, D. J. & Özdemir, Ö. (1997). *Rock magnetism: fundamentals and frontiers*, volume 3. Cambridge university press.
- Dunlop, D. J., Ozima, M., & Kinoshita, H. (1969). Piezomagnetization of Single-Domain Grains: A Graphical Approach. *Journal of geomagnetism and geoelectricity*, 21(2), 513–518.
- Egli, R. (2013). VARIFORC: An optimized protocol for calculating non-regular first-order reversal curve (FORC) diagrams. *Global and Planetary Change*, 110, 302–320.
- Emmerton, S., Muxworthy, A. R., Hezel, D. C., & Bland, P. a. (2011). Magnetic characteristics of CV chondrules with paleointensity implications. *J. Geophys. Res.*, 116(E12), E12007.
- Eppelbaum, L., Kutasov, I., & Pilchin, A. (2014). Thermal Properties of Rocks and Density of Fluids. In *Applied Geothermics* (pp. 99–149). Berlin, Heidelberg: Springer Berlin Heidelberg.
- Fabian, K. (2001). A theoretical treatment of paleointensity determination experiments on rocks containing pseudo-single or multi domain magnetic particles. *Earth and Planetary Science Letters*, 188(1–2), 45–58.
- Fabian, K. (2003). Statistical theory of weak field thermoremanent magnetization in multidomain particle ensembles. *Geophysical Journal International*, 155(2), 479–488.
- Fabian, K. & Leonhardt, R. (2010). Multiple-specimen absolute paleointensity determination: An optimal protocol including pTRM normalization, domain-state correction, and alteration test. *Earth and Planetary Science Letters*, 297(1–2), 84–94.
- Fillion, G. & Rochette, P. (1988). The Low Temperature Transition In Monoclinic Pyrrhotite. *Le Journal de Physique Colloques*, 49(C8), C8–907–C8–908.

- Fu, R. R., Weiss, B. P., Lima, E. A., Harrison, R. J., Bai, X.-N., Desch, S. J., Ebel, D. S., Suavet, C., Wang, H., Glenn, D., Le Sage, D., Kasama, T., Walsworth, R. L., & Kuan, A. T. (2014). Solar nebula magnetic fields recorded in the Semarkona meteorite. *Science*, 346(6213), 1089–1092.
- Fuller, M., Cisowski, S., Hart, M., Haston, R., Schmidtke, E., & Jarrard, R. (1988). NRM: IRM(S) demagnetization plots; an aid to the interpretation of natural remanent magnetization. *Geophysical Research Letters*, 15(5), 518–521.
- Fuller, M. D. & Cisowski, S. M. (1987). Lunar paleomagnetism. *Geomagnetism*, Vol. 2, p. 307 - 455, 2, 307–455.
- Funaki, M. & Syono, Y. (2008). Acquisition of shock remanent magnetization for demagnetized samples in a weak magnetic field (7 μ T) by shock pressures 5-20 GPa without plasma-induced magnetization. *Meteorit. Planet. Sci.*, 43(3), 529–540.
- Gaffet, E., Hamzaoui, R., & Elkedim, O. (2004). Milling conditions effect on structure and magnetic properties of mechanically alloyed Fe–10% Ni and Fe–20% Ni alloys. *Materials Science and Engineering: A*, 381(1-2), 363–371.
- Gao, R., Chen, W., Zhang, J., Fong, W., Li, W., & Li, X. (2001). Intergrain interaction, coercivity and Henkel plot for NdFeB magnets. *Journal of Materials Science & Technology*.
- Garrick-Bethell, I. & Weiss, B. P. (2010). Kamacite blocking temperatures and applications to lunar magnetism. *Earth and Planetary Science Letters*, 294(1-2), 1–7.
- Gattacceca, J., Berthe, L., Boustie, M., Vadeboin, F., Rochette, P., & De Resseguier, T. (2008). On the efficiency of shock magnetization processes. *Physics of the Earth and Planetary Interiors*, 166(1-2), 1–10.
- Gattacceca, J., Boustie, M., Weiss, B. P., Rochette, P., Lima, E. a., Fong, L. E., & Baudenbacher, F. J. (2006). Investigating impact demagnetization through laser impacts and SQUID microscopy. *Geology*, 34(5), 333–336.
- Gattacceca, J., Lamali, A., Rochette, P., Boustie, M., & Berthe, L. (2007). The effects of explosive-driven shocks on the natural remanent magnetization and the magnetic properties of rocks. *Physics of the Earth and Planetary Interiors*, 162(1), 85–98.
- Gattacceca, J. & Rochette, P. (2004). Toward a robust normalized magnetic paleointensity method applied to meteorites. *Earth and Planetary Science Letters*, 227(3-4), 377–393.
- Gattacceca, J., Suavet, C., Rochette, P., Weiss, B. P., Winklhofer, M., Uehara, M., & Friedrich, J. M. (2014). Metal phases in ordinary chondrites: Magnetic hysteresis properties and implications for thermal history. *Meteoritics & Planetary Science*, 49(4), 652–676.
- Gilder, S. A., Egli, R., Hochleitner, R., Roud, S. C., Volk, M. W. R., Le Goff, M., & de Wit, M. (2011). Anatomy of a pressure-induced, ferromagnetic-to-paramagnetic transition in pyrrhotite: Implications for the formation pressure of diamonds. *Journal of Geophysical Research: Solid Earth*, 116(B10), B10101.

- Gilder, S. A. & Le Goff, M. (2008). Systematic pressure enhancement of titanomagnetite magnetization. *Geophysical Research Letters*, 35(10), L10302.
- Gilder, S. A., Le Goff, M., & Chervin, J.-C. (2006). Static stress demagnetization of single and multidomain magnetite with implications for meteorite impacts. *High Pressure Research*, 26(4), 539–547.
- Gilder, S. A., LeGoff, M., Chervin, J.-C., & Peyronneau, J. (2004). Magnetic properties of single and multi-domain magnetite under pressures from 0 to 6 GPa. *Geophysical Research Letters*, 31(10).
- Glaubitx, B., Buschhorn, S., Brüßing, F., Abrudan, R., & Zabel, H. (2011). Development of magnetic moments in $\text{Fe}_{1-x}\text{Ni}_x$ - alloys. *Journal of Physics: Condensed Matter*, 23(25), 254210.
- Halgedahl, S. L. (1998). Revisiting the Lowrie–Fuller test: alternating field demagnetization characteristics of single-domain through multidomain glass–ceramic magnetite. *Earth and Planetary Science Letters*, 160(3-4), 257–271.
- Halgedahl, S. L. & Fuller, M. D. (1981). The dependence of magnetic domain structure upon magnetization state in polycrystalline pyrrhotite. *Physics of the Earth and Planetary Interiors*, 26(1-2), 93–97.
- Hamzaoui, R., Elkedim, O., Fenineche, N., Gaffet, E., & Craven, J. (2003). Structure and magnetic properties of nanocrystalline mechanically alloyed Fe-10% Ni and Fe-20% Ni. *Materials Science and Engineering: A*, 360(1-2), 299–305.
- Henkel, O. (1964). Remanenzverhalten und Wechselwirkungen in hartmagnetischen Teilchenkollektiven. *physica status solidi (b)*, 7(3), 919–929.
- Hood, L. L. & Cisowski, S. M. (1983). Paleomagnetism of the moon and meteorites. *Rev. Geophys.*, 21(3), 676.
- Jackson, M. (2007). *Encyclopedia Of Geomagnetism And Paleomagnetism*. Dordrecht: Springer Netherlands.
- Jackson, M. J. & Solheid, P. A. (2010). On the quantitative analysis and evaluation of magnetic hysteresis data. *Geochemistry, Geophysics, Geosystems*, 11(4).
- Kaloshkin, S. D., Tcherdyntsev, V. V., Tomilin, I. a., Baldokhin, Y. V., & Shelekhov, E. V. (2001). Phase transformations in Fe–Ni system at mechanical alloying and consequent annealing of elemental powder mixtures. *Physica B: Condensed Matter*, 299(3-4), 236–241.
- Kanthal (2002). *Kanthal Handbook*. Technical report.
- Kapicka, A. (1983). Irreversible changes of anisotropy of magnetic-susceptibility of rocks due to uniaxial pressure. *Journal Of Geophysics-Zeitschrift Fur Geophysik*, 53(3), 144–148.
- Kean, W. F., Day, R., Fuller, M. D., & Schmidt, V. a. (1976). The effect of uniaxial compression on the initial susceptibility of rocks as a function of grain size and composition of their constituent titanomagnetites. *Journal of Geophysical Research: Solid Earth*, 81(5), 861–872.

- Kind, J., Garcia-Rubio, I., Charilaou, M., Nowaczyk, N. R., Loffler, J. F., & Gehring, A. U. (2013). Domain-wall dynamics in 4C pyrrhotite at low temperature. *Geophysical Journal International*, 195(1), 192–199.
- Kirschvink, J. L., Kopp, R. E., Raub, T. D., Baumgartner, C. T., & Holt, J. W. (2008). Rapid, precise, and high-sensitivity acquisition of paleomagnetic and rock-magnetic data: Development of a low-noise automatic sample changing system for superconducting rock magnetometers. *Geochemistry, Geophysics, Geosystems*, 9(5).
- Kletetschka, G., Acuña, M. H., Kohout, T., Wasilewski, P. J., & Connerney, J. E. P. (2004a). An empirical scaling law for acquisition of thermoremanent magnetization. *Earth and Planetary Science Letters*, 226(3–4), 521–528.
- Kletetschka, G., Connerney, J. E. P., Ness, N. F., & Acuña, M. H. (2004b). Pressure effects on Martian crustal magnetization near large impact basins. *Meteorit. Planet. Sci.*, 39(11), 1839–1848.
- Koch, C. C. (1997). Synthesis of nanostructured materials by mechanical milling: problems and opportunities. *Nanostructured Materials*, 9(1–8), 13–22.
- Koulialias, D., Kind, J., Charilaou, M., Weidler, P. G., Loffler, J. F., & Gehring, A. U. (2015). Variable defect structures cause the magnetic low-temperature transition in natural monoclinic pyrrhotite. *Geophysical Journal International*, 204(2), 961–967.
- Krásá, D., Heunemann, C., Leonhardt, R., & Petersen, N. (2003). Experimental procedure to detect multidomain remanence during Thellier–Thellier experiments. *Phys. Chem. Earth, Parts A/B/C*, 28(16–19), 681–687.
- Krot, A. N., Keil, K., Scott, E. R. D., Goodrich, C. A., & Weisberg, M. K. (2007). Classification of Meteorites. In *Treatise on Geochemistry* (pp. 1–52). Elsevier.
- Kuhrt, C. & Schultz, L. (1993). Phase formation and martensitic transformation in mechanically alloyed nanocrystalline Fe–Ni. *Journal of Applied Physics*, 73(4), 1975.
- Lappe, S.-C. L. L., Church, N. S., Kasama, T., da Silva Fanta, A. B., Bromiley, G., Dunin-Borkowski, R. E., Feinberg, J. M., Russell, S., & Harrison, R. J. (2011). Mineral magnetism of dusty olivine: A credible recorder of pre-accretionary remanence. *Geochemistry, Geophysics, Geosystems*, 12(12).
- Lappe, S.-C. L. L., Feinberg, J. M., Muxworthy, A. R., & Harrison, R. J. (2013). Comparison and calibration of nonheating paleointensity methods: A case study using dusty olivine. *Geochemistry, Geophysics, Geosystems*, 14(7), 2143–2158.
- Leonhardt, R. (2006). Analyzing rock magnetic measurements: The RockMagAnalyzer 1.0 software. *Computers & Geosciences*, 32(9), 1420–1431.
- Leonhardt, R., Heunemann, C., & Krásá, D. (2004). Analyzing absolute paleointensity determinations: Acceptance criteria and the software ThellierTool4.0. *Geochemistry, Geophys. Geosystems*, 5(12).
- Leonhardt, R., Matzka, J., Nichols, A., & Dingwell, D. (2006). Cooling rate correction of paleointensity determination for volcanic glasses by relaxation geospeedometry. *Earth and Planetary Science Letters*, 243(1–2), 282–292.

- Levi, S. (1977). The effect of magnetite particle size on paleointensity determinations of the geomagnetic field. *Physics of the Earth and Planetary Interiors*, 13(4), 245–259.
- Li, X. G., Chiba, A., & Takahashi, S. (1997). Preparation and magnetic properties of ultrafine particles of Fe-Ni alloys. *Journal of Magnetism and Magnetic Materials*, 170(3), 339–345.
- Louzada, K. L., Stewart, S. T., & Weiss, B. P. (2007). Effect of shock on the magnetic properties of pyrrhotite, the Martian crust, and meteorites. *Geophysical Research Letters*, 34(5), L05204.
- Louzada, K. L., Stewart, S. T., Weiss, B. P., Gattacceca, J., & Bezaeva, N. S. (2010). Shock and static pressure demagnetization of pyrrhotite and implications for the Martian crust. *Earth and Planetary Science Letters*, 290(1-2), 90–101.
- Lowrie, W. (2012). Identification of ferromagnetic minerals in a rock by coercivity and unblocking temperature properties. *Geophysical Research Letters*, 17(2), 159–162.
- Lutterotti, L., Matthies, S., & Wenk, H. R. (1999). Lutterotti: MAUD: a friendly Java program for material analysis using diffraction. *IUCr: Newsletter of the CPD*, 21, 14–15.
- Magnetic-Measurements (2016). Thermal demagnetiser MMTD80A.
<http://www.magnetic-measurements.com/products/new-high-precision-thermal-demagnetizers-paleomagnetic-furnaces/>.
- Martin-Hernandez, F., Dekkers, M. J., Dekkers, M. J., Dekkers, M. J., Bominaar-Silkens, I. M. a., & Maan, J. C. (2008). Magnetic anisotropy behaviour of pyrrhotite as determined by low- and high-field experiments. *Geophysical Journal International*, 174(1), 42–54.
- Menyeh, A. & O'Reilly, W. (1997). Magnetic Hysteresis Properties of Fine Particles of Monoclinic Pyrrhotite Fe₇S₈. *Journal of geomagnetism and geoelectricity*, 49(7), 965–976.
- Mikami, I., Hirone, T., Watanabe, H., Maeda, S., Adachi, K., & Yamada, M. (1959). On the Magnetic Anisotropy of a Pyrrhotite Crystal. *Journal of the Physical Society of Japan*, 14(11), 1568–1572.
- Mittlefehldt, D. W., Killgore, M., & Lee, M. M. T. (2002). Petrology and geochemistry of D'Orbigny, geochemistry of Sahara 99555, and the origin of angrites. *Meteorit. Planet. Sci.*, 37(3), 345–369.
- Mittlefehldt, D. W., McCoy, T. J., Goodrich, C. A., & Kracher, A. (1998). Non-chondritic meteorites from asteroidal bodies. *Reviews in Mineralogy and Geochemistry*, 36(1), 4.1–4.195.
- Morden, S. J. (1992). A magnetic study of the Millbillillie (eucrite) achondrite: Evidence for a dynamo-type magnetising field. *Meteoritics*, 27(5), 560–567.
- Morimoto, N., Nakazawa, H., Nishigucmi, K., & Tokonami, M. (1970). Pyrrhotites: Stoichiometric Compounds with Composition Fe_{n-1}S_n (n≥8). *Science*, 168(3934), 964–966.

- Mørup, S., Hansen, M. F., & Frandsen, C. (2010). Magnetic interactions between nanoparticles. *Beilstein Journal of Nanotechnology*, 1, 182–190.
- Mørup, S., Hansen, M. F., & Frandsen, C. (2011). 1.14 Magnetic Nanoparticles. In *Comprehensive Nanoscience and Technology*. Elsevier.
- Moskowitz, B. M. (1991). Hitchhiker's guide to the to magnetism. In *Environmental Magnetism Workshop at the Institute for Rock Magnetism*: Institute for Rock Magnetism.
- Moys, M. H. (2015). Grinding to nano-sizes: Effect of media size and slurry viscosity. *Minerals Engineering*, 74(C), 64–67.
- Muxworthy, A. R., Dunlop, D. J., & Özdemir, Ö. (2003). Low-temperature cycling of isothermal and anhysteretic remanence: microcoercivity and magnetic memory. *Earth and Planetary Science Letters*, 205, 173–184.
- Muxworthy, A. R. & Williams, W. (2006). Understanding viscous magnetization of multidomain magnetite. *Journal of Geophysical Research: Solid Earth*, 111(B2), n/a–n/a.
- Muxworthy, A. R. & Williams, W. (2009). Critical superparamagnetic/single-domain grain sizes in interacting magnetite particles: implications for magnetosome crystals. *Journal of the ...*, 6(41), 1207–1212.
- Muxworthy, A. R. & Williams, W. (2015). Critical single-domain grain sizes in elongated iron particles: implications for meteoritic and lunar magnetism. *Geophysical Journal International*, 202(1), 578–583.
- Nagata, T. (1966). Main characteristics of piezo-magnetization and their qualitative interpretation. *J. Geomagn. Geoelectr.*, 18(1), 81–97.
- Nagata, T. (1979a). Magnetic properties and paleointensity of achondrites in comparison with those of Lunar surface rocks. In *Lunar Planet. Sci. Conf. Vol. 10*. (pp. 887–888).
- Nagata, T. (1979b). Meteorite magnetism and the early solar system magnetic field. *Physics of the Earth and Planetary Interiors*, 20(2-4), 324–341.
- Nagata, T., Arai, Y., & Momose, K. (1963). Secular variation of the geomagnetic total force during the last 5000 years. *J. Geophys. Res.*, 68(18), 5277.
- Néel, L. (1949). Preuves expérimentales du ferromagnétisme et de l'antiferromagnétisme. *Annales de l'institut Fourier*, 1, 163–183.
- Néel, M. L. (1952). Antiferromagnetism and ferrimagnetism. In *Proceedings of the Physical Society London Section A*.
- Néel, M. L. (1955). Some theoretical aspects of rock-magnetism. *Advances in Physics*, 4(14), 191–243.
- Newell, A. J. & Merrill, R. T. (1999). Single-domain critical sizes for coercivity and remanence. *Journal of Geophysical Research: Solid Earth*, 104(B1), 617–628.

- Nichols, C., Bryson, J., & Herrero-Albillos, J. (2016). Pallasite paleomagnetism: Quiescence of a core dynamo. *Earth and Planetary Science Letters*, 441, 103–112.
- Nishioka, I., Funaki, M., & Sekine, T. (2007). Shock-induced anisotropy of magnetic susceptibility: impact experiment on basaltic andesite. *Earth, Planets Sp.*, 59(11), e45–e48.
- O'Reilly, W. (1984). *Rock and Mineral Magnetism*. Blackie & Son Ltd.
- O'Reilly, W., Hoffmann, V., Chouker, A. C., Soffel, H. C., & Menyeh, A. (2000). Magnetic properties of synthetic analogues of pyrrhotite ore in the grain size range 1–24 μm . *Geophysical Journal International*, 142(3), 669–683.
- Otmani, A., Greneche, J. M., Djekoun, A., Boudinar, N., Chebli, A., Benabdeslem, M., & Bouzabata, B. (2009). Structure and magnetic properties of Fe-rich nanostructured $\text{Fe}_{100-X}\text{Ni}_X$ powders obtained by mechanical alloying. *Physics Procedia*, 2(3), 693–700.
- Paterson, G. A., Biggin, A. J., Hodgson, E., & Hill, M. J. (2015). Thellier-type paleointensity data from multidomain specimens. *Physics of the Earth and Planetary Interiors*, 245, 117–133.
- Paterson, G. A., Biggin, A. J., Yamamoto, Y., & Pan, Y. (2012). Towards the robust selection of Thellier-type paleointensity data: The influence of experimental noise. *Geochemistry, Geophysics, Geosystems*, 13, Q05Z43.
- Paterson, G. a., Heslop, D., & Muxworthy, A. R. (2010). Deriving confidence in paleointensity estimates. *Geochemistry, Geophysics, Geosystems*, 11(7), 1–15.
- Paterson, G. A., Tauxe, L., Biggin, A. J., Shaar, R., & Jonestrask, L. C. (2014). On improving the selection of Thellier-type paleointensity data. *Geochemistry, Geophysics, Geosystems*, 15(4), 1180–1192.
- Pearce, G. W. & Karson, J. A. (1981). On pressure demagnetization. *Geophysical Research Letters*, 8(7), 725–728.
- Perrin, M. (1998). Paleointensity determination, magnetic domain structure, and selection criteria. *J. Geophys. Res.*, 103, 30591.
- Peters, C. & Dekkers, M. J. (2003). Selected room temperature magnetic parameters as a function of mineralogy, concentration and grain size. *Physics and Chemistry of the Earth, Parts A/B/C*, 28(16–19), 659–667.
- Petrovský, E., Alcalá, M. D., Criado, J. M., Grygar, T., Kapička, A., & Šubrt, J. (2000). Magnetic properties of magnetite prepared by ball-milling of hematite with iron. *Journal of Magnetism and Magnetic Materials*, 210(1–3), 257–273.
- Pike, C. R., Roberts, A. P., & Verosub, K. L. (1999). Characterizing interactions in fine magnetic particle systems using first order reversal curves. *Journal of Applied Physics*, 85(9), 6660–6667.
- Pohl, J., Bleil, U., & Hornemann, U. (1975). Shock magnetization and demagnetization of basalt by transient stress up to 10 kbar. *J. Geophys.*, 41, 23–41.

- Pohl, J. & Eckstaller, A. (1981). The Effect of Shock on Remanence in Multi-Domain Iron Grains and Implications for Palaeointensity Measurements. *LUNAR Planet. Sci.*, 12, 851–853.
- Popa, N. C. & Lungu, G. A. (2013). Dependence of the strain diffraction line broadening on (hkl) and sample direction in textured polycrystals. *Journal of Applied Crystallography*, 46(2), 391–395.
- Pouchou, J. L. & Pichoir, F. (1984). New model for quantitative x-ray microanalysis. Part I: Application to the analysis of homogeneous samples. *Rech. Aerosp.*, (3), 13–38.
- Powell, A. V., Vaqueiro, P., Knight, K. S., Chapon, L. C., & Sánchez, R. D. (2004). Structure and magnetism in synthetic pyrrhotite Fe₇S₈: A powder neutron-diffraction study. *Phys. Rev. B*, 70(1), 014415.
- Pucher, R. & Fromm, K. (1985). Magnetkies – Ursache der magnetischen Anomalie Kirchzarten. In J. Homilius (Ed.), *Die Magnetische Anomalie Kirchzarten*, number E23 (pp. 263–277). Stuttgart, Germany: Schweizerbart Science Publishers.
- Pullaiah, G., Irving, E., Buchan, K. L., & Dunlop, D. J. (1975). Magnetization changes caused by burial and uplift. *Earth and Planetary Science Letters*, 28(2), 133–143.
- Rietveld, H. M. (1969). A profile refinement method for nuclear and magnetic structures. *Journal of Applied Crystallography*, 2(2), 65–71.
- Riisager, P. & Riisager, J. (2001). Detecting multidomain magnetic grains in Thellier palaeointensity experiments. *Physics of the Earth and Planetary Interiors*, 125(1-4), 111–117.
- Roberts, A. P., Heslop, D., Zhao, X., & Pike, C. R. (2014). Understanding fine magnetic particle systems through use of first-order reversal curve (FORC) diagrams. *Rev. Geophys.*
- Roberts, A. P., Pike, C. R., & Verosub, K. L. (2001). First-order reversal curve diagrams and thermal relaxation effects in magnetic particles. *Geophysical Journal International*, 145(3), 721–730.
- Rochette, P. (2003). Magnetic classification of stony meteorites: 1. Ordinary chondrites. *Meteorit. Planet. Sci.*, 38(2), 251–268.
- Rochette, P., Fillion, G., & Dekkers, M. J. (2011). Interpretation of low-temperature data part 4: the low-temperature magnetic transition of monoclinic pyrrhotite. *The IRM Quarterly*.
- Rochette, P., Fillion, G., Mattéi, J.-L., & Dekkers, M. J. (1990). Magnetic transition at 30–34 Kelvin in pyrrhotite: insight into a widespread occurrence of this mineral in rocks. *Earth and Planetary Science Letters*, 98(3-4), 319–328.
- Rochette, P., Gattacceca, J., Bonal, L., Bourot-Denise, M., Chevrier, V., Clerc, J.-P., Consolmagno, G., Folco, L., Gounelle, M., Kohout, T., Pesonen, L. J., Quirico, E., Sagnotti, L., & Skripnik, A. (2008). Magnetic classification of stony meteorites: 2. Non-ordinary chondrites. *Meteoritics & Planetary Science*, 43(5), 959–980.

- Rochette, P., Gattacceca, J., Bourot-Denise, M., Consolmagno, G., Folco, L., Kohout, T., Pesonen, L. J., & Sagnotti, L. (2009). Magnetic classification of stony meteorites: 3. Achondrites. *Meteoritics & Planetary Science*, 44(3), 405–427.
- Rochette, P., Lorand, J.-P., Fillion, G., & Sautter, V. (2001). Pyrrhotite and the remanent magnetization of SNC meteorites: a changing perspective on Martian magnetism. *Earth and Planetary Science Letters*, 190(1-2), 1–12.
- Sato, K., Yamada, M., & Hirone, T. (1964). Megnetocrystalline anisotropy of pyrrhotite. *Journal of the Physical Society of Japan*, 19(9), 1592–1595.
- Schwarz, E. J. & Vaughan, D. J. (1972). Magnetic Phase Relations of Pyrrhotite. *Journal of geomagnetism and geoelectricity*, 24(4), 441–458.
- Sekels GmbH (2016). Thermal treatment, <http://www.sekels.de/en/thermal-treatment/>.
- Sephton, M. A. (2002). Organic compounds in carbonaceous meteorites. *Natural product reports*, 19(3), 292–311.
- Sharp, T. G. & DeCarli, P. S. (2006). Shock effects in meteorites. *Meteorites and the early solar system II*.
- Shaw, J. (2010). Comment on “A new high-precision furnace for paleomagnetic and paleointensity studies: Minimizing magnetic noise generated by heater currents inside traditional thermal demagnetizers” by Zhong Zheng, Xixi Zhao, and Chong-Shern Horng. *Geochemistry, Geophysics, Geosystems*, 11(11).
- Shcherbakov, V. P. & Shcherbakova, V. V. (2001). On the suitability of the Thellier method of palaeointensity determinations on pseudo-single-domain and multidomain grains. *Geophysical Journal International*, 146(1), 20–30.
- Shcherbakova, V., Shcherbakov, V. P., & Heider, F. (2000). Properties of partial thermoremanent magnetization in pseudosingle domain and multidomain magnetite grains. *J. Geophys. Res.*, 105(B1), 767–781.
- Snock, E., Gatel, C., Lacroix, L. M., Blon, T., Lachaize, S., Carrey, J., Respaud, M., & Chaudret, B. (2008). Magnetic Configurations of 30 nm Iron Nanocubes Studied by Electron Holography. *Nano Letters*, 8(12), 4293–4298.
- Soffel, H. C. (1977). Pseudo-Single-Domain Effects and Single-Domain Multidomain Transition in Natural Pyrrhotite Deduced from Domain Structure Observations. *Journal of Geophysics*, (42), 351–359.
- Soffel, H. C. (1981). Domain structure of natural fine-grained pyrrhotite in a rock matrix (diabase). *Physics of the Earth and Planetary Interiors*, 26(1-2), 98–106.
- Special Metals Corporation (2008). *Inconel alloy 600*. Technical report.
- Stacey, F. D. (1976). *Paleomagnetism of Meteorites*, volume 4. Annual Reviews.
- Stacey, F. D. & Lovering, J. F. (1959). Natural Magnetic Moments of Two Chondritic Meteorites. *Nature*, 183(4660), 529–530.

- Stöffler, D., Keil, K., & Edward R.D, S. (1991). Shock metamorphism of ordinary chondrites. *Geochim. Cosmochim. Acta*, 55(12), 3845–3867.
- Sugiura, N. & Strangway, D. W. (1988). Magnetic studies of meteorites. *Meteorites and the Early Solar System*, (pp. 595–615).
- Suryanarayana, C. (2001). Mechanical alloying and milling. *Progress in Materials Science*, 46(1-2), 1–184.
- Swartzendruber, L. J., Itkin, V. P., & Alcock, C. B. (1991). The Fe-Ni (iron-nickel) system. *Journal of Phase Equilibria*, 12(3), 288–312.
- Tarduno, J. A., Cottrell, R. D., Nimmo, F., Hopkins, J., Voronov, J., Erickson, A., Blackman, E., Scott, E. R. D., & McKinley, R. (2012). Evidence for a dynamo in the main group pallasite parent body. *Science*, 338(6109), 939–942.
- Thellier, E. & Thellier, M. (1959). Sur l'intensité du champ magnétique terrestre dans le passé historique et géologique. *Ann. Géophysique*, 15(3), 285–376.
- Tikoo, S. M., Gattacceca, J., Swanson-Hysell, N. L., Weiss, B. P., Suavet, C., & Cournède, C. (2015). Preservation and detectability of shock-induced magnetization. *J. Geophys. Res. Planets*, 120(9), 1461–1475.
- Tokonami, M., Nishiguchi, K., & Morimoto, N. (1972). Crystal structure of a monoclinic pyrrhotite (Fe₇S₈). *American Mineralogist*, 57, 1066–1080.
- Uehara, M. & Nakamura, N. (2006). Experimental constraints on magnetic stability of chondrules and the paleomagnetic significance of dusty olivines. *Earth and Planetary Science Letters*, 250(1-2), 292–305.
- Van de Moortèle, B., Reynard, B., Rochette, P., Jackson, M. J., Beck, P., Gillet, P., McMillan, P. F., & McCammon, C. a. (2007). Shock-induced metallic iron nanoparticles in olivine-rich Martian meteorites. *Earth and Planetary Science Letters*, 262(1-2), 37–49.
- Volk, M. W. & Gilder, S. A. (2016). Effect of static pressure on absolute paleointensity recording with implications for meteorites. *Journal of Geophysical Research: Solid Earth*, in revision.
- Volk, M. W. R., Eitel, M., & Gilder, S. A. (2016a). Thermal fluctuation study and arm at elevated temperatures in natural titanomagnetites. *Studia Geophysica et Geodaetica*, in preparation.
- Volk, M. W. R. & Gilder, S. A. (2012). Grain size and field dependence of the morin transition and mössbauer spectroscopy of synthetic hematite. In *EGU General Assembly Conference, Vienna, Austria Abstracts*.
- Volk, M. W. R. & Gilder, S. A. (2014). Effect of pressure on absolute paleointensity recording. In *14th Castle Meeting, Evora, Portugal, Abstracts*.
- Volk, M. W. R. & Gilder, S. A. (2015). Effect of static pressure on absolute paleointensity determinations with implications for meteorites. In *American Geophysical Union meeting, San Francisco, USA, Abstracts 72203*.

- Volk, M. W. R., Gilder, S. A., & Feinberg, J. M. (2016b). Low temperature magnetic properties of monoclinic pyrrhotite with particular relevance to the Besnus transition transition. *Geophysical Journal International*, in preparation.
- Volk, M. W. R., Wack, M., & Gilder, S. A. (2016c). Grain size dependence on the magnetic properties of Fe-Ni alloys with relevance to magnetic field recording in meteorites. In *Planetary Magnetism meeting Dresden, Abstracts*.
- Volk, M. W. R., Wack, M. R., & Gilder, S. A. (2016d). Evolution of magnetic properties of Fe₈₀Ni₂₀ during low and high energy mechanical alloying. *Journal of Magnetism and Magnetic Materials*, in preparation.
- von Dobeneck, T. (1996). A systematic analysis of natural magnetic mineral assemblages based on modelling hysteresis loops with coercivity-related hyperbolic basis functions. *Geophysical Journal International*, 124(3), 675–694.
- Wack, M. (2010). A new software for the measurement of magnetic moments using SQUID and spinner magnetometers. *Comput. Geosci.*, 36(9), 1178–1184.
- Wack, M. R. (2016). Dokumentationen für die sektion geophysik: Paleomagnetism: Sushibar.
- Wack, M. R. & Gilder, S. A. (2012). The SushiBar: An automated system for paleomagnetic investigations. *Geochemistry, Geophysics, Geosystems*, 13(3).
- Wardle, M. (2007). Magnetic fields in protoplanetary disks. *Astrophys. Space Sci.*, 311(1-3), 35–45.
- Wasilewski, P. (1974a). Magnetic remanence mechanisms in iron and iron-nickel alloys, metallographic recognition criteria and implications for lunar sample research. *The Moon*, 9(3-4), 335–354.
- Wasilewski, P. (1974b). The role of nickel content and the magnetic remanence in iron-nickel alloys of lunar composition. *The Moon*, 11(3-4), 313–316.
- Wasilewski, P. (1981a). Magnetization of small iron-nickel spheres. *Physics of the Earth and Planetary Interiors*, 26(1-2), 149–161.
- Wasilewski, P., Acuña, M. H., & Kletetschka, G. (2002). 443 Eros: Problems with the meteorite magnetism record in attempting an asteroid match. *Meteorit. Planet. Sci.*, 37(7), 937–950.
- Wasilewski, P. J. (1981b). New magnetic results from Allende C3(V). *Physics of the Earth and Planetary Interiors*, 26(1-2), 134–148.
- Weisberg, M. K., McCoy, T. J., & Krot, A. N. (2006). Systematics and Evaluation of Meteorite Classification. In D. S. Lauretta & H. Y. McSween Jr. (Eds.), *Meteorites and the Early Solar System II* (pp. 19–52). University of Arizona Press.
- Weiss, B. P., Berdahl, J. S., Elkins-Tanton, L. T., Stanley, S., Lima, E. A., & Carporzen, L. (2008a). Magnetism on the angrite parent body and the early differentiation of planetesimals. *Science*, 322(5902), 713–716.

- Weiss, B. P., Carporzen, L., Elkins-Tanton, L. T., & Ebel, D. S. (2009). Evidence for Internally Generated Magnetic Fields on the CV Chondrite Parent Planetesimal. *Lunar and Planetary Science Conference*, 40.
- Weiss, B. P. & Elkins-Tanton, L. T. (2013). Differentiated planetesimals and the parent bodies of chondrites. *Annu. Rev. Earth Planet. Sci.*, 41(1), 529–560.
- Weiss, B. P., Fong, L. E., Vali, H., Lima, E. A., & Baudenbacher, F. J. (2008b). Paleointensity of the ancient Martian magnetic field. *Geophysical Research Letters*, 35(23), L23207.
- Weiss, B. P., Gattacceca, J., Stanley, S., Rochette, P., & Christensen, U. R. (2010). Paleomagnetic Records of Meteorites and Early Planetesimal Differentiation. *Space Science Reviews*, 152(1), 341–390.
- Weiss, B. P., Vali, H., Baudenbacher, F. J., Kirschvink, J. L., Stewart, S. T., & Shuster, D. L. (2002). Records of an ancient Martian magnetic field in ALH84001. *Earth and Planetary Science Letters*.
- Williams, W. & Muxworthy, A. R. (2006). Observations of viscous magnetization in multidomain magnetite. *Journal of Geophysical Research: Solid Earth*, 111(B1), B01103–13.
- Wilson, E. A. (1994). The $\gamma \rightarrow \alpha$ Transformation in Low Carbon Irons. *ISIJ International*, 34(8), 615–630.
- Wohlfarth, E. P. (1958). Relations between Different Modes of Acquisition of the Remanent Magnetization of Ferromagnetic Particles. *Journal of Applied Physics*, 29(3), 595–596.
- Wolfers, P., Fillion, G., Ouladdiaf, B., Ballou, R., & Rochette, P. (2011). The Pyrrhotite 32 K Magnetic Transition. *Solid State Phenomena*, 170, 174–179.
- Xu, M., Bahl, C. R. H., Frandsen, C., & Mørup, S. (2004). Interparticle interactions in agglomerates of α -Fe₂O₃ nanoparticles: influence of grinding. *Journal of Colloid and Interface Science*, 279(1), 132–136.
- Xu, S. & Dunlop, D. J. (2004). Thellier paleointensity theory and experiments for multidomain grains. *J. Geophys. Res.*, 109(B7), 148–227.
- Yin, H. & Chow, G.-M. (2009). Effects of oleic acid surface coating on the properties of nickel ferrite nanoparticles/PLA composites. *Journal of Biomedical Materials Research Part A*, 91A(2), 331–341.
- Yu, Y. (2006). How accurately can NRM/SIRM determine the ancient planetary magnetic field intensity? *Earth and Planetary Science Letters*, 250(1-2), 27–37.
- Yu, Y. (2010). Paleointensity determination using anhysteretic remanence and saturation isothermal remanence. *Geochemistry, Geophysics, Geosystems*, 11(2).
- Yu, Y., Tauxe, L., & Genevey, A. (2004). Toward an optimal geomagnetic field intensity determination technique. *Geochemistry, Geophysics, Geosystems*, 5(2).

- Zheng, Z., Zhao, X., & Horng, C.-S. (2010). Reply to comment by John Shaw on "A new high-precision furnace for paleomagnetic and paleointensity studies: Minimizing magnetic noise generated by heater currents inside traditional thermal demagnetizers". *Geochemistry, Geophysics, Geosystems*, 11(11).
- Zheng, Zhong, Zhao, Xixi, Horng, C S, & Horng, Chorng-Shern (2010). A new high-precision furnace for paleomagnetic and paleointensity studies: Minimizing magnetic noise generated by heater currents inside traditional thermal demagnetizers. *Geochemistry, Geophysics, Geosystems*, 11(4).
- Zhu, L.-H. & Huang, Q.-W. (2003). Study on martensitic transformation of mechanically alloyed nanocrystalline Fe–Ni. *Materials Letters*, 57(24-25), 4070–4073.

Curriculum Vitae

Michael Volk

Education

- 2001 Thomas Mann Gymnasium Munich
- 2002 Civil service at Stiftung St. Zeno, Kirchseeon
- 2004 **Diploma Audio Engineering**
SAE Institute, Munich
- 2005 **Bachelor of Arts - Recording Arts**
Middlesex University London, Byron Bay, Australia
Thesis: *"An ergonomic approach in designing digital mixing consoles"*
- 2009 **Bachelor Geosciences**
Technical University & Ludwig Maximilians University, Munich
Thesis: *"Mössbauer study of natural Pyrrhotite and Hematite Crystals"*
- 2011 **Master Geophysics**
Ludwig Maximilians University, Munich
Thesis: *"Grain Size and Field Dependence of the Morin Transition and Mössbauer Spectroscopy of Synthetic Hematite"*
- 2012-present **PhD candidate in Geophysics**
Ludwig Maximilians University, Munich

Work experience

- 2005 Studio manager, supervisor, audio consultant, technical planning
SAE Institute, Byron Bay, Australia

- 2006 Administration, IT, light consulting, light architecture
Hellhaus GmbH. Munich
- 2006 Junior studio planner, project management and technical consulting
SMM Gesellschaft für Medien Integration, Munich
- 2008 Scientific consultant
EVISCO AG - The Electronic Vision Company, Munich
- 2006-2009 Event planning and organization, system integration
FMM GmbH Licht-, Ton- und Event design, Munich
- 2007-present Research Assistant (DFG financed), magnetism group
Ludwig Maximilians University, Munich
- 2012-2015 Teaching Assistant – Applied Geophysics
Ludwig Maximilians University, Munich

Awards

- 2014 **Outstanding Student Presentation Award**
14th Castle Meeting New Trends in Paleo, Rock and Environmental Magnetism.
Evora, Portugal

Languages

German: Mother tongue

English: fluent

Publications

- Volk, M. W. R. & Gilder, S. A. (2012). Grain size and field dependence of the morin transition and mössbauer spectroscopy of synthetic hematite. In *EGU General Assembly Conference, Vienna, Austria Abstracts*
- Volk, M. W. R. & Gilder, S. A. (2014). Effect of pressure on absolute paleointensity recording. In *14th Castle Meeting, Evora, Portugal, Abstracts*
- Volk, M. W. R. & Gilder, S. A. (2015). Effect of static pressure on absolute paleointensity determinations with implications for meteorites. In *American Geo-*

physical Union meeting, San Francisco, USA, Abstracts 72203

Volk, M. W. R., Wack, M., & Gilder, S. A. (2016c). Grain size dependence on the magnetic properties of Fe-Ni alloys with relevance to magnetic field recording in meteorites. In *Planetary Magnetism meeting Dresden, Abstracts*

Volk, M. W. & Gilder, S. A. (2016). Effect of static pressure on absolute paleointensity recording with implications for meteorites. *Journal of Geophysical Research: Solid Earth*, in revision

Volk, M. W. R., Gilder, S. A., & Feinberg, J. M. (2016b). Low temperature magnetic properties of monoclinic pyrrhotite with particular relevance to the Besnus transition. *Geophysical Journal International*, in preparation

Volk, M. W. R., Wack, M. R., & Gilder, S. A. (2016d). Evolution of magnetic properties of Fe₈₀Ni₂₀ during low and high energy mechanical alloying. *Journal of Magnetism and Magnetic Materials*, in preparation

Volk, M. W. R., Eitel, M., & Gilder, S. A. (2016a). Thermal fluctuation study and arm at elevated temperatures in natural titanomagnetites. *Studia Geophysica et Geodaetica*, in preparation